united nations
educational, scientific
and cultural
organization

international atomic
energy agency

the
abdus salam
international centre for theoretical physics

H4.SMR/1241-4

"Workshop on Three-Dimensional Modelling
of Seismic Waves Generation and their Propagation"

25 September - 6 October 2000

SEISMIC WAVE PROPAGATION IN LATERALLY HETEROGENEOUS ANELASTIC MEDIA: THEORY AND APPLICATIONS TO SEISMIC ZONATION

G.F. Panza[1,2], *F. Romanelli*[1,3], *F. Vaccari*[1,3]

1) Dept. of Earth Sciences, Trieste
2) SAND Group, ICTP, Trieste
3)GNDT, Rome

SEISMIC WAVE PROPAGATION IN LATERALLY HETEROGENEOUS ANELASTIC MEDIA: THEORY AND APPLICATIONS TO SEISMIC ZONATION

Giuliano F. Panza[1,2], Fabio Romanelli[1,3], Franco Vaccari[1,3]

1) Department of Earth Sciences, Via Weiss 4, 34127, Trieste, Italy

1) SAND Group, The Abdus Salam International Centre for Theoretical Physics, Miramare, Trieste, Italy

1) GNDT, Via Nizza 128, 00198, Rome, Italy

Advances in Geophysics, Vol. 43, 2000

1. Introduction

The guidelines of the International Decade for Natural Disaster Reduction (IDNDR - sponsored by United Nations), for the drawing up of pre-catastrophe plans of action, have led to the consolidation of the idea that zoning can and must be used as a means of prevention in areas that have not yet been hit by a disaster but are potentially prone to it. The urgency for improving earthquake risk assessment and risk management is clearly pointed out in the monograph on seismic zonation edited by Hays et al. (1998). Optimization of the techniques aimed at the prevention will be one of the basic themes of the development of seismic zoning in the 21st century.

The first scientific and technical methods developed for zoning were deterministic and based on the observation that damage distribution is often correlated to the spatial distribution and the physical properties of the underlying terrain and rocks. The 1970s saw the beginning of the construction of probabilistic seismic zoning maps on a national, regional, and urban (microzoning) scale. In the 1990s these instruments for the mitigation of seismic hazard were coming to prevail over deterministic cartography.

The most controversial question regarding definition of standards to be used in the evaluation of seismic hazard may be formulated as follows: should probabilistic or deterministic criteria and methods be used? Because probabilistic and deterministic approaches play mutually supportive roles in earthquake risk mitigation, at the current level of development in the modelling of seismogenesis

and of seismic wave propagation the best policy for the future is to combine the advantages offered by both methods, using integrated approaches (e.g., Reiter, 1990). In this way, among others, we have the main advantage of making possible the extension of seismic zoning to long periods, a period band up to now almost totally ignored by all methods, but which is acquiring continuously increasing importance, due to the widespread existence in the built environment of special objects, with relatively long free periods.

Studies carried out following strong earthquakes (e.g., 1985 Michoacan; 1995 Kobe) proved to be important sources of basic knowledge and have acted as catalysts for the use of zoning in seismic risk management. The impetus for this has come essentially from politicians and administrators particularly interested in rapid reconstruction, according to criteria which reduce the probability of a repetition of disasters. These postearthquake studies have led to the conclusion that the destruction caused by an earthquake is the result of the interaction of three complex systems: 1) the solid Earth system, made up of a) seismic source, b) propagation of the seismic waves, and c) geometry and physical conditions of the local geology; 2) the anthropic system, whose most important feature in this context is the quality of constructions (buildings, bridges, dams, pipelines, etc.); and 3) the social, economic, and political system, which governs the use and development of a settlement before it is struck by an earthquake.

Results have shown that in an area of urban development it is now technically possible to identify zones in which the heaviest damage can be predicted. A first-order zoning can be carried out at regional scale, based on the knowledge of the average properties of seismic sources and structural models. Microzonations are

possible as well, provided that very detailed information about the source, path, and local site conditions are available.

Seismic zoning can use scientific data bases, integrated in an expert system, by means of which it is possible to identify the safest and most suitable areas for urban development, taking into account the complex interaction between the solid Earth system, the environmental system, and the social, economic, and political system.It is also possible to define the seismic input that is going to affect a given building. The construction of an integrated expert system will make it possible to tackle the problem at its widest level of generality and to maintain the dynamic updating of zoning models, dictated by the acquisition of new data and the development of new model-building methods.

With the acquired knowledge, a drastic change is required in the orientation of zoning that must no longer be considered a postdisaster activity. It is necessary to proceed to predisaster surveys that can be usefully employed to mitigate the effects of the next earthquake, using all available technologies. As clearly indicated by the 1994 Northridge, California, and 1995 Kobe, Japan, events, we cannot confine ourselves to using what has been learned from a catastrophe solely in the area in which it took place. We must be able to take preventive steps, extending results obtained in a scientifically acceptable way, to areas in which no direct experience has yet been gained. An opportunity is offered in this direction by the scientific community's ability to make realistic simulations of the behavior of the solid Earth system through the computation of increasingly realistic synthetic seismograms with a broad frequency content.

The contribution of seismology to knowledge of the Earth's interior dramatically improved starting in the 1960s, when good quality instrumental

data became available, and computers allowed for fast processing. From the analysis of good quality seismograms it became evident that large lateral heterogeneities are not confined to the transition areas between oceans and continents, or just to the surficial geology, but characterize the whole structure of the Earth with the possible exception of the outer core.

Seismic waves can be represented as elastic perturbations propagating within a medium, originated by a transient disequilibrium in the stress field. The properties of seismic waves are ruled by the physics of elastic bodies, and are studied using the formalisms of elastodynamic theory.

It is necessary therefore to incorporate the effects of lateral heterogeneities in the direct modelling of the wavefield in order to retrieve a correct image of the heterogeneity itself and consequently to understand the geodynamics of the studied portion of the Earth.

Macroseismic observations made corresponding to the destructive events of the past 100 years or so have clearly evidenced the strong influence of near-surface geological and topographical conditions on damage distribution. Because most anthropic areas (e.g., megacities) are settled in relation to sedimentary basins such as river valleys, a realistic definition of the seismic input that takes into account site response has become one of the most relevant tasks in seismic engineering analysis.

An additional reason to extend modelling techniques to laterally heterogeneous structures is connected with the seismic hazard assessment. Using the available geological and geotechnical information, a lowcost parametric analysis can be performed to estimate the groundshaking site response. The theoretical approach, based on computer codes and developed from a detailed

knowledge of the seismic source process and the propagation of seismic waves in heterogeneous media, can simulate the ground motion associated with a given earthquake scenario.

2. The seismic wavefield

Seismic waves can be represented as elastic perturbations propagating within a medium, originated by a transient disequilibrium in the stress field. In the study of elastic bodies, to take into account macroscopic phenomena, it is assumed that the medium is a *continuum*, i.e., that the matter is distributed continuously in space. Therefore it is possible to define the mathematical functions that describe the fields associated with displacement, stress and deformation. Furthermore, being interested in the motion of the considered elastic body, the Lagrangian description is used, where the motion of each particle is analyzed in space and time, and the vector field $\mathbf{u}(x,t)$, associated with the displacement, is defined at any point of the body.

2.1 Equations of motion and constitutive relations

Considering the balance of forces, including inertia, body forces and surface forces acting on a cubic element within the continuum, and applying Newton's law, we obtain the system of equations of motion

$$\begin{aligned}
\rho\frac{\partial^2 u_x}{\partial t^2} &= \rho X + \frac{\partial \sigma_{xx}}{\partial x} + \frac{\partial \sigma_{yx}}{\partial y} + \frac{\partial \sigma_{zx}}{\partial z} \\
\rho\frac{\partial^2 u_y}{\partial t^2} &= \rho Y + \frac{\partial \sigma_{xy}}{\partial x} + \frac{\partial \sigma_{yy}}{\partial y} + \frac{\partial \sigma_{zy}}{\partial z} \\
\rho\frac{\partial^2 u_z}{\partial t^2} &= \rho Z + \frac{\partial \sigma_{xz}}{\partial x} + \frac{\partial \sigma_{yz}}{\partial y} + \frac{\partial \sigma_{zz}}{\partial z}
\end{aligned} \qquad (1)$$

where a Cartesian coordinate system (x, y, z) is adopted. $\sigma_{ij}(\mathbf{x},t)$ (i=x, y, z; j=x, y, z) indicates the second-order stress tensor, ρ is the density of the material, and X, Y, Z are the components of body forces for a unit mass.

Deformations, indicated by the second order tensor $e_{kl}(x,t)$ (k=x, y, z; l=x, y, z), if assumed infinitesimal, can be written as a function of displacements

$$\begin{aligned}
e_{xx} + e_{yy} + e_{zz} &= \frac{\partial u_x}{\partial x} + \frac{\partial u_y}{\partial y} + \frac{\partial u_z}{\partial z} \\
e_{xy} = e_{yx} &= \frac{1}{2}\left(\frac{\partial u_x}{\partial y} + \frac{\partial u_y}{\partial x}\right) \qquad e_{yz} = e_{zy} = \frac{1}{2}\left(\frac{\partial u_z}{\partial y} + \frac{\partial u_y}{\partial z}\right) \\
e_{xz} = e_{zx} &= \frac{1}{2}\left(\frac{\partial u_z}{\partial x} + \frac{\partial u_x}{\partial z}\right)
\end{aligned} \qquad (2)$$

In general, the relation between stress and deformation can take a very complex form since it has to include the effects of parameters like pressure, temperature, and the amount and variability of stress. Nevertheless, considering small deformations and stresses of short duration (conditions mostly satisfied in ground motion estimation problems), we can assume that the solid behaves

linearly and the constitutive relation linking stresses and deformation becomes *Hooke's law*

$$\sigma_{ij} = C_{ijkl} e_{kl} \qquad (3)$$

where the convention of repeated indices is used; C_{ijkl} is a fourth order symmetric tensor, whose 81 elements are the elastic moduli. If the solid is isotropic (as mostly occurs for the Earth) the components of the tensor C_{ijkl} assume the same value for all the axes and (3), using the Kronecker delta δ_{ij}, becomes):

$$\sigma_{ij} = \lambda \delta_{ij} e_{kk} + \mu (e_{ij} + e_{ji}) + \nu(e_{ij} - e_{ji}) \qquad (3a)$$

where λ, μ and ν are scalar quantities (Jeffreys and Jeffreys, 1950). Because e_{ij} is a symmetric tensor, (3a) can be rewritten as:

$$\sigma_{ij} = \lambda e_{kk} \delta_{ij} + 2 \mu e_{ij} \qquad (4)$$

and the quantities λ and μ are called *Lamè parameters*.

Using relations (3) and (4), Eq. (1) becomes a linear system of three differential equations with three unknowns: the three components of the displacement vector, whose coefficients depend upon the elastic parameters of the material. It is not possible to find the analytic solution for this system of equations, therefore it is necessary to add further approximations, chosen according to the adopted

resolving method. Two ways can be followed. In the first one an exact definition of the medium is given, and a direct *numerical* integration technique is used to solve the set of differential equations. The second way implies that exact *analytical* techniques are applied to an approximated model of the medium that may have the elastic parameters varying along one or more directions of heterogeneity. In the following we introduce the analytical solution valid for a flat layered halfspace that constitutes the base of knowledge for the treatment we will develop for models with lateral discontinuities.

2.2 Equations of elastic motion for a halfspace with vertical heterogeneities

Let us consider a halfspace in a system of Cartesian coordinates with the vertical z axis positive downward and the free surface, where vertical stresses (σ_{xz}, σ_{yz}, σ_{zz}) are null, is defined by the plane z=0 (Fig. 1).

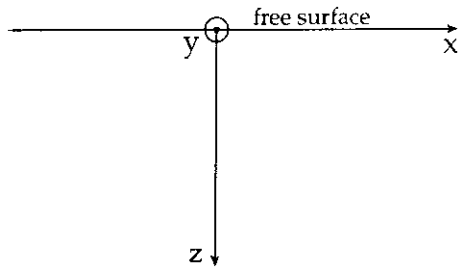

Fig. 1. Adopted reference system for a vertically heterogeneous halfspace.

Let us assume that λ, μ and ρ are piecewise continuous functions of z, and that body wave velocities, $\alpha = \sqrt{\frac{\lambda + 2\mu}{\rho}}$ and $\beta = \sqrt{\frac{\mu}{\rho}}$, assume their largest value, α_H and β_H, when $z > H$, remaining constant for greater depths.

If the elastic parameters depend only upon the vertical coordinate, using (2.1) the relations (2.3) and (2.4) become:

$$\rho \frac{\partial^2 u_x}{\partial t^2} = \rho X + (\lambda + 2\mu)\frac{\partial^2 u_x}{\partial x^2} + (\lambda + \mu)\frac{\partial^2 u_y}{\partial x \partial y} + (\lambda + \mu)\frac{\partial^2 u_z}{\partial x \partial z} + \\ + \mu \frac{\partial^2 u_x}{\partial y^2} + \mu \frac{\partial^2 u_x}{\partial z^2} + \frac{\partial \mu}{\partial z}\frac{\partial u_x}{\partial z} + \frac{\partial \mu}{\partial z}\frac{\partial u_z}{\partial x}$$

$$\rho \frac{\partial^2 u_y}{\partial t^2} = \rho Y + (\lambda + 2\mu)\frac{\partial^2 u_y}{\partial y^2} + (\lambda + \mu)\frac{\partial^2 u_x}{\partial x \partial y} + (\lambda + \mu)\frac{\partial^2 u_z}{\partial y \partial z} + \\ + \mu \frac{\partial^2 u_y}{\partial x^2} + \mu \frac{\partial^2 u_y}{\partial z^2} + \frac{\partial \mu}{\partial z}\frac{\partial u_y}{\partial z} + \frac{\partial \mu}{\partial z}\frac{\partial u_z}{\partial y} \qquad (5)$$

$$\rho \frac{\partial^2 u_z}{\partial t^2} = \rho Z + (\lambda + 2\mu)\frac{\partial^2 u_z}{\partial z^2} + (\lambda + \mu)\frac{\partial^2 u_x}{\partial x \partial z} + (\lambda + \mu)\frac{\partial^2 u_y}{\partial y \partial z} + \\ + \mu \frac{\partial^2 u_z}{\partial x^2} + \mu \frac{\partial^2 u_z}{\partial y^2} + \frac{\partial \lambda}{\partial z}\left(\frac{\partial u_x}{\partial x} + \frac{\partial u_y}{\partial y} + \frac{\partial u_z}{\partial z}\right) + 2\frac{\partial \mu}{\partial z}\frac{\partial u_z}{\partial z}$$

The boundary conditions that must be satisfied when solving (5) are the free surface condition at z=0

$$\sigma_{zz} = (\lambda + 2\mu)\frac{\partial u_z}{\partial z} + \lambda\left(\frac{\partial u_x}{\partial x} + \frac{\partial u_y}{\partial y}\right) = 0$$

$$\sigma_{zx} = \mu\left(\frac{\partial u_x}{\partial z} + \frac{\partial u_z}{\partial x}\right) = 0 \qquad (6)$$

$$\sigma_{zy} = \mu\left(\frac{\partial u_y}{\partial z} + \frac{\partial u_z}{\partial y}\right) = 0$$

and the continuity condition for the displacement and stress components $u_x, u_y, u_z, \sigma_{zx}, \sigma_{zy}, \sigma_{zz}$ all along the vertical axis, including the points where λ, μ and ρ are eventually discontinuous.

The complete solution of Eq. (5) can be represented in an integral form. At large distances from the source, compared with the wavelength, the main part of the solution is given by Rayleigh and Love modes (see e.g., Levshin (1973) and Aki and Richards (1980)).

Neglecting the body forces, we can consider solutions of (5) having the form of plane harmonic waves propagating along the positive x axis:

$$\mathbf{u}(x,t) = \mathbf{F}(z)e^{i(\omega t - kx)} \qquad (7)$$

where k is the wavenumber connected with the phase velocity c, i.e., $k=\omega/c$, and ω is the angular frequency.

Let us consider the case $c<\beta_H$. Using (7) Eq. (5) becomes:

$$\omega^2 \rho F_x - k^2(\lambda + 2\mu)F_x - ik(\lambda + \mu)\frac{\partial F_z}{\partial z} - ik\frac{\partial \mu}{\partial z}F_z + \frac{\partial}{\partial z}\left(\mu \frac{\partial F_z}{\partial z}\right) = 0$$

$$\omega^2 \rho F_y - k^2 \mu F_y + \frac{\partial}{\partial z}\left(\mu \frac{\partial F_y}{\partial z}\right) = 0 \qquad (8)$$

$$\omega^2 \rho F_z - k^2 \mu F_z - ik(\lambda + \mu)\frac{\partial F_x}{\partial z} - ik\frac{\partial \lambda}{\partial z}F_x + \frac{\partial}{\partial z}\left[(\lambda + 2\mu)\frac{\partial F_z}{\partial z}\right] = 0$$

We have to solve two independent eigenvalue problems for the three components of the vector $\mathbf{F}=(F_x,F_y,F_z)$. The first one describes the motion in the plane (x,z), i.e., P-SV waves. It has the form

$$\frac{\partial}{\partial z}\left[\mu\frac{\partial F_x}{\partial z} - i\,k\,\mu\,F_z\right] - ik\lambda\frac{\partial F_z}{\partial z} + F_x\left[\omega^2\rho - k^2(\lambda+2\mu)\right] = 0$$

$$\frac{\partial}{\partial z}\left[(\lambda+2\mu)\frac{\partial F_z}{\partial z} - i\,k\,\lambda\,F_x\right] - ik\,\mu\frac{\partial F_x}{\partial z} + F_z\left(\omega^2\rho - k^2\mu\right) = 0 \qquad (9)$$

and must be solved with the free surface boundary condition at $z = 0$

$$\sigma_{zz} = (\lambda+2\mu)\frac{\partial F_z}{\partial z} - i\,k\,\lambda\,F_x = 0$$

$$\sigma_{zx} = \mu\left(\frac{\partial F_x}{\partial z} - i\,k\,F_z\right) = 0 \qquad (10)$$

The second eigenvalue problem describes the case when the particle motion is limited to the y-axis and determines phase velocity and amplitude of SH waves. It has the form

$$\frac{\partial}{\partial z}\left(\mu\frac{\partial F_y}{\partial z}\right) + F_y(\omega^2\rho - k^2\mu) = 0 \qquad (11)$$

and must be solved with the boundary condition:

$$\sigma_{zy} = \mu\frac{\partial F_y}{\partial z} = 0 \qquad (12)$$

when $z = 0$.

2.3 *Multimodal method (SH and P-SV waves) in a layered halfspace*

Let us now assume that the vertical heterogeneity in the halfspace is modelled with a series of N-1 homogeneous flat layers, parallel to the free surface, overlying a homogeneous halfspace (see Fig. 2). Let ρ_m, α_m, β_m, and d_m, respectively be the density, P-wave and S-wave velocities, and the thickness of the m-th layer. Furthermore, let us define

$$r_{\alpha m} = \begin{cases} \sqrt{\left(\frac{c}{\alpha_m}\right)^2 - 1} & \text{if } c > \alpha_m \\ -i\sqrt{1 - \left(\frac{c}{\alpha_m}\right)^2} & \text{if } c < \alpha_m \end{cases} \qquad r_{\beta m} = \begin{cases} \sqrt{\left(\frac{c}{\beta_m}\right)^2 - 1} & \text{if } c > \beta_m \\ -i\sqrt{1 - \left(\frac{c}{\beta_m}\right)^2} & \text{if } c < \beta_m \end{cases} \qquad (13)$$

2.3.1 *Love modes*

For Love modes, the periodic solutions of the elastic equations of motion for the m-th layer are

$$u_x = u_z = 0$$

$$u_y = \left(v_m' e^{-ikr_{\beta m}z} + v_m'' e^{+ikr_{\beta m}z}\right)e^{i(\omega t - kx)} \qquad (14)$$

and the associated stress component is

$$\sigma_{zy} = \mu \frac{\partial u_y}{\partial z} = ik\mu r_{\beta m}\left(-v_m' e^{-ikr_{\beta m}z} + v_m'' e^{+ikr_{\beta m}z}\right) e^{i(\omega t - kx)} \qquad (15)$$

where v_m' and v_m'' are constants. Given the sign conventions adopted, the term in v' represents a plane wave whose direction of propagation makes an angle $\cot^{-1} r_{\beta m}$ with the +z direction when $r_{\beta m}$ is real, and a wave propagating in the +x direction with amplitude diminishing exponentially in the +z direction when $r_{\beta m}$ is imaginary. Similarly the term in v'' represents a plane wave making the same angle with the direction -z when $r_{\beta m}$ is real and a wave propagating in the +x direction with amplitude increasing in the +z direction when $r_{\beta m}$ is imaginary (Fig. 2).

For Love modes the boundary conditions that must be satisfied at any interface are the continuity of the transverse component of displacement, u_y, and the continuity of the tangential component of stress, σ_{zy}. Then we can use the Thomson-Haskell method and its modifications (e.g., Schwab and Knopoff, 1972; Florsch et al., 1991) to efficiently compute the multimodal dispersion of surface waves and therefore synthetic seismograms in anelastic media.

Let us consider the m-th layer and interface (m-1), where we set the origin of the coordinate system. It is convenient to use $\frac{\dot{u}_y}{c} = iku_y$ instead of displacement, u_y, so that we deal with nondimensional quantities.

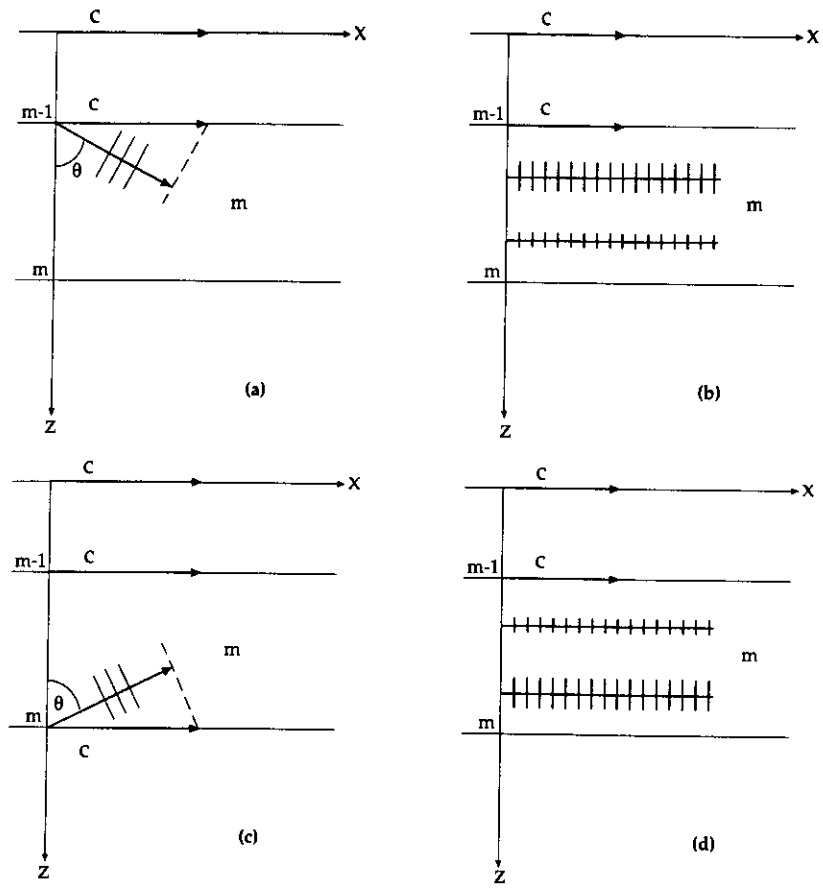

Fig. 2. For the adopted reference system the term in v' of equation (14) represents a plane wave whose direction of propagation makes an angle $\cot^{-1} r_{\beta m}$ with the +z direction when $r_{\beta m}$ is real (a), and a wave propagating in the +x direction with amplitude diminishing exponentially in the +z direction when $r_{\beta m}$ is imaginary (b). Similarly the term in v'' represents a plane wave making the same angle with the direction -z when $r_{\beta m}$ is real (c) and a wave propagating in the +x direction with amplitude increasing in the +z direction when $r_{\beta m}$ is imaginary (d).

At the interface (m-1) we have

$$\left(\frac{\dot{u}_y}{c}\right)_{m-1} = ik(v'_m + v''_m)$$

$$(\sigma_{zy})_{m-1} = ik\mu_m r_{\beta_m}(v''_m - v'_m) \qquad (16)$$

while at the m-th interface we have

$$\left(\frac{\dot{u}_y}{c}\right)_m = ik(v'_m + v''_m)\cos Q_m - k(v''_m - v'_m)\sin Q_m$$

$$(\sigma_{zy})_m = -k\mu_m r_{\beta_m}(v''_m + v'_m)\sin Q_m + ik\mu_m r_{\beta_m}(v''_m - v'_m)\cos Q_m \qquad (17)$$

where we define $Q_m = kr_{\beta_m}d_m$ and we drop the time-dependent term $e^{i\omega t}$.

Eliminating the quantities v_m' and v_m'' in Eqs. (16) and (17) we obtain

$$\left(\frac{\dot{u}_y}{c}\right)_m = \left(\frac{\dot{u}_y}{c}\right)_{m-1}\cos Q_m + i(\sigma_{zy})_{m-1}(\mu_m r_{\beta_m})^{-1}\sin Q_m$$

$$(\sigma_{zy})_m = \left(\frac{\dot{u}_y}{c}\right)_{m-1} i\mu_m r_{\beta_m}\sin Q_m + (\sigma_{zy})_{m-1}\cos Q_m \qquad (18)$$

Introducing the layer matrix

$$a_m = \begin{bmatrix} \cos Q_m & \frac{i\sin Q_m}{\mu_m r_{\beta_m}} \\ i\mu_m r_{\beta_m}\sin Q_m & \cos Q_m \end{bmatrix} \qquad (19)$$

Eq. (18) can be rewritten in the matrix form

$$\begin{bmatrix} \left(\frac{\dot{u}_y}{c}\right)_m \\ (\sigma_{zy})_m \end{bmatrix} = a_m \begin{bmatrix} \left(\frac{\dot{u}_y}{c}\right)_{m-1} \\ (\sigma_{zy})_{m-1} \end{bmatrix} \qquad (20)$$

Subsequently substituting m with values between (N-1) and 0 we have that

$$\begin{bmatrix} \left(\frac{\dot{u}_y}{c}\right)_{N-1} \\ (\sigma_{zy})_{N-1} \end{bmatrix} = A \begin{bmatrix} \left(\frac{\dot{u}_y}{c}\right)_0 \\ (\sigma_{zy})_0 \end{bmatrix} \qquad (21)$$

$$A = a_{N-1}a_{N-2}\ldots a_2 a_1$$

where A is a 2x2 matrix.

If we now use (16) with m=N, and remembering that the boundary conditions of surface waves and the free surface implies that $v_N'' = 0$ and $(\sigma_{zy})_0 = 0$, we have that

$$A_{21} + \mu_N r_{\beta_N} A_{11} = 0 \qquad (22)$$

The left-hand side of Eq. (22) is the *dispersion function* for Love modes (SH waves), where A_{21} and A_{11} are elements of the matrix A. The couples (ω,c) for which the dispersion function is equal to zero are its roots and represent the eigenvalues of the problem. Eigenvalues, according to the number of zeroes of the corresponding eigenfunctions, $u_y(z,\omega,c)$ and $\sigma_{zy}(z,\omega,c)$, can be subdivided in the dispersion curve of the fundamental mode (which has no nodal planes), of the first higher mode (having one nodal plane), of the second higher mode and so on. Once the phase velocity c is determined, we can compute analytically the group velocity using the implicit functions theory (Schwab and Knopoff, 1972), and the eigenfunctions (Florsch et al., 1991).

2.3.2 Rayleigh modes

For P-SV waves, periodic solutions of the elastic equation of motion for the m-th layer may be found by combining dilatational and rotational wave solutions

$$\Delta_m = \frac{\partial u_x}{\partial z} + \frac{\partial u_z}{\partial x} = \left(\Delta_m' e^{-ikr_{\alpha m} z} + \Delta_m'' e^{+ikr_{\alpha m} z}\right) e^{i(\omega t - kx)}$$

$$\delta_m = \frac{1}{2}\left[\frac{\partial u_x}{\partial z} - \frac{\partial u_z}{\partial x}\right] = \left(\delta_m' e^{-ikr_{\beta m} z} + \delta_m'' e^{+ikr_{\beta m} z}\right) e^{i(\omega t - kx)} \qquad (23)$$

where Δ_m', Δ_m'', δ_m' and δ_m'' are constants. Given the sign conventions adopted, the term in Δ_m' represents a plane wave whose direction of propagation makes an angle $\cot^{-1} r_{\alpha m}$ with the +z direction when $r_{\alpha m}$ is real, and a wave propagating in the +x direction with amplitude diminishing exponentially in the +z direction when $r_{\alpha m}$ is imaginary. Similarly the term in Δ_m'' represents a plane wave making

the same angle with the direction -z when $r_{\alpha m}$ is real and a wave propagating in the +x direction with amplitude increasing in the +z direction when $r_{\alpha m}$ is imaginary (e.g., see Fig. 2). The same considerations can be applied to the terms in δ_m' and δ_m'', substituting $r_{\alpha m}$ with $r_{\beta m}$. Dropping the term $\exp[i(\omega t - kx)]$ the displacements and the associated stress components corresponding to the dilatation and rotation, given by Eq. (23), can be written as

$$u_x = -\frac{\alpha_m^2}{\omega^2}\left(\frac{\partial \Delta_m}{\partial x}\right) - 2\frac{\beta_m^2}{\omega^2}\left(\frac{\partial \delta_m}{\partial z}\right) \qquad (24)$$

$$u_z = -\frac{\alpha_m^2}{\omega^2}\left(\frac{\partial \Delta_m}{\partial z}\right) + 2\frac{\beta_m^2}{\omega^2}\left(\frac{\partial \delta_m}{\partial x}\right) \qquad (25)$$

$$\sigma_{zz} = \rho_m\left\{\alpha_m^2 \Delta_m + 2\beta_m^2\left[\frac{\alpha_m^2}{\omega^2}\left(\frac{\partial^2 \Delta_m}{\partial x^2}\right) + 2\frac{\beta_m^2}{\omega^2}\left(\frac{\partial^2 \delta_m}{\partial z^2}\right)\right]\right\} \qquad (26)$$

$$\sigma_{zx} = 2\beta_m^2 \rho_m\left\{-\frac{\alpha_m^2}{\omega^2}\left(\frac{\partial^2 \Delta_m}{\partial x \partial z}\right) + \frac{\beta_m^2}{\omega^2}\left[\left(\frac{\partial^2 \delta_m}{\partial x^2}\right) - \left(\frac{\partial^2 \delta_m}{\partial z^2}\right)\right]\right\} \qquad (27)$$

For Rayleigh waves the boundary conditions that must be satisfied at any interface are the continuity of the displacement and stress components given in Eqs. (24-27).

As we did for Love modes, iterating over the interfaces we can build up the dispersion function, whose roots are the eigenvalues associated with the Rayleigh wave modes (P-SV waves). This is the procedure at the base of the modern and efficient methods for the computation of multimodal dispersion in anelastic media (e.g., Schwab and Knopoff, 1972; Schwab et al., 1984; Panza, 1985).

2.3.3 Modes radiated by point sources in anelastic media

The source is introduced in the medium representing the fault, which is supposed to be planar, as a discontinuity in the displacement and shear stresses fields, with respect to the fault plane. On the contrary, normal stresses are supposed to be continuous across the fault plane. Maruyama (1963) and Burridge and Knopoff (1964) demonstrated with the representation theorem the rigorous equivalence of the effects between a faulted medium with a discontinuity in the displacements and shear stress fields, and an unfaulted medium where proper body forces are applied.

Following the procedure proposed by Kausel and Schwab (1973), we assume that periods and wavelengths which we are interested in are large compared with the rise time and the dimensions of the source. Therefore the source function, describing the discontinuity of the displacement across the fault, can be approximated with a step function in time and a point source in space. Furthermore, if the normal stress is continuous across the fault, then for the representation theorem the equivalent body force in an unfaulted medium is a double-couple with null total moment. With this assumption, the eigenvalues and eigenfunctions of the problem having been determined, we can write the expression of the displacement with varying time, i.e., the synthetic seismogram, for the three components of motion. The asymptotic expression of the Fourier transform (hereafter called FT) of the displacement $\mathbf{U} = (U_x, U_y, U_z)$, at a distance r from the source, can be written as $\mathbf{U} = \sum_{m=1}^{\infty} {}^{m}\mathbf{U}$, where m is the mode index and:

$$
{}^{m}U_x(r,z,\omega) = \frac{e^{-i\frac{3}{4}\pi}}{\sqrt{2\pi}}\left[\chi_R(h_s,\varphi)S(\omega)\frac{\sqrt{k_R}e^{-ik_R r-\omega r C_{2R}}}{\sqrt{r}}\frac{\varepsilon_0 u_x(z,\omega)}{2c_R v_{gR} I_{1R}}\right]_m
$$

$$
{}^{m}U_y(r,z,\omega) = \frac{e^{-i\frac{3}{4}\pi}}{\sqrt{2\pi}}\left[\chi_L(h_s,\varphi)S(\omega)\frac{\sqrt{k_L}e^{-ik_L r-\omega r C_{2L}}}{\sqrt{r}}\frac{u_y(z,\omega)}{2c_L v_{gL} I_{1L}}\right]_m \qquad (28)
$$

$$
{}^{m}U_z(r,z,\omega) = {}^{m}U_x(r,z,\omega)e^{-i\frac{\pi}{2}}\varepsilon_0^{-1}
$$

The suffixes R and L refer to quantities associated with Rayleigh and Love modes, respectively.

In Eq. (28) $S(\omega) = |S(\omega)|\exp[i\arg(S(\omega))]$ is the FT of the source time function while $\chi(h_s,\varphi)$ represents the azimuthal dependence of the excitation factor (Ben-Menhaem and Harkrider, 1964)

$$
\begin{aligned}
\chi_R(h_s,\varphi) &= d_0 + i(d_{1R}\sin\varphi + d_{2R}\cos\varphi) + d_{3R}\sin 2\varphi + d_{4R}\cos 2\varphi \\
\chi_L(h_s,\varphi) &= i(d_{1L}\sin\varphi + d_{2L}\cos\varphi) + d_{3L}\sin 2\varphi + d_{4L}\cos 2\varphi
\end{aligned} \qquad (29)
$$

with

$$
\begin{aligned}
d_0 &= \frac{1}{2}B(h_s)\ \sin\lambda \sin 2\delta \\
d_{1R} &= -C(h_s)\ \sin\lambda \cos 2\delta \\
d_{2R} &= -C(h_s)\ \cos\lambda \cos\delta \\
d_{3R} &= A(h_s)\ \cos\lambda \sin\delta \\
d_{4R} &= -\frac{1}{2}A(h_s)\ \sin\lambda \sin 2\delta
\end{aligned}
\qquad (30)
$$

$$
\begin{aligned}
d_{1L} &= G(h_s)\ \cos\lambda \sin\delta \\
d_{2L} &= -G(h_s)\ \sin\lambda \cos 2\delta \\
d_{3L} &= \frac{1}{2}V(h_s)\ \sin\lambda \sin 2\delta \\
d_{4L} &= V(h_s)\ \cos\lambda \sin\delta
\end{aligned}
$$

where φ is the angle between the strike of the fault and the direction obtained connecting the epicenter with the station, measured anticlockwise; h_s is the focal depth; δ is the dip angle and λ is the rake angle (see Fig. 3). The functions of h_s that appear in (30) depend on the values assumed by the eigenfunctions at the hypocenter

$$
\begin{aligned}
A(h_s) &= -\frac{u_x^*(h_s)}{u_z(0)} \\
B(h_s) &= -\left(3 - 4\frac{\beta^2(h_s)}{\alpha^2(h_s)}\right)\frac{u_x^*(h_s)}{u_z(0)} - \frac{2}{\rho(h_s)\,\alpha^2(h_s)}\frac{\sigma_{zz}^*(h_s)}{\dot{u}_z(0)/c} \\
C(h_s) &= -\frac{1}{\mu(h_s)}\frac{\sigma_{zx}(h_s)}{\dot{u}_z(0)/c} \\
G(h_s) &= -\frac{1}{\mu(h_s)}\frac{\sigma_{zy}^*(h_s)}{\dot{u}_y(0)/c} \\
V(h_s) &= \frac{\dot{u}_y(h_s)}{\dot{u}_y(0)} = \frac{u_y(h_s)}{u_y(0)}
\end{aligned}
\qquad (31)
$$

where the asterisk, *, indicates the imaginary part of a complex quantity, i.e., u_x^*, σ_{zz}^*, and σ_{zy}^* are real quantities.

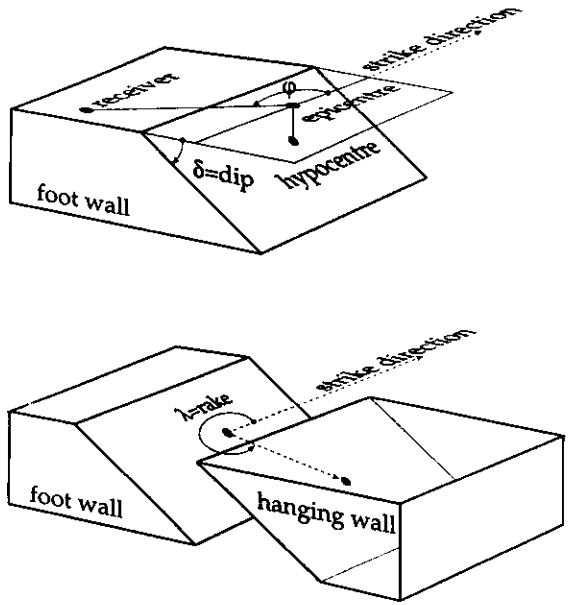

Fig. 3. Angle conventions used for the source system.

The quantity I_i in (28) are the *energy integrals* defined as

$$
\begin{aligned}
I_{1L} &= \int_0^\infty \rho(z)\left(u_y(z)/u_y(0)\right)^2 dz \\
I_{1R} &= \int_0^\infty \rho(z)\left[y_1^2(z) + y_3^2(z)\right] dz
\end{aligned}
\qquad (32)
$$

where

$$y_1 = \frac{u_z(z)}{u_z(0)}$$

$$y_3 = -i\frac{u_x(z)}{u_z(0)} = \frac{u_x{}^*(z)}{u_z(0)} \qquad (33)$$

In Eq. (28), v_g is the group velocity that can be calculated analytically from the phase velocity

$$v_g = \frac{c}{1 - \frac{\omega}{c}\frac{\partial c}{\partial \omega}} \qquad (34)$$

while C_2 indicates the phase attenuation and expresses the effect due to anelasticity. C_2 can be calculated analytically using variational techniques (e.g., Takeuchi and Saito, 1972; Aki and Richards, 1980).

For Love modes one has (Florsch et al., 1991)

$$C_{2L} = \frac{\int_0^\infty \mu B_1 B_2 \left[\frac{1}{\mu^2}\left(\frac{\sigma_{zy}{}^*}{\dot{u}_y(0)/c}\right)^2 + \left(\frac{u_y}{u_y(0)}\right)^2\right] dz}{c\int_0^\infty \mu\left(\frac{u_y}{u_y(0)}\right)^2 dz} \qquad (35)$$

where c is the phase velocity in the perfectly elastic case, while B_1 and B_2 are respectively the S-wave velocity and the S-wave phase attenuation that are related to the complex body-wave velocity (Schwab and Knopoff, 1972)

$$\frac{1}{\beta} = \frac{1}{\beta_1 + i\beta_2} = \frac{1}{B_1} - iB_2 \qquad (36)$$

For Rayleigh modes one has (Panza, 1985)

$$C_{2R} = \frac{\mathrm{Im}(I_{4R})}{2\omega k I_{3R}} \qquad (37)$$

where k is the wavenumber in the perfectly elastic case and the integrals I_{3R} and I_{4R} are defined as

$$I_{3R} = \int_0^\infty \left\{\left[(\lambda+2\mu) - \frac{\lambda^2}{(\lambda+2\mu)}\right] y_3{}^2 - \frac{1}{k}\left[y_1 y_4 - \frac{\lambda}{(\lambda+2\mu)}\right] y_2 y_3\right\} dz \qquad (38)$$

$$I_{4R} = \int_0^\infty \left\{\delta(\lambda+2\mu)\left[\frac{1}{(\lambda+2\mu)^2}\left(y_2{}^2 - 2k y_2 y_3\right) + k^2\left(1 + \frac{\lambda^2}{(\lambda+2\mu)^2}\right) y_3{}^2\right] + \right. \qquad (2.39)$$

$$\left. + \delta\mu\frac{y_4{}^2}{\mu^2} + \delta\lambda\left[\frac{2k}{(\lambda+2\mu)}\left(y_2 y_3 - k\lambda y_3{}^2\right)\right]\right\} dz$$

where

$$y_2 = \frac{\sigma_{zz}(z)}{u_z(0)} = -\frac{k\sigma_{zz}^*(z)}{\dot{u}_z(0)/c}$$

$$y_4 = -i\frac{\sigma_{zx}(z)}{u_z(0)} = \frac{k\sigma_{zx}(z)}{\dot{u}_z(0)/c} \qquad (2.40)$$

and y_1 and y_3 are defined in (33). The variational quantities in (39) are

$$\begin{aligned}
\delta(\lambda+2\mu) &= \rho\left(\alpha_1^2 - \alpha_2^2 - \bar{\alpha}^2\right) + i2\rho\alpha_1\alpha_2 \\
\delta\mu &= \rho\left(\beta_1^2 - \beta_2^2 - \bar{\beta}^2\right) + i2\rho\beta_1\beta_2 \qquad (41) \\
\delta\lambda &= \rho\left[\left(\alpha_1^2 - \alpha_2^2 - \bar{\alpha}^2\right) - 2\left(\beta_1^2 - \beta_2^2 - \bar{\beta}^2\right)\right]\left(\alpha_1^2 - \alpha_2^2 - \bar{\alpha}^2\right) + i2\rho(\alpha_1\alpha_2 - 2\beta_1\beta_2)
\end{aligned}$$

where $\bar{\alpha}$ and $\bar{\beta}$ are the P-wave and S-wave velocities in the perfectly elastic case, while for anelastic media one has (analogously to (36) for S-waves)

$$\frac{1}{\alpha} = \frac{1}{\alpha_1 + i\alpha_2} = \frac{1}{A_1} - iA_2 \qquad (42)$$

where A1 and A2 are, respectively, the P-wave velocity and the P-wave phase attenuation.

The synthetic seismogram can be obtained with three significant digits using the FT of (28) as long as the condition kr > 10 is satisfied (Panza et al., 1973), and a realistic kinematic model of a finite fault can easily be adopted (e.g., Panza and Suhadolc, 1987; Saraò et al., 1998) in conjunction with the modal summation

technique. The fault of finite length is modelled as a series of point sources on a defined grid, placed along the fault plane, with appropriate spacing. The seismogram is computed by summing the time series radiated by the single point-sources with the appropriate time-shifts that are defined by the rupture process. The resultant time series show the great influence that directivity and the distribution of energy release in time, may have on the synthesized ground motion.

3. Algorithms for laterally heterogeneous media

Linear system (1) is composed of three partial differential equations, with parameters that are dependent on the spatial variables, for which it is not always possible to find an exact analytical solution. We can distinguish between two main classes of methods that can be used to solve the system of Eqs. (1): analytical and numerical methods. It is not easy to choose which method is the best: advantages and disadvantages are related to the final goal and usually a compromise is necessary. Technically speaking, the choice depends on the ratio between the wavelength of the seismic signal and the dimensions of the lateral heterogeneities. For instance, if one wants to study the response of a complex sedimentary basin, it can be worth using a numerical approach. On the other hand, analytical methods may be certainly preferred when dealing with models with dimensions several orders of magnitude larger than the representative wavelengths of the computed signal, because of limitations in the dimensions of

the model that affect numerical techniques. To make use of the advantages of each method, analytical and numerical approaches can be combined in the so-called hybrid techniques. Typically the analytical solution is applied to the regional model characterizing the path from the source to the local area of interest, and the numerical solution is applied to model the local site conditions.

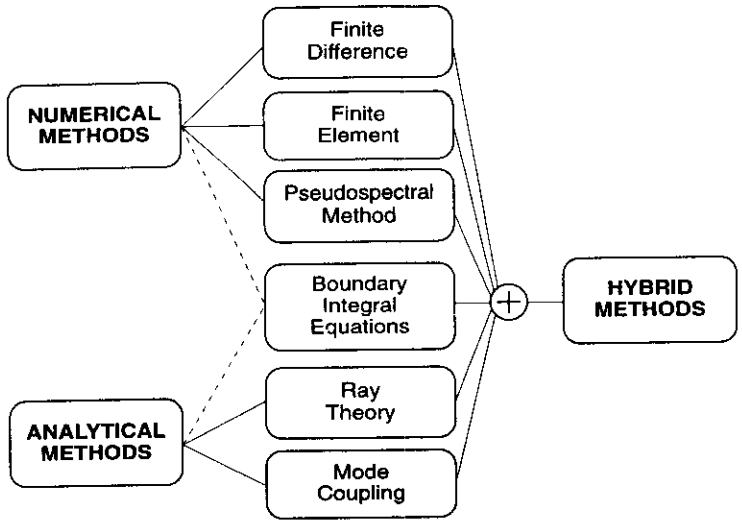

Fig. 4. Schematic diagram showing the techniques for the synthetic seismograms calculation in laterally heterogeneous media. The mode couplings techniques will be further expanded.

In Sections 3.1-3.5 we describe the methods summarized in the scheme of Fig. 4. (Methods based upon Alsop's approach that are considered in Section 4.) For hybrid techniques, in the following we concentrate just on the approach based on the modal summation technique and a finite difference scheme. The so-called Boundary Integral Equations (BIE) share elements of both subdivisions.

3.1 Numerical methods

3.1.1 Finite difference

The core of this technique is the substitution, in the wave equation, of the differential operators with finite difference operators defined by the Taylor expansion

$$u(x \pm h) = u(x) \pm \frac{du}{dx}h + \frac{1}{2}\frac{d^2u}{dx^2}(h)^2 \pm o(h^3) \tag{43}$$

In such a way the continuum is approximated by a regular grid of points.

For instance, we can define the operators of forward difference, D_+, central difference, D_0, and backward difference, D_-, that can substitute the initial first-order differential operator

$$Du(x) = \frac{du}{dx} \rightarrow \begin{cases} D_+u(x) = \dfrac{u(x+h) - u(x)}{h} \\ D_0u(x) = \dfrac{u(x+h) - u(x-h)}{2h} \\ D_-u(x) = \dfrac{u(x) - u(x-h)}{h} \end{cases} \tag{44}$$

Truncation errors have a dominant term proportional to h, h^2, and h (first, second, and first order), respectively. With a proper linear combination of the operators defined in (44) we can find the expressions for substitution of the second derivative operator, and of the operator D, to higher-order accuracy by including additional terms. We can extend the same considerations to temporal and spatial derivatives with respect to any spatial coordinate.

In the following general considerations we consider the example of the 1-D SH motion equation, assuming that the elastic parameters vary only along the x co-ordinate

$$\rho(x)\frac{\partial^2 u_y}{\partial t^2} = \frac{\partial}{\partial x}\left[\mu(x)\frac{\partial u_y}{\partial x}\right] \qquad (45)$$

To avoid the evaluation of partial derivatives with respect to μ, we can rewrite (45) using a velocity-stress formulation

$$\begin{aligned}\frac{\partial \dot{u}_y}{\partial t} &= \frac{1}{\rho(x)}\frac{\partial \sigma_{xy}}{\partial x}\\ \frac{\partial \sigma_{xy}}{\partial t} &= \mu(x)\frac{\partial \dot{u}_y}{\partial x}\end{aligned} \qquad (46)$$

Let us sample the plane (x,t) in the locations (l Δt, m Δx), where l and m are integer numbers. To determine stress and velocity in the point (m Δx) at a given instant of time ((l+1) Δt), we can approximate the system (46) by D_0 operator in space, i.e., using the values of σ_{xy} and $\dot{u}_y$ at three space-adjacent points ((m-1) Δx, m Δx, (m+1) Δx), and by D_+ operator in time

$$\begin{aligned}\frac{(\dot{u}_y)_m^{l+1} - (\dot{u}_y)_m^l}{\Delta t} &= \frac{1}{\rho_m}\frac{(\sigma_{xy})_{m+1}^l - (\sigma_{xy})_{m-1}^l}{2\Delta x}\\ \frac{(\sigma_{xy})_m^{l+1} - (\sigma_{xy})_m^l}{\Delta t} &= \mu_m\frac{(\dot{u}_y)_{m+1}^l - (\dot{u}_y)_{m-1}^l}{2\Delta x}\end{aligned} \qquad (47)$$

This system must be iterated in space and time (Aki and Richards, 1980), satisfying the proper boundary conditions. Because the truncation error, ε, grows exponentially with increasing time, the stability of the system, $1/\varepsilon$, tends to zero, making the scheme adopted in (47) always unstable. If a D_0 operator is adopted also for the time derivative, the resulting scheme is a conditionally stable one, i.e., the integration step in time must satisfy the relation

$$\Delta t < \frac{\Delta x}{\beta} \qquad (48)$$

where the boundary in the time step corresponds to the physical condition that information cannot propagate across the mesh faster than the velocity $\Delta x/\Delta t$. The stability condition (48) can be extended to a homogeneous medium with N spatial dimensions simply by dividing the right-hand side of (48) by $\sqrt{N}$. One of the most important topics for any practical application of a stable finite difference scheme, explicit in time, to a laterally varying medium, is to find the proper combination of Δx and Δt.

As for the stability criteria, the accuracy control of the adopted scheme, i.e., the rate of convergence of the numerical phase and group velocities to the correct ones, the so-called numerical dispersion, can be derived. For example, in the case of the 1-D central difference scheme for time and space which leads to condition (48), it can be demonstrated (e.g., Aki and Richards, 1980) that the accuracy of modelling the signal dispersion (grid dispersion) requires that at least 10 grid points are defined per wavelength

$$\Delta x < \frac{c\,2\pi}{10\,\omega} \qquad (49)$$

Condition (49) significantly limits the spatial extension of the structural model. Given that both (48) and (49) must be simultaneously satisfied, the lowest phase velocity drives the choice of Δx, while the highest phase velocity determines the time sampling Δt, that, due to computational limitations, is generally chosen as close as possible to the highest allowed value. Therefore the numerical error introduced varies with time.

The application of finite difference schemes to some dynamical problems described by partial differential equations may result implicit in time approaches, where the solution is obtained by solving a linear set of equations. The characteristic of such solutions is that their stability does not have to satisfy a given condition (unconditionally stable), but often no gain in accuracy is provided unless a mixed scheme is adopted.

A possibility for improving the overall accuracy of an explicit finite difference scheme is to adopt the so-called staggered grids, where the fields, velocity and stress in the case of Eqs. (44), are defined on separate grids shifted in space (Madariaga, 1976). Another approach leads to the adoption of higher-order operators (compared to (44)) for the spatial derivatives (e.g., Levander, 1988) that use more information, by means of the Taylor series, than that coming from the nearest neighbor grid points.

Among the advantages of the methods based on finite-differences schemes are the easy creation of computer codes and the possibility for treating media with spatially varying parameters compared with the signal wavelength. The drawback of the method is the requirement of huge computer CPU time and memory.

3.1.2 *Hybrid method mode summation - finite difference*

Fäh et al. (1993a,b) developed a hybrid method that combines the modal summation technique, valid for laterally homogeneous anelastic media (see Sect. 2.3), with finite difference, and optimizes the advantages of both methods. Wave propagation is treated by means of the modal summation technique from the source to the vicinity of the local, heterogeneous anelastic structure that we may want to model in detail; the particular case in which the source is located beneath the receiver can be studied with the classical propagator-matrix techniques (e.g., Haskell, 1962). A laterally homogeneous anelastic structural model is adopted, which represents the average crustal properties of the region. The generated wavefield is then introduced in the grid that defines the heterogeneous area and it is propagated according to the finite-differences scheme (see Fig. 5). A more realistic modelling of wave propagation in the regional structure can be obtained using extension of the modal summation technique to laterally heterogeneous media described in Section 4.

With this approach, source, path, and site effects are all taken into account, and it is therefore possible to carry out a detailed study of the wavefield that propagates at large distances from the epicenter. This hybrid approach has been successfully applied, for the purpose of seismic microzoning, in several urban areas like Mexico City, Rome (Fäh and Panza, 1994), Benevento (Fäh and Suhadolc, 1995; Marrara and Suhadolc, 1998), Naples (Nunziata et al., 1995) and Catania (Romanelli et al., 1998a;b) in the framework of the IUGS-UNESCO-IGCP project (Panza et al., 1999b).

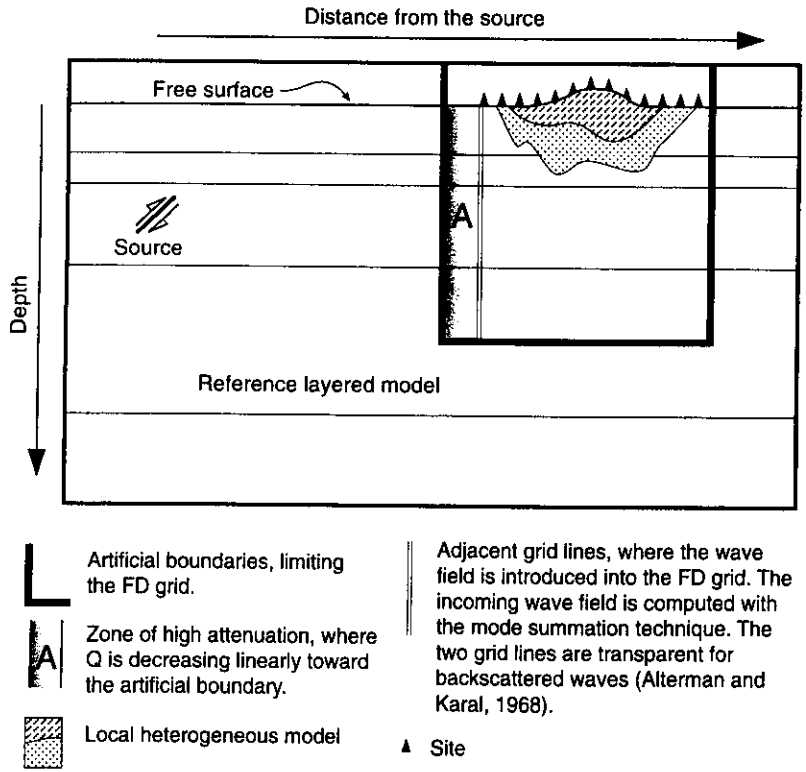

Fig. 5. Schematic diagram of the hybrid (modal summation and finite difference) method.

3.1.3 Pseudospectral method

The pseudospectral, or Fourier, method employs directly, like the finite-difference methods, the discrete form of Eq. (1): the computation domain is represented by a grid in space and an explicit scheme is adopted in the time domain. The wavefield at future time steps is calculated using the information of

the current and previous time steps; if a second order finite-difference integration scheme is used, one has

$$(\dot{u}_y)_m^{l+1} = (\dot{u}_y)_m^{l-1} + (\ddot{u}_y)_m^{l}\,\Delta t \tag{50}$$

where the same notation of Eq. (47) is adopted. In scheme (50) the time step has to be chosen in order to keep the dispersion error to an acceptable level. A criterion similar to (48) has to be adopted for a 2-D scheme:

$$\Delta t < 0.2\frac{\Delta x}{v_{max}} \tag{51}$$

The spatial derivatives that appear in Eq. (1) are analytically evaluated in the wavenumber domain, after FT, by means of orthogonal functions (e.g., Chebyshev polynomials, Fourier series; the proper choice depends on the periodicity of the problem). For example, the simplified Eq. (46) become

$$\begin{aligned}\frac{\partial \dot{\tilde{u}}_y}{\partial t} &= \frac{1}{\rho(x)}\frac{\partial \tilde{\sigma}_{xy}}{\partial x}\\ \frac{\partial \tilde{\sigma}_{xy}}{\partial t} &= \mu(x)\frac{\partial \dot{\tilde{u}}_y}{\partial x}\end{aligned} \tag{52}$$

where the notation

$$\tilde{g}(x,k,t) = \int_{-\infty}^{\infty} g(x,y,t)e^{-iky}dy \tag{53}$$

is adopted, and k is the wavenumber for the y variable. For each value of k, Eq. (52) can be solved in the wavenumber domain. In the actual calculations, k has to be discretized and such an operation is correctly done only by assuming that the source-medium configuration is periodic along the y-axis. If the periodicity length is L, one has that $k=n\Delta k$ where $\Delta k=2\pi/L$ and n is an integer. The sum over the wavenumbers can be truncated at $N\Delta k$, where N is defined as

$$N \geq 1.1 \frac{L}{\lambda_{min}} \tag{54}$$

and λ_{min} is the minimum wavelength associated to the model. Once the k components of the displacement are calculated, they can be converted to the physical domain applying a discrete inverse FT

$$u_y(x,y_d,t) = \frac{1}{L} \sum_{k=-N\Delta k}^{N\Delta k} u_y(x,k,t)\, e^{iky_d} \tag{55}$$

where y_d is the source-receiver distance.

Approximation of the spatial derivatives is infinitely accurate for periodic functions with a limited bandwidth and with spatial cutoff wavenumbers smaller than the cutoff wavenumbers of the grid, whose total dimension has to be sufficiently large to avoid space-aliasing problems (Kosloff et al., 1984). Considerations valid for the choice of the grid dimension are similar to those that are made for the finite-difference techniques when the reflections from the domain boundaries have to be avoided. Use of Cartesian grids with insufficient number of points per wavelength can lead to the diffraction of spurious waves from the staircase approximation of the interfaces between the layers present in

the model. This problem can be solved using curved grids that conform to the geometry of the actual interfaces; in such a way the local density of the grid points can be varied according to the velocity of each single layer (Nielsen et al., 1995). Other numerical techniques that have been developed for optimization of the pseudospectral methods (e.g., inclusion of the anelasticty and nonlinearity effects), are revised by Furumura and Takenaka (1996).

Comparing the efficiency of the pseudospectral method with finite difference or finite element, it appears that for a given final accuracy fewer grid points are required per wavelength (about one-fourth), but more computations are necessary at each grid point (Fornberg, 1987; Kosloff et al., 1984). In general we can state that the pseudospectral method is more efficient when implemented on fast computers and when not requiring a large amount of memory.

3.1.4 Finite Element

The finite element method can be applied to models where the geological irregularities are placed between two flat layered media, separated by vertical interfaces (Fig. 6).

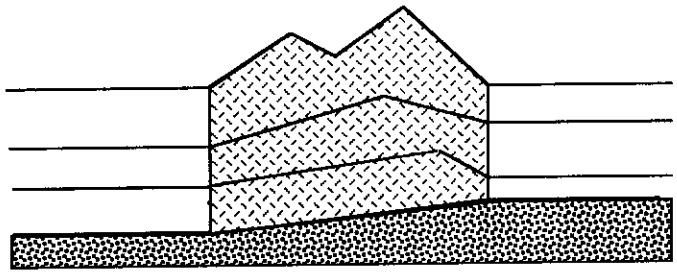

Fig. 6. Typical structural model for finite element method.

The classic procedure (Lysmer and Drake, 1972) implies a stationary analysis with finite elements of the irregular area. Special boundary conditions simulate the presence of the two layered halfspaces at each side. In the first step of the procedure the model is subdivided into a finite number of plane elements with proper values of the elastic parameters. Accuracy of the analysis depends on the detail of the mesh: as a general rule each element should not extend more than one-tenth of the wavelength of the S-wave associated with it. The elements are connected in a discrete number of nodal points. The basic assumptions are: 1) the displacements of the nodal points define the displacement field of the whole structure, and 2) all the external forces and the forces between the elements are transmitted through the nodal points.

As a consequence, the displacement field and the forces acting on the structure can be represented by two column vectors, each with dimensions equal to the number of nodal points for Love modes, and twice as big for Rayleigh modes.

For Love modes, the equations of motion can be written in the matrix form

$$[M]\{\ddot{u}_y\}+[K]\{u_y\}=\{Q\} \qquad (56)$$

where the matrices M and K are the mass and the force matrix, respectively, and contain information relative to (a) the elastic parameters of the model, (b) the excitation of one of the regular structures due to the seismic source and (c) the boundary conditions. Equation (56) forms a system of second-order differential equations with constant coefficients, and can be solved with several numerical techniques.

The finite element technique is affected by the same kind of limitations described for finite difference: for complicated models it requires huge amounts of CPU time and memory. On the other hand, being a flexible method, it is a very good choice for seismic engineering studies such as the analysis of soil-structure interaction (Wolf and Song, 1996).

3.2 Boundary Integral Equations (BIE)

In this method the equations of motion are written in the integral form

$$\varphi(x)=f(x)+\int_a^x K(x,t)\varphi(t)dt \qquad (57)$$

(named Volterra equation of the second type) where $\varphi(x)$ is the unknown function and K(x,t), called "kernel", and f(x) are known functions. An integral equation associates the unknown function not only with its values in the neighboring points but in a whole region. The boundary conditions are contained within the equation, through the values assumed by the kernel, rather than applied at the end of the solution procedure.

To describe this approach in the field of seismology we follow Bouchon and Coutant (1994), and we consider SH-waves in the simple configuration shown in Fig. 7.

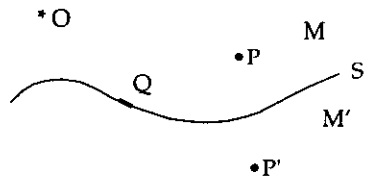

Fig. 7. Starting configuration of the BIE method.

The source of the elastic perturbation is placed at point O of medium M, and it generates at point P a direct wavefield $V_0(P)$. The wavefield diffracted in medium M' from the interface S, separating M and M', can be described as a radiation generated by secondary sources distributed along the interface. Therefore the wavefield in P can be described as

$$V(P) = V_0(P) + \int_S \sigma(Q)\, G(P,Q)\, dQ \tag{58}$$

where $\sigma(Q)$ is a density function of the source that represents the force of the wavefield diffracted from point Q, and G(P,Q) is the wavefield generated in P by a unit source placed in Q (it is also known as the *Green function*).

Analogously, the diffracted wavefield in P' is

$$V'(P') = \int_S \sigma'(Q)\, G'(P',Q)\, dQ \tag{59}$$

where G' is the Green function of M'.

The next step in obtaining a numerical solution is the discretization of the surface integral, approximating the surface S with N elements of area ΔS_i, for which the source density functions are assumed constant. Supposing that P and P' are lying, at the same point Q, on the two sides of the interface, Eqs. (58) and (59) become

$$\begin{aligned} V(Q_j) &= V_0(Q_j) + \sum_{i=1}^{N} \sigma_i \int_{\Delta S_i} G(Q_j,Q)\, dQ \\ V'(Q_j) &= \sum_{i=1}^{N} \sigma'_i \int_{\Delta S_i} G'(Q_j,Q)\, dQ \end{aligned} \tag{60}$$

The continuity condition across the interface of displacements $V(Q_j) = V'(Q_j)$, and of stresses $T(Q_j) = T'(Q_j)$, leads to a system of 2N equations with 2N unknowns represented by the source density functions. To solve the integrals of (60) we need the expression for the Green functions. Usually the discrete wavenumber method is adopted (Bouchon and Aki, 1977), supposing that the medium is periodic and avoiding the occurrence of mathematical and numerical singularities often associated with pure BIE techniques. For instance, in the frequency domain the Green function, when considering SH-waves, can be written as (Bouchon and Aki, 1977)

$$G'(Q_j,Q) = \frac{1}{2ip\beta^2 L} \sum_{n=-M}^{M} \frac{\exp\left(-i\gamma_n \left|z_j - z_Q\right|\right) \exp\left(-ik_n \left|x_j - x_Q\right|\right)}{\gamma_n} \tag{61}$$

where (x_j, z_j) and (x_Q, z_Q) are the coordinates of Q_j and Q, respectively, ρ is the density of the medium, β is the shear wave velocity, L is the length of the medium periodicity, and M is an integer big enough to guarantee the convergence of the series, and

$$\begin{aligned} k_n &= \frac{2\pi}{nL} \\ \gamma_n &= \left(\frac{\omega^2}{\beta} - k_n^2\right), \quad \mathrm{Im}(\gamma_n) \le 0 \end{aligned} \tag{62}$$

When surface S degenerates into a plane, the Green functions are those of a stratified medium and can be computed analytically using the formalism described in Sect. 2.3.

The BIE method has several advantages with respect to the so-called domain techniques (finite difference and finite element), since it requires the discretization of a surface rather than of a volume, but it is limited to relatively simpler models than those treatable by numerical techniques. Solution of the equation system (60) becomes heavy in terms of computational time when many irregular surfaces are present in the model. The BIE method has been successfully applied in seismology to the study of wave propagation in irregular media (e.g., Bouchon and Coutant, 1994), and its variants (Boundary Element Methods) are used in engineering analysis (Maier et al., 1991).

3.3 Analytical methods

Among the methods that attempt to solve equations of motion in flat laterally heterogeneous media with numerical techniques applied to analytical solutions, we can distinguish two main complementary classes: methods based on ray theory and methods based on mode coupling.

Ray methods are based on the principles of classic geometrical optics. The synthetic signal is built up as a superposition of rays, reflected and transmitted according to the Snell law. The modal approaches, that will be more extensively analyzed, share the idea that the unknown wavefields are built up as a superposition of the normal modes characteristic of the medium. The choice between the two physical representations of the wavefield depends upon the kind of data that one wants to model. It depends on wether one is interested in the dispersive features of the complete signal or in the study of the arrival times of some early phases. The number of rays necessary to model the late arrivals in one seismogram becomes huge and difficult to handle. Furthermore, at long

periods, ray theory can no longer be applied, being rigorously defined at infinite frequency, and problems arise for peculiar transition zones, known as caustics. On the other hand the number of modes necessary to describe adequately the first arrivals in a seismogram could be too large to be efficiently handled. The duality between rays (P-SV, SH-waves) and modes (Rayleigh, Love) is evident also from the formal point of view: Marquering (1996) has shown that any of the two representations can be written as the FT of the other.

3.4 Ray theory

Ray theory is based on a hypothesis (ansatz) of the form of the solution of the elastic equations of motion (Babich, 1956):

$$\mathbf{u}(\mathbf{x},\omega) = \mathbf{A}(\mathbf{x},\mathbf{x}_0,\omega)\frac{e^{i\omega\theta(\mathbf{x},\mathbf{x}_0)}}{\sqrt{J(\mathbf{x},\mathbf{x}_0)}} \qquad (63)$$

where $\theta(\mathbf{x},\mathbf{x}_0)$ is called phase, and represents the time necessary for the wave to travel from point $\mathbf{x}_0$ to point $\mathbf{x}$, and J is the geometrical decay of the wavefronts.

Expression (63) does not contain any approximation since $\mathbf{A}$ is a generic function of $\mathbf{x}$ and ω. To obtain the approximation of the classic ray theory we have to expand the amplitude vector in a series of inverse powers of ω

$$\mathbf{A}(\mathbf{x},\mathbf{x}_0,\omega) = S(\omega)\sum_{i=0}^{\infty}\mathbf{A}_i(\mathbf{x},\mathbf{x}_0)\,\omega^{-i} \qquad (64)$$

where $S(\omega)$ is the FT of the source time function. If we consider only the first term in (64), then (63) becomes:

$$\mathbf{u}(\mathbf{x},\omega) = S(\omega)\mathbf{A}_0(\mathbf{x},\mathbf{x}_0)\frac{e^{i\omega\theta(\mathbf{x},\mathbf{x}_0)}}{\sqrt{J(\mathbf{x},\mathbf{x}_0)}} \qquad (65)$$

and represents an approximation of the solution of the wave equation valid only at high frequencies, when the higher terms can be neglected in (65). Furthermore, we assume that the terms $\mathbf{A}_0$, J and θ in (65) are smoothly varying functions of the spatial co-ordinates. In such a way (65) becomes a form of the solution suitable for computation of a synthetic seismogram, since its FT can very easily be computed.

Introducing (65) in the equations of motion, we obtain an independent set of solutions that, for SH-waves, can be written as (Cerveny, 1987):

$$(\nabla\theta)^2 = \frac{1}{\beta} \qquad (66)$$
$$\mathbf{A}_0 \cdot (\nabla\theta) = 0$$

also called the eikonal equation.

We define the surface $\theta(\mathbf{x}) = \text{const}$ as a wavefront. The slowness vector, $\mathbf{p} = \nabla\theta$, is normal to the wavefront and has modulus $1/\beta$: its trajectory describes a ray. The horizontal component of p is analogous to the phase velocity c, equal to $\sin\theta/\beta$ (see Fig. 2), for the mode with horizontal wavenumber $k=\omega/c$. Given an initial wavefront $t_0 = \theta(\mathbf{x},\mathbf{x}_0)$, the rays and the following wavefronts can be computed using (66) with the so-called *ray tracing*. As in geometrical optics, an alternative to the above mentioned approach, based on Huygens principle, is represented by a variational formulation corresponding to the Fermat principle: the ray corresponds to the trajectory between two given points for which the travel time is minimum.

Expression (65) can become unstable or singular under certain conditions, for instance, in the vicinity of a caustic, where ray theory predicts an infinite

amplitude. Furthermore, classic ray theory is extremely sensitive to small local perturbations of the velocity field, because of the crucial assumption of infinite frequency in (65). The so-called spectral methods furnish a partial solution to these problems, keeping intact the physical meaning of ray theory. In a spectral method, the wavefield is not computed using (65) directly, but rather by a sum of ray beams having the form of (65). Among the spectral methods, the most popular is the WKBJ method (acronym for G. Wentzel, H. Kramers, L. Brillouin, and H. Jeffreys), where the source is represented as a sum of Snell waves, each one propagating independently from the other ones. The seismogram is then calculated summing all the propagated waves (Chapman, 1978).

Recently, advances in ray theory have been obtained applying the ray perturbation theory. In this way the techniques known as paraxial rays and Gaussian beams have been developed (Farra and Madariaga, 1987; Madariaga, 1989). The ray perturbation theory is used for evaluation of ray amplitude and for solving iteratively ray tracing problems. The most important perturbations are those related to the initial and final values of the position and propagation velocity. Ray perturbation theory also computes the trajectories of paraxial rays that propagate in the neighborhood of a reference ray. The study of paraxial rays simplifies computation of geometrical spreading and facilitates better following the rays crossing a curved interface.

In summary, the fundamental limitations of the techniques based on ray theory are connected with the dimensions of the heterogeneities that must be much larger than the dominating wavelength of the considered waves. Advantages with respect to numerical techniques are that models whose lateral dimensions are several orders of magnitude larger than representative

wavelengths of the computed signal can be considered. Furthermore, ray theory can easily separate the different phases that contribute to the wavefield, since one can follow, using an intuitive physical approach, the way energy associated with seismic waves propagates through the medium. With these considerations, one can understand the importance of ray theory for seismic tomography studies based on body wave arrivals, bearing in mind the difficulty of recognizing the phases in the synthesised seismogram (a feasible operation only when travel times are reliable).

3.5 Mode coupling

Whenever the source-receiver configuration is like the one shown in Fig. 5, surface waves (fundamental and first few higher modes) represent the longest and strongest portion of a seismic signal generated from an earthquake. These waves constitute the dominant part of the seismogram and thus supply the data with the most favorable signal/noise ratio. Therefore analysis of surface waves is crucial for gaining knowledge of the elastic and anelastic properties of the areas crossed by the waves (Snieder, 1986; Nolet, 1990; Du et al., 1998), and for seismic hazard studies, with engineering implications (see Sect. 5).

Surface waves cannot be modelled easily with methods based on ray theory, because of computational problems: it is not a theoretical limitation but a practical one. There is no doubt that the modal summation is the most suitable technique for modelling the dominant part of seismic ground motion. The key point of the technique is the description of the wavefield as a linear combination of given base functions: the normal modes characteristic of the medium. In the case of the Earth, the modal summation technique is an exact method, since for a

finite body the normal modes form a complete set. If we approximate the Earth with a flat layered halfspace, the completeness of normal modes is no longer satisfied, since they are associated only with the discrete part of the wavefield spectrum. Nevertheless this limitation can be overcome or controlled using several procedures described in Sects. 3.5.1-3.5.3 and 4.

Extension of the modal summation technique, described in Section 2.3, to laterally heterogeneous media can be performed following different procedures. The choice of the most suitable procedure must take into account the geometry and the physical properties of the medium.

In the following, the term "intracoupling" refers to the coupling of a mode with itself, while "intercoupling" indicates the coupling of a mode with another one (Snieder, 1986).

3.5.1 WKBJ method

The main assumption of WKBJ method, widely used in seismology (Woodhouse, 1974), is that the lateral variations of the elastic parameters are *regular* (compared to the wavelength). Once this hypothesis is satisfied, we can assume that the energy carried by each mode in a given structure is neither reflected nor transmitted to other modes. In other words, modes are not coupled; each mode propagates with a wavenumber driven by the local structure. The amplitude is not changed, while phase perturbations are computed by averaging the whole source-receiver path, neglecting the horizontal position of the heterogeneities.

Let us assume that the solution of Eq. (11), associated with the m-th mode, is ${}^{m}u_{y}^{0}$. Asymptotic expression of the perturbed mode at point x, due to regular lateral variations, can be written as

$$ {}^{m}u_{y}(x) = {}^{m}u_{y}^{0}(x)\exp\left[i({}^{m}\delta k)x\right] \tag{67} $$

where

$$ {}^{m}\delta k(x) = \int_{0}^{\infty}\left(\frac{\partial({}^{m}k)}{\partial\rho}\delta\rho + \frac{\partial({}^{m}k)}{\partial\alpha}\delta\alpha + \frac{\partial({}^{m}k)}{\partial\beta}\delta\beta\right)dz \tag{68} $$

and $\delta\rho$, $\delta\alpha$, and $\delta\beta$ are the perturbations of the elastic parameters, at point x, with respect to the reference model.

The total wavefield computed at a distance r from the source can be written as the sum of the contributions of each single mode

$$ u_{y}(r) = \sum_{m=1}^{\infty} {}^{m}u_{y}^{0}(r)\exp\left[i({}^{m}\overline{\delta k})x\right] \tag{69} $$

where

$$ {}^{m}\overline{\delta k} = \frac{1}{r}\int_{0}^{r} {}^{m}\delta k(x)dx \tag{70} $$

Expanding the term $\exp\left[i({}^{m}\delta k)x\right]$, expression (69) can be seen as an infinite sum of multiple intracoupling terms.

The WKBJ method has been used for large-scale inversions (Nolet et al., 1986), but in some cases it can be unrealistic, as true phase perturbations must depend upon the position of the heterogeneities along the path (Marquering, 1996). In spite of this limitation, including amplitude variations of the seismogram in the formalism facilitates performing an efficient fully analytical waveform inversion scheme (Du and Panza, 1999) at a regional scale.

3.5.2 The Born approximation

Let us relate the perturbations of the elastic parameters of the laterally heterogeneous medium to the unperturbed medium as follows

$$ \begin{cases} \rho(x,z) = \rho_{0}(z) + \varepsilon\delta\rho(x,z) \\ \alpha(x,z) = \alpha_{0}(z) + \varepsilon\delta\alpha(x,z) \\ \beta(x,z) = \beta_{0}(z) + \varepsilon\delta\beta(x,z) \end{cases} \tag{71} $$

The transmitted wavefield can then be written as follows

$$ \mathbf{u} = \mathbf{u}_{0} + \varepsilon\delta\mathbf{u}(\delta\rho,\delta\alpha,\delta\beta) + o(\varepsilon^{2}) \tag{72} $$

Perturbation of the wavefield in (72) can be written as a function of the so-called "scattering matrix" that describes the coupling between modes (Snieder, 1986). If we assume normal incidence and that the lateral variations exist only along the x direction, there are no conversions between Love and Rayleigh modes both in the transmitted and in the reflected wavefields.

If the perturbations are weak, i.e., if in (71) ε is small enough, then the contributions due to multiple scattering can be neglected. In the Born approximation only the mode coupling of the first order is considered: the total

contribution is given by the unperturbed mode plus a term that describes the coupling between modes, due to the lateral heterogeneity. If the intercouplings are neglected, the Born approximation coincides with the WKBJ method (Marquering, 1996). The main limit of the Born approximation is that it can correctly treat only small perturbations of the wavefield.

3.5.3 *Invariant Imbedding Technique (IIT)*

Kennett (1984) developed a representation of the mode coupling where the wave equation is expressed by a set of first-order coupled differential equations. The complete wavefield in a laterally heterogeneous medium is written as a properly weighted superposition of the modes of a reference model. This method has been extended to tridimensionally heterogeneous media by Bostock (1992). In these techniques, named IIT, the effects due to lateral heterogeneity along the source-receiver path are described by coupling mode coefficients, c_i in (73) and (74) that depend on the local structures.

The unperturbed displacement can be written as (Marquering and Snieder, 1995)

$$ {}^{m}u_y^0(r,z) = \sum_{i=1}^{N} c_i^0(r)\,\phi_i^0(z)\,\frac{e^{ik_i r}}{\sqrt{kr}} \qquad (73) $$

where $c_i^0(r)$ is the modal coefficient, constant for laterally homogeneous media, relative to the i-th mode.

The modal coefficients, that are complex, can be defined for the transmitted and reflected wavefield from the heterogeneity $c_i^+(r)$, $c_i^-(r)$. If the heterogeneity is limited in space, the coefficients can be defined by transmission and reflection

matrices (analogousto the scattering matrix) linking the incoming modes with the modes outgoing from the heterogeneity (transmitted and reflected).

The mode at the receiver is given by the sum of the unperturbed mode and the effects due to multiple couplings (forward and backward). If reflections and the intercouplings are neglected, the IIT method coincides with the WKBJ method. Neglecting the reflections and second-order couplings makes IIT coincident with the Born approximation (Marquering and Snieder, 1995).

The limitation of this method is the considerable computational effort necessary to solve the complete problem. To overcome this, several techniques have been developed, based on the IIT method. Among them we mention here the Matrix Exponent Approximation (MEA) (Marquering and Snieder, 1995), where the reflection matrix is neglected and the transmission coefficient can be written as

$$ c_i^+(r) = c_i^0 + \sum_{m=1}^{N} M_{im} c_m^0 + \sum_{m=1}^{N}\sum_{k=1}^{N} M_{im} M_{mk} c_k^0 + \cdots \qquad (74) $$

where the first term represents the unperturbed term, excited at the source and propagated to the receiver. The second term represents all the first-order couplings with the i-th mode. The third term in (74) is the contribution to the i-th mode of the k-th mode coupled with the m-th and represents the second order coupling. The MEA method is a powerful tool for computation of the arrivals associated mainly with body waves, but it is computationally expensive whenever the investigated media are characterized by strong lateral discontinuities.

A technique quite similar to IIT has been developed by Odom (1986) and by Maupin (1988). In their formulation the base functions appearing in (73) are those relative to the local structure and therefore depend on the horizontal coordinate.

4. Analytical computation of the mode coupling coefficients

In Section 3 we described several methods that can be used to extend the modal summation technique to laterally heterogeneous media. These techniques share the idea that the unknown wavefield generated by the lateral heterogeneities is written as a linear combination of base functions representing the normal modes (Love and Rayleigh) of the considered structure, therefore the problem reduces to the computation of the coefficients of this expansion.

If we consider a heterogeneous medium made of two layered quarterspaces in welded contact, the traditional method (Alsop, 1966; McGarr and Alsop, 1967) assumes that at a given frequency the set of eigenfunctions is complete for each of the two quarterspaces. If this condition is satisfied, then the unknowns of the problem, i.e., the transmission and reflection coefficients, can be computed assuming the proper continuity conditions at the vertical interface. There are two problems with this approach: (1) at a given frequency the discrete spectrum of the eigenfunctions is not complete and the continuous spectrum should be included, and this requires the cumbersome computation of branch-line integrals; and (2) expansion in series of the base functions can be carried out for a

finite number of terms, so that a control over the approximations introduced becomes necessary.

In a modal approach alternative to the original Alsop's method, the coupling coefficients for the modes transmitted and reflected at the vertical interface are computed, and the outgoing (inhomogeneous) surface waves are obtained as a superposition of homogeneous and inhomogeneous waves using Snell's law at each section (supposed infinite) of the vertical interface (Alsop et al., 1974). The main objection to this approach is that the horizontal boundary conditions are no longer satisfied and therefore some diffracted waves, near the vertical interface, are not properly taken into account. Nevertheless it is possible to estimate the severity of the approximation introduced by checking the energy balance between the incoming and the outgoing wavefields.

In this Section, starting from the original formulation by Gregersen and Alsop (1974), we describe the analytical solution of the problem associated with SH waves. The results shown include the effect of topography (Romanelli et al., 1996). For the P-SV problem, the analytical solution is given by Vaccari et al. (1989) for poissonian media, and extended to non-poissonian media by Romanelli et al. (1997).

The basic model treated in this Section consists of two layered quarterspaces in welded contact, but the formalism can be extended to any laterally heterogeneous structure using a series of 1-D layered structures in welded contact at the vertical interfaces. In Sect. 5 this approach will be used to model the wavefield in sedimentary basins.

4.1 Coupling coefficients for Love modes

Let us consider a mode of medium I, incident on the vertical interface between medium I and medium II as shown in Fig. 8. We consider normal incidence at the vertical interface, but the case of oblique incidence can be treated as well.

The wavefield associated with the incoming mode can be described by the stress-displacement vector defined as

$$\mathbf{A}_I=(u_{xI},\ u_{yI},\ u_{zI},\ \sigma_{xxI},\ \sigma_{yxI},\ \sigma_{zxI}) \qquad (75)$$

where $\mathbf{u}_I = (u_{xI},\ u_{yI},\ u_{zI})$ is the displacement vector and σ_{ixI} (i= x, y, z) are the three components of the stress acting on the vertical interface defined by the equation x=0.

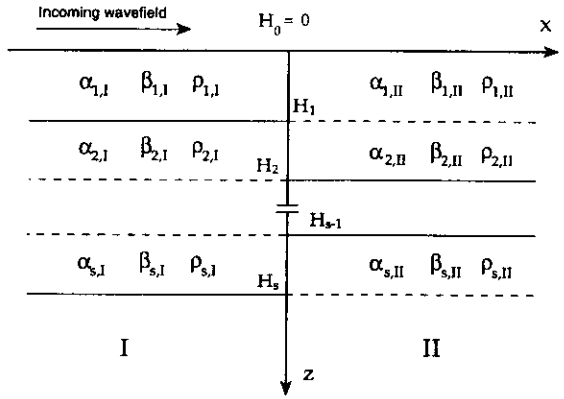

Fig. 8. 2-D model. Dashed lines represent the fictitious interfaces introduced to line up the layers of the two quarterspaces.

Similarly we can define the stress-displacement vector associated with a mode belonging to medium II

$$\mathbf{A}_{II}=(u_{xII},\ u_{yII},\ u_{zII},\ \sigma_{xxII},\ \sigma_{yxII},\ \sigma_{zxII}) \qquad (76)$$

The projection of vector (75) on the vector (76) can be defined as follows (Herrera, 1964)

$$\langle \mathbf{A}_I, \mathbf{A}_{II} \rangle = \frac{1}{2i}\int_0^{\infty} [u_{xI}\bar{\sigma}_{xxII} + u_{yI}\bar{\sigma}_{yxII} + u_{zI}\bar{\sigma}_{zxII} + \\ -\bar{u}_{xII}\sigma_{xxI} - \bar{u}_{yII}\sigma_{yxI} - \bar{u}_{zII}\sigma_{zxI}]dz \qquad (77)$$

where (here and in the following) the bar denotes the complex conjugation operator. This scalar product fully describes the orthogonality relation for the considered eigenfunction sets (see Appendix A). Actually, if vectors $\mathbf{A}^{(n)}$ and $\mathbf{A}^{(m)}$ represent two modes (n and m) of the same medium at the same frequency, then if $n \neq m$ $\langle \mathbf{A}^{(n)}, \mathbf{A}^{(m)} \rangle = 0$, while if n=m (Alsop, 1966)

$$\langle \mathbf{A}^{(m)}, \mathbf{A}^{(m)} \rangle = \pm \frac{1}{\omega} E \qquad (78)$$

where E is proportional to the energy flux carried by the incoming mode crossing the vertical interface. The sign in (78) is chosen according to the propagation direction: (+) for transmitted and (-) for reflected waves.

The stress-displacement vectors associated with transmitted and reflected modes, indicated as

$$\mathbf{A}_T=(u_{xT}, u_{yT}, u_{zT}, \sigma_{xxT}, \sigma_{yxT}, \sigma_{zxT}) \tag{79}$$

$$\mathbf{A}_R=(u_{xR}, u_{yR}, u_{zR}, \sigma_{xxR}, \sigma_{yxR}, \sigma_{zxR}) \tag{80}$$

can be regarded as a superposition of propagating modes of medium II and medium I respectively. In each horizontal section the displacement, due to a Love mode, can be written as (see Eq. 14) :

$$u_y(x,z,t) = \left[A_s \cos\left(kr_{\beta s} z\right) + B_s \sin\left(kr_{\beta s} z\right)\right] e^{i(\omega t - kx)} \tag{81}$$

where A_s and B_s are the layer constants and

$$r_{\beta s} = \sqrt{\frac{c^2}{\beta_s^2} - 1} \qquad \text{if } c>\beta_s$$

$$r_{\beta s} = -i\sqrt{1 - \frac{c^2}{\beta_s^2}} \qquad \text{if } c<\beta_s \tag{82}$$

where c is the phase velocity and β_s is the S-wave velocity in section s. Therefore, in each horizontal section a Love mode can be considered as a superposition of SH-waves incident on the vertical interface with an angle

$$\theta_s = \cos^{-1}\left(\frac{\beta_s}{c}\right) \tag{83}$$

From (83) we can see that, according to the values of c, which for a given mode and a given frequency are the same for all the sections, and and according to the S-wave velocity, which generally varies with varying sections, the resulting SH-waves in each section can be homogeneous (θ_s real) or inhomogeneous (θ_s imaginary). Now the transmission and reflection coefficients can be computed in each horizontal section using Snell's law, which is valid for an infinite surface of contact. For a homogeneous SH-wave with unitary amplitude the coefficients are (Aki and Richards, 1980)

$$b_s = \frac{2\rho_{s,I}\beta_{s,I}\cos\theta_{s,I}}{\rho_{s,I}\beta_{s,I}\cos\theta_{s,I} + \rho_{s,II}\beta_{s,II}\cos\theta_{s,II}}$$

$$a_s = \frac{\rho_{s,I}\beta_{s,I}\cos\theta_{s,I} - \rho_{s,II}\beta_{s,II}\cos\theta_{s,II}}{\rho_{s,I}\beta_{s,I}\cos\theta_{s,I} + \rho_{s,II}\beta_{s,II}\cos\theta_{s,II}} \tag{84}$$

where θ_I and θ_{II} are the angles of incidence and refraction respectively. Iterating the procedure for each horizontal section we can define the vectors (4.5) and (4.6). The procedure is approximated, since the horizontal boundary conditions are no longer satisfied and not all the diffracted waves are included in the computations. In Sect. 4.2.1 we shall describe a method that allows us to estimate the level of the approximation introduced.

The transmission coupling coefficient, i.e., the quantity that describes how the amplitude of mode m' in medium II is excited by the incoming mode m of medium I is (Vaccari et al., 1989)

$$\gamma_T^{(m,m')} = \frac{\langle \mathbf{A}_T^{(m)}, \mathbf{A}_{II}^{(m')} \rangle}{\langle \mathbf{A}_I^{(m)}, \mathbf{A}_I^{(m)} \rangle^{1/2} \langle \mathbf{A}_{II}^{(m')}, \mathbf{A}_{II}^{(m')} \rangle^{1/2}} \tag{85}$$

If we prefer to consider an incoming mode with unit surface amplitude we need to define a normalization coefficient and the following quantity must be used

$$\Gamma_T^{(m,m')} = \gamma_T^{(m,m')} \frac{\langle \mathbf{A}_I^{(m)}, \mathbf{A}_I^{(m)} \rangle^{1/2}}{\langle \mathbf{A}_{II}^{(m')}, \mathbf{A}_{II}^{(m')} \rangle^{1/2}} = \frac{\langle \mathbf{A}_T^{(m)}, \mathbf{A}_{II}^{(m')} \rangle}{\langle \mathbf{A}_{II}^{(m')}, \mathbf{A}_{II}^{(m')} \rangle} \tag{86}$$

The reflection coupling coefficient can be defined as

$$\gamma_R^{(m,m')} = \frac{\langle \mathbf{A}_R^{(m)}, \mathbf{A}_I^{(m)} \rangle}{\langle \mathbf{A}_I^{(m)}, \mathbf{A}_I^{(m)} \rangle^{1/2} \langle \mathbf{A}_{II}^{(m')}, \mathbf{A}_{II}^{(m')} \rangle^{1/2}} \tag{87}$$

while if we consider an incoming mode with unit surface amplitude

$$\Gamma_R^{(m,m')} = \gamma_R^{(m,m')} \frac{\langle \mathbf{A}_{II}^{(m')}, \mathbf{A}_{II}^{(m')} \rangle^{1/2}}{\langle \mathbf{A}_I^{(m)}, \mathbf{A}_I^{(m)} \rangle^{1/2}} = \frac{\langle \mathbf{A}_R^{(m)}, \mathbf{A}_I^{(m)} \rangle}{\langle \mathbf{A}_I^{(m)}, \mathbf{A}_I^{(m)} \rangle} \tag{88}$$

From (88) and considering the orthogonality relations holding at a fixed frequency (Romanelli et al., 1996), it can be shown that the only non-zero reflection coefficients are those relative to the coupling of homologous modes, i.e., the intracoupling coefficients.

For Love waves, vectors (75), (76), and (79) are:

$$\mathbf{A}_I = (0, u_{yI}, 0, 0, \sigma_{yxI}, 0) \tag{89}$$

$$\mathbf{A}_{II} = (0, u_{yII}, 0, 0, \sigma_{yxII}, 0) \tag{90}$$

$$\mathbf{A}_T = (0, u_{yT}, 0, 0, \sigma_{yxT}, 0) \tag{91}$$

since in the case of normal incidence there is no conversion of SH-waves into P-SV waves. The scalar product (77) becomes

$$\langle \mathbf{A}_I, \mathbf{A}_{II} \rangle = \frac{1}{2i} \int_0^\infty \left[u_{yI} \bar{\sigma}_{yxII} - \bar{u}_{yII} \sigma_{yxI} \right] dz \tag{92}$$

Remembering that

$$\sigma_{yx} = \mu \frac{du_y}{dx} = -ik\mu u_y \tag{93}$$

the two products in the denominator of (85) can be written as

$$\langle \mathbf{A}_I^{(m)}, \mathbf{A}_I^{(m)} \rangle = k_I^{(m)} \int_0^\infty \mu_I \left(u_{yI}^{(m)} \right)^2 dz = \omega v_{gI}^{(m)} I_{II}^{(m)} \tag{94}$$

$$\langle \mathbf{A}_{II}^{(m')}, \mathbf{A}_{II}^{(m')} \rangle = k_{II}^{(m')} \int_0^\infty \mu_{II} \left(u_{yII}^{(m')} \right)^2 dz = \omega v_{gII}^{(m')} I_{III}^{(m')} \tag{95}$$

where I_1 and v_g are, respectively, the energy integral and the group velocity of the Love mode at angular frequency ω. These two spectral quantities, defined by Eqs. (32) and (34) in Sect. 2.3.1, can be quickly and accurately computed using the algorithms already available for the case of a layered halfspace.

The numerator of (85) is given by

$$\left\langle \mathbf{A}_{\mathrm{I}}^{(m)}, \mathbf{A}_{\mathrm{II}}^{(m')} \right\rangle = \frac{\left(k_{\mathrm{I}}^{(m)} + k_{\mathrm{II}}^{(m')}\right)}{2} \int_0^{\infty} \mu_{\mathrm{II}} \left(u_{y\mathrm{I}}^{(m)} u_{y\mathrm{II}}^{(m')} \right) dz \tag{96}$$

If we introduce in the two quarterspaces some horizontal interfaces so that the layer thickness is the same at the two sides of the vertical interface (see Fig. 8), expression (96) can be written as

$$\sum_{s=0}^{S-1} \mu_{s,\mathrm{II}} b_s^{(m)} \int_{H_s}^{H_{s+1}} \left(u_{y\mathrm{I}}^{(m)} u_{y\mathrm{II}}^{(m')} \right) dz + \mu_{S,\mathrm{II}} b_S^{(m)} \int_{H_S}^{\infty} \left(u_{y\mathrm{I}}^{(m)} u_{y\mathrm{II}}^{(m')} \right) dz \tag{97}$$

where coefficients b_s are defined in (84). From (97) we can see that the integrals, that must be computed in each horizontal section, are

$$\int_0^{d_s} \left(u_{y\mathrm{I}}^{(m)} u_{y\mathrm{II}}^{(m')} \right) dz \qquad d_s = H_{s+1} - H_s \tag{98}$$

and using (81), for instance when $c > \beta_{s\mathrm{I}}$ and $c > \beta_{s\mathrm{II}}$, (98) becomes

$$\begin{aligned} &\int_0^{d_s} \left(\cos\left(k_{\mathrm{I}} r_{\beta \mathrm{I} s} z\right) \cos\left(k_{\mathrm{II}} r_{\beta \mathrm{II} s} z\right) \right) dz + w_1 \int_0^{d_s} \left(\cos\left(k_{\mathrm{I}} r_{\beta \mathrm{I} s} z\right) \sin\left(k_{\mathrm{II}} r_{\beta \mathrm{II} s} z\right) \right) dz + \\ &+ w_2 \int_0^{d_s} \left(\sin\left(k_{\mathrm{I}} r_{\beta \mathrm{I} s} z\right) \cos\left(k_{\mathrm{II}} r_{\beta \mathrm{II} s} z\right) \right) dz + w_3 \int_0^{d_s} \left(\sin\left(k_{\mathrm{I}} r_{\beta \mathrm{I} s} z\right) \sin\left(k_{\mathrm{II}} r_{\beta \mathrm{II} s} z\right) \right) dz \end{aligned} \tag{99}$$

where w_i are constants, and the analytical solution is immediately available. When dealing with inhomogeneous waves on both sides of the vertical interface, expression (99) is still valid but the hyperbolic functions must be used instead of the corresponding trigonometric ones. When the integrals must be computed over the depth occupied by one of the terminating homogeneous halfspaces, their argument involves decaying exponential functions. For instance, if $\alpha_{S\mathrm{II}} < \beta_{S\mathrm{II}} < c$, the integrals assume the form

$$\int_0^{d_s} \left(e^{-i k_{\mathrm{I}} r_{\beta \mathrm{I} s} z} \cos\left(k_{\mathrm{II}} r_{\beta \mathrm{II} s} z\right) \right) dz \quad \text{or} \quad \int_0^{d_s} \left(e^{-i k_{\mathrm{I}} r_{\beta \mathrm{I} s} z} \sin\left(k_{\mathrm{II}} r_{\beta \mathrm{II} s} z\right) \right) dz \tag{100}$$

Finally, when the two terminating homogeneous halfspaces are in contact, the integral is

$$\int_0^{\infty} \left(e^{-i k_{\mathrm{I}} r_{\beta \mathrm{I} s} z} e^{-i k_{\mathrm{II}} r_{\beta \mathrm{II} s} z} \right) dz \tag{101}$$

4.1.1 Energy conservation

The condition of welded contact between medium I and medium II implies that the energy flux (incident, transmitted and reflected) across the vertical interface must be preserved

$$\langle \mathbf{A}_I, \mathbf{A}_I \rangle = \langle \mathbf{A}_R, \mathbf{A}_R \rangle + \langle \mathbf{A}_T, \mathbf{A}_T \rangle \tag{102}$$

The continuity conditions at the vertical interface are, for displacement and stress components

$$\mathbf{u}_I + \mathbf{u}_R = \mathbf{u}_T$$

$$\sigma_{xiI} + \sigma_{xiR} = \sigma_{xiT} \qquad (i = x, y, z) \tag{103}$$

or, introducing the stress-displacement vector

$$\mathbf{A}_T = \mathbf{A}_R + \mathbf{A}_I \tag{104}$$

Equation (104) can be written as

$$\langle \mathbf{A}_T, \mathbf{A}_T \rangle = \langle \mathbf{A}_R + \mathbf{A}_I, \mathbf{A}_R + \mathbf{A}_I \rangle \tag{105}$$

and using the orthogonality relations we obtain

$$\langle \mathbf{A}_T, \mathbf{A}_T \rangle = \langle \mathbf{A}_I, \mathbf{A}_I \rangle + 2\mathrm{Re}\langle \mathbf{A}_I, \mathbf{A}_R \rangle - \langle \mathbf{A}_R, \mathbf{A}_R \rangle = \langle \mathbf{A}_I, \mathbf{A}_I \rangle - \langle \mathbf{A}_R, \mathbf{A}_R \rangle \tag{106}$$

which is exactly Eq. (102).

The transmitted vector, for the whole set of outgoing modes, can be written as

$$\langle \mathbf{A}_T, \mathbf{A}_T \rangle = \sum_{m'=0}^{\infty} \langle \mathbf{A}_T^{(m')}, \mathbf{A}_T^{(m')} \rangle \tag{107}$$

Defining column vector, $B_{m,m'}$, as the vector whose elements are the transmission coefficients for each single section, defined by relation (84) for the incoming mode m, we can write

$$\langle \mathbf{A}_T, \mathbf{A}_T \rangle = \sum_{m'=0}^{\infty} \sum_{m=0}^{\infty} B_{m,m'}^2 \langle \mathbf{A}_I^{(m)}, \mathbf{A}_I^{(m)} \rangle = \sum_{m'=0}^{\infty} \sum_{m=0}^{\infty} B_{m,m'}^2 \tag{108}$$

Likewise, for the reflected vector, from (106) we obtain

$$\sum_{m'=0}^{\infty} \sum_{m=0}^{\infty} B_{m,m'}^2 + \sum_{m'=0}^{\infty} \sum_{m=0}^{\infty} A_{m,m'}^2 = 1 \tag{109}$$

which corresponds to the condition of unitary scattering matrix as defined by Vaccari et al. (1989). If we consider a single incident mode m of unitary amplitude, expression (109) can be written as:

$$\sum_{m'=0}^{\infty} (\gamma_T^{(m,m')})^2 + \sum_{m'=0}^{\infty} (\gamma_R^{(m,m')})^2 = 1 \tag{110}$$

where γ refers to the coupling energy with transmitted and reflected modes. Equation (110) is the fundamental relation to estimate the approximation introduced by neglecting diffracted body waves.

4.1.2 *Numerical examples*

To test the validity of the analytical algorithm, the transmission and reflection coupling coefficients are computed for a medium defined by the two layered lithospheric models shown in Fig. 9, in welded contact.

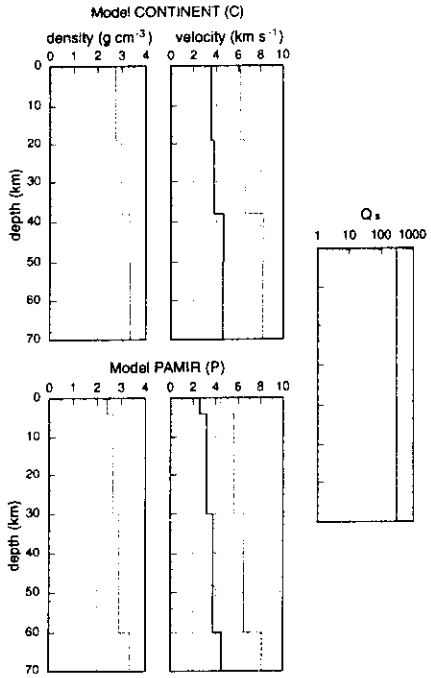

Fig. 9. Elastic and anelastic parameters of model C and model P. Thick lines represent S-wave velocities; Qs is the quality factor common to both structures.

For the sake of simplicity in the following figures the models CONTINENT and PAMIR (Levshin, 1985) will be called model C and model P, while the fundamental mode and the higher modes are indicated, respectively, as F, 1, 2 etc. Therefore, the fundamental mode of model C is named CF, the first higher

mode of model P is named P1, and so on. Each coupling coefficient is associated with a four-character acronym: the first two characters identify the incoming mode, the last two identify the outgoing mode. With this convention, the coupling between the fundamental mode of model C (incident) and the fundamental mode of model P (outgoing) is indicated with CFPF. The corresponding coupling energy is identified by the same acronym, written in lowercase letters.

In Fig. 10 the intracoupling coefficients (85) and (86) are shown for the incident fundamental mode, in both directions (CFPF and PFCF). The two curves corresponding to coefficients (85) overlap almost perfectly. Actually, since the coupling energy for two modes belonging to two different structures is the square of coefficient (85), Fig. 10 demonstrates that in this case the reversibility theorem for the scattering matrix (Vaccari et al., 1989) is satisfied for the whole set of frequencies considered.

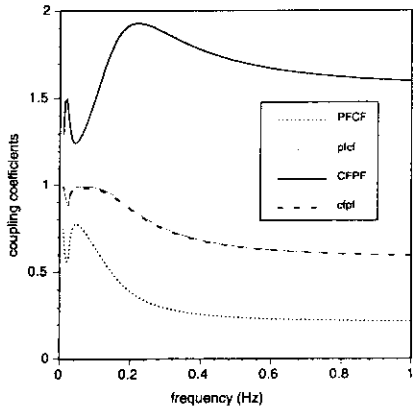

Fig. 10. Coupling coefficients for CFPF and PFCF. The dashed and the thin lines indicate the coefficients defined by Eq. (85).

In Fig. 11 and 12 it is shown how the energy carried by one incident mode of model C is redistributed within several outgoing modes of model P. In Fig. 11 the coupling energies, i.e., the square of coefficient (85), are shown for the incident fundamental mode, while in Fig. 12 we consider the incidence of the first higher mode. In both figures, the curves indicated as SUM T represent the sum of the transmitted energy for five outgoing modes, while the curves marked as SUM include the reflected energy. From Figs. 11 and 12 we can see that the amount of energy neglected corresponds, in the worst case, to 5 and 9% of the incident energy, respectively.

Numerical tests performed with models C and P suggest that, in order to obtain accuracy of three significant digits in the calculated signal (i.e., graphical accuracy), the maximum amount of scattered energy that can be neglected is of the order of 5%. Thus, the results shown in Fig. 12 indicate that when the first higher mode of model C is considered, the couplings with modes with order number higher than five have to be included in the computations if a graphically accurate seismogram is needed. This is an easy task to perform when only two models are considered, due to the high efficiency of the computations. In Sect. 4.3 the results, obtained considering more than 100 incoming modes each coupled with more than 100 outgoing modes, are shown. It has to be mentioned, however, that the resulting intracouplings and intercouplings are strongly dependent on the physical difference of the models adopted and on the frequency that is considered. More similar the two models will be felt by the wavetrain, i.e., for wavelengths greater than the dimension of the heterogeneity, nearer to 1 will be the computed intracoupling energy.

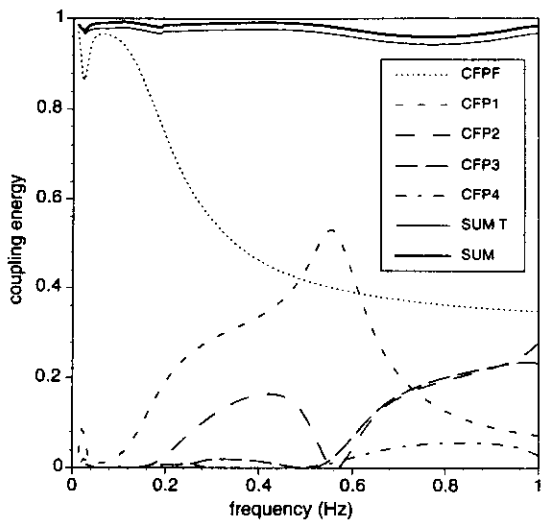

Fig. 11. Transmission of energy from incident fundamental mode of model C to first five modes of model P. SUM T and SUM are the curves describing the outgoing energy, without and with the inclusion of reflected energy.

In Fig. 13 we show the coupling energy for the case of reflection, i.e., the square of the coefficients (Eq. 87), for the first five incident modes of model C. Only the intracoupling coefficients are shown, since for the reflected wavefield the intercouplings are all zero.

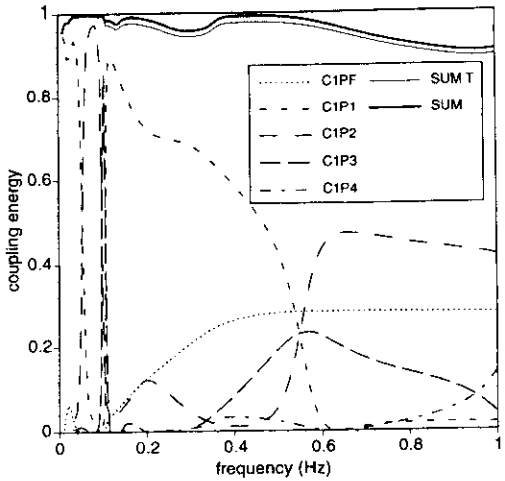

Fig. 12. Transmission of energy from incident first higher mode of model C to first five modes of model P. SUM T and SUM are the curves obtained summing the outgoing energy, without and with the inclusion of reflected energy.

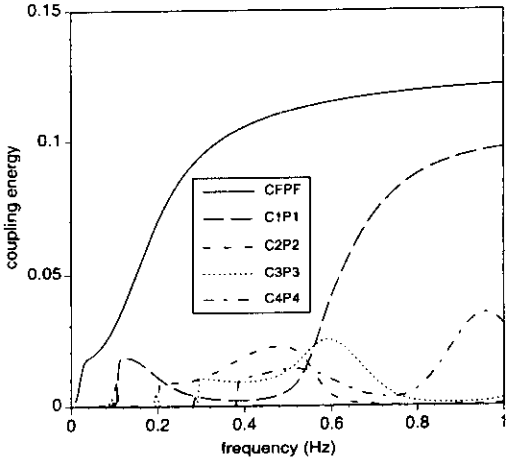

Fig. 13. Reflection of energy for the first five modes incident from model C.

In order to assess the importance of topography in wave propagation we consider the model shown in Fig. 14. The two layered structures differ only for the thickness of the uppermost layer.

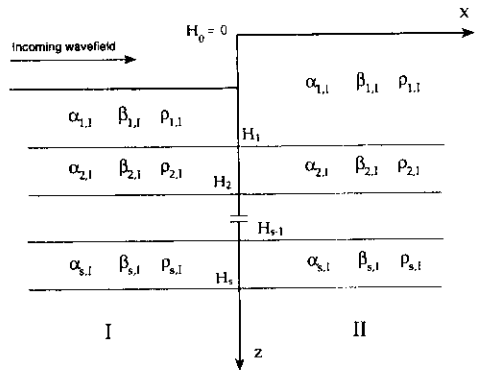

Fig. 14. 2-D model with a topographic step.

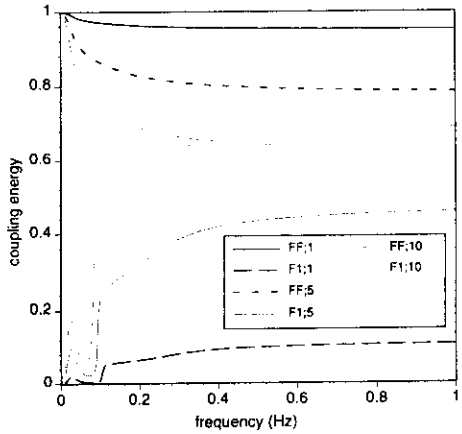

Fig. 15. Coupling energy for incident fundamental mode of medium I and first two outgoing modes of medium II (for the model see Fig. 14). The third parameter in the legend is the thickness of the topographic step, expressed in km.

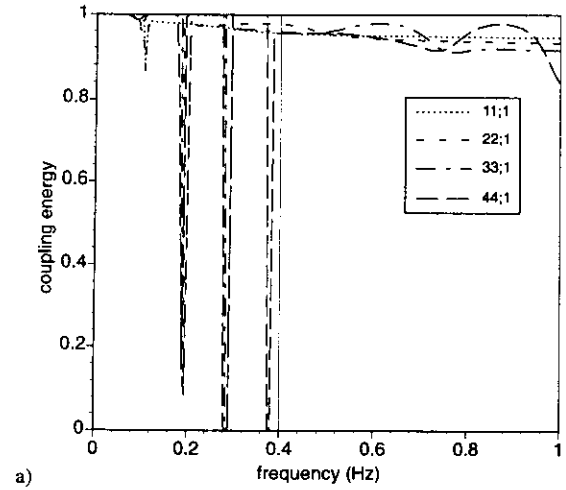

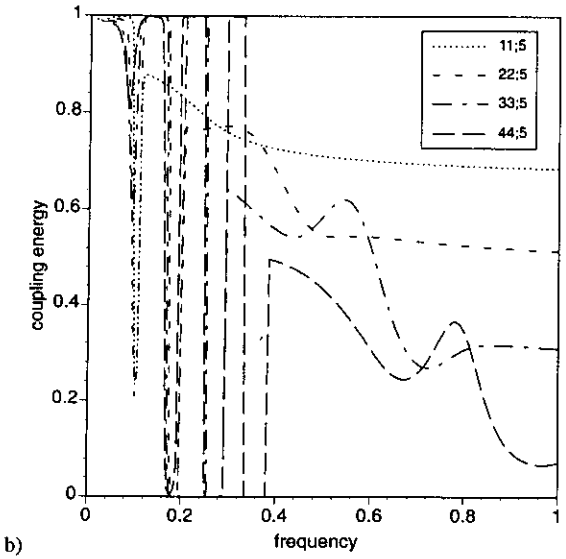

Fig. 16. Transmission of energy for the intracoupling of the first four higher modes: (a) topographic step of 1 km; (b) topographic step of 5 km.

The variability of thickness (H_0 - H_1) of the uppermost layer of medium II defines a variable topographic step that is assumed positive when the thickness is larger in medium II, and negative in the opposite case. In Fig. 15 we show the coupling energy (for three different steps: 1, 5, and 10 km) of the fundamental mode of model C (medium I in Fig. 14) with the fundamental mode (FF;1, FF;5 and FF;10) and with the first higher mode (F1;1, F1;5, and F1;10) of medium II. The higher the step is, the larger the difference between the obtained coupling energy and the values characterizing the absence of the step (1 for intracouplings and 0 for intercouplings).

In Fig. 16 we show the intracoupling energies for the first four higher modes and for topographic steps of 1 or 5 km. The minima in the coupling value become wider and deeper as the height of the topographic step increases.

4.2 Coupling coefficient for Rayleigh modes

For Rayleigh modes the formulation is similar to the one discussed in Sect. 4.1, and the basic definitions (75-80 and 85-88) are identical; the stress-displacement vectors in medium I and medium II and their scalar product can be written as

$$\mathbf{A}_I = (u_{xI}, 0, u_{zI}, \sigma_{xxI}, 0, \sigma_{zxI}) \tag{111}$$

$$\mathbf{A}_{II} = (u_{xII}, 0, u_{zII}, \sigma_{xxII}, 0, \sigma_{zxII}) \tag{112}$$

$$\langle \mathbf{A}_I, \mathbf{A}_{II} \rangle = \frac{1}{2i} \int_0^\infty [u_{xI}\bar{\sigma}_{xxII} + u_{zI}\bar{\sigma}_{zxII} - \bar{u}_{xII}\sigma_{xxI} - \bar{u}_{zII}\sigma_{zxI}]dz \tag{113}$$

The problem of the analytical computation of transmission and reflection coupling coefficients has been solved by Vaccari et al. (1989) who computed the transmission and reflection coefficients at each section of the vertical interface (analogous to (84)) using Nafe (1957) expressions, which are valid only for Poissonian media ($\alpha/\beta = \sqrt{3}$). This assumption in several cases can be highly unrealistic, for instance, in sedimentary basins or geothermal regions (Stümpel et al., 1984; Vaccari and Panza, 1993) where the ratio α/β can vary from 1.5 to approximately 5 (in the sediments) and from 1.7 to 1.9 (in the lower crust and upper mantle of geothermal areas).

The computation of coefficients can be extended to non-poissonian media by modifying in the scalar product (113) the equations of stresses. The component of the stress tensor involved is

$$\sigma_{xx} = \begin{cases} \mu\left(3\dfrac{\partial u_x}{\partial x} + \dfrac{\partial u_z}{\partial z}\right) & \text{Poissonian media} \quad (114a) \\ \lambda\left(\dfrac{\partial u_x}{\partial x} + \dfrac{\partial u_z}{\partial z}\right) + 2\mu\dfrac{\partial u_x}{\partial x} & \text{Non Poissonian media} \quad (114b) \end{cases}$$

Therefore, by substituting (114b) into (113) we can compute the coefficients (85-88) for non-poissonian media (non-poissonian formulation).

4.2.1 Computation of coupling coefficients in non-poissonian media

The transmission coupling coefficients have been computed for a 2-D structural model, M0, made up of the two lithospheric models C and P (see Figs. 8 and 9). Keeping α fixed, the β values have been modified in order to consider the two models M1 and M2, with ratios α/β=1.5 and 2.0 respectively. In the

following, the fundamental mode is indicated by F; the poissonian formulations by *P*, and the non-poissonian formulations by *NP*. In the figures, each coupling coefficient is associated with an acronym of seven or eight characters: the first two refer to the incident mode, the next two to the outgoing mode, the fifth and sixth indicate the model, and the last one (or two) is connected with the formulation employed. As an example, coupling between the fundamental mode of model C (incoming) with the fundamental mode of model P (outgoing) for α/β=2.0, using the poissonian formulation is identified by CFPFM2*P*. The corresponding coupling energy is indicated by the same acronym, written with lowercase letters.

In Fig. 17 we show the intracoupling energies and the intracoupling transmission coefficients, respectively given by Eqs. (85) and (86) when m=m', for the fundamental mode of models M0, M1, M2, computed using formulations *P* and *NP*. The percentage difference in the values of Γ_T obtained with the two formulations is shown in Fig. 18. For model M0, which can be considered quasi-poissonian, the two results are in very good agreement, therefore M0 can be used as a reference model.

If we apply formulation *P* to model M2, both coupling energy and Γ_T are underestimated in the whole frequency range considered, because of the small value of the Lamè parameter λ adopted in the computations. This leads to low values for σ_{xx} and consequently for $\langle \mathbf{A}_T, \mathbf{A}_{II} \rangle$. On the contrary, if we apply formulation *P* to model M1, both coupling energy and Γ_T are overestimated. Furthermore, using the formulation *P* the computed coupling energy becomes larger than 1 for frequencies below 0.3 Hz, violating Vaccari et al.'s (1989)

theorem of energy conservation. Therefore formulation P cannot be used when α/β differs noticeably from $\sqrt{3}$.

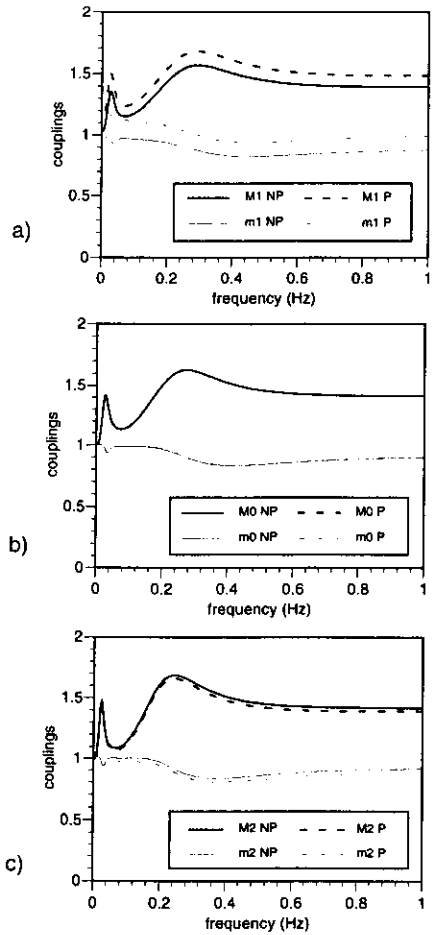

Fig. 17. Transmission coupling coefficients (M) and coupling energies (m) for incident fundamental mode of model C and outgoing fundamental mode of model P. NP and P indicate the non-poissonian and the poissonian formulations, respectively. Structural models: (a) Model 1; (b) Model 0; (c) Model 2.

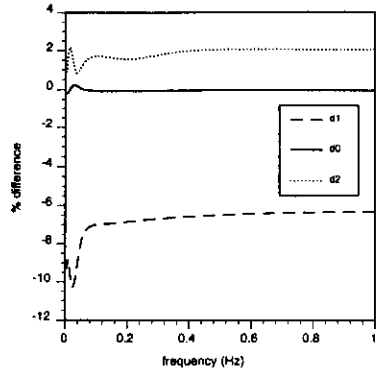

Fig. 18. Percentage difference between the transmission coupling coefficients computed with formulations *NP* and *P* for the fundamental mode. d0, d1, and d2 indicate the percentage differences calculated using the structural models M0, M1 and M2 respectively.

Fig. 19 shows the reflection coupling energy and the reflection coupling coefficient, respectively, given by equations (87) and (88), for the incident fundamental mode of models M1 and M2. The percentage difference of Γ_R for models M0, M1, and M2 is given in Fig. 20.

The higher the mode index is, the stronger the frequency dependence, but we can say that, in the considered frequency range, the percentage difference is generally smaller than the one computed for the fundamental mode. For instance, the maximum percentage difference for the first higher mode is about 2%. When considering high-frequency signals, the error introduced by using formulation P for non-poissonian media can be significant. This error increases when dealing with a sequence of 1-D models in welded contact, since at each vertical interface a value of Γ must be computed and the final result contains their product (see Sect. 4.3).

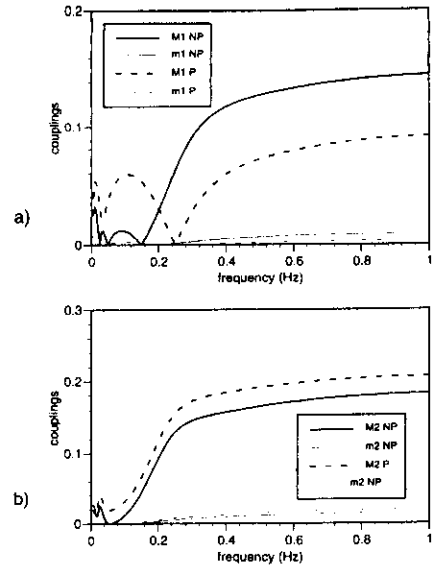

Fig. 19. Reflection coupling coefficients (M) and coupling energies (m) for incident fundamental mode of model C and fundamental mode of model P. NP and P indicate the non-poissonian and the poissonian formulations, respectively. Structural models: (a) Model 1; (b) Model 2.

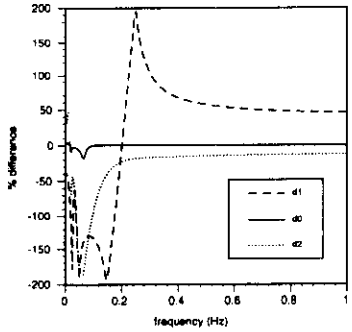

Fig. 20. Percentage difference between the reflection coupling coefficients computed with formulations *NP* and *P* for the fundamental mode. d0, d1, and d2 indicate the percentage differences calculated using the structural models M0, M1, and M2 respectively.

Based on the computation of the coupling coefficients, Gregersen and Vaccari (1993) and Vaccari and Gregersen (1998) have given a simple physical explanation of the propagation and attenuation of Lg waves seen as a superposition of Love and Rayleigh modes (Knopoff et al., 1973; Panza and Calcagnile, 1975).

4.3 Synthetic seismograms in laterally heterogeneous anelastic media

Once the coupling coefficients have been computed for Love and Rayleigh modes, following the algorithm developed in Sects. 4.1 and 4.2, it is possible to compute the synthetic seismograms for a laterally heterogeneous medium like the one shown in Fig. 8.

The expression that describes the displacement due to Love and Rayleigh wave modes propagating in a layered halfspace (28) has been generalized to laterally heterogeneous structures by Levshin (1985), who applied ray theory to surface waves.

Asymptotic expression of the FT of the transverse component of displacement, ${}^{m}U_{y}$, associated with the incoming Love mode m and transmitted into the mode m′, at a distance r from the source can be written as

$$ {}^{m,m'}U_y(r,z,\omega) = \frac{\exp(-i3\pi/4)}{\sqrt{8\pi}} \left[\frac{\chi_L(h_s,\varphi)S(\omega)}{c_L\sqrt{v_{gL}I_{1L}}} \right]_m \left[\frac{\exp\left[-i(k_L d + k'_L d) - \omega(dC_{2L} + d'C'_{2L})\right]}{\sqrt{d/k_L + d'/k'_L}} \gamma_{TL}^{(m,m')} \right]_{mm'} \left[\frac{u_y(z,\omega)}{\sqrt{v_{gL}I_{1L}}} \right]_{m'} \tag{115} $$

where the subscript L refers to Love modes, prime-indexed quantities are related to medium II (the medium with the receiver) and those without index refer to

medium I (the medium with the source), and d and d' indicate the distances travelled in medium I and II, respectively. Expression (115) represents the contribution of one single mode m generated by a point-source placed in medium I, transmitted across the vertical interface and recorded as mode m' in medium II at a distance r=d+d'. If medium I and medium II are equal, (115) reduces exactly to the second expression of (28), valid for a layered halfspace.

If we consider a model composed of N one-dimensional structures in welded contact, separated by vertical interfaces, (115) becomes

$$ {}^{m,m'}U_y(r,z,\omega) = \frac{\exp(-i3\pi/4)}{\sqrt{8\pi}} \left[\frac{\chi_L(h_s,\varphi)S(\omega)}{c_L\sqrt{v_{gL}I_{1L}}} \right]_m \left[\frac{\exp\left[-i(\sum_{j=1}^{N} k_L^j d_j) - \omega(\sum_{j=1}^{N} d_j C_{2j})\right]}{\sqrt{\sum_{j=1}^{N} d_j / k_L^j}} \prod_{j=1}^{N-1} \gamma_{TL}^j \right] \left[\frac{u_y(z,\omega)}{\sqrt{v_{gL}I_{1L}}} \right]_{m'} \tag{116} $$

where mode m is in the first structure and mode m' is in the last one.

The expressions analogous to (115), associated with the FT of the radial (U_x) and vertical (U_z) components are

$$ {}^{m,m'}U_x(r,z,\omega) = \frac{\exp(-3i\pi/4)}{\sqrt{8\pi}} \left[\frac{\chi_R(h_s,\varphi)S(\omega)}{c_R\sqrt{v_{gR}I_{1R}}} \right]_m \left[\frac{\exp\left[-i(k_R d + k'_R d) - \omega(dC_{2R} + d'C'_{2R})\right]}{\sqrt{d/k_R + d'/k'_R}} \gamma_{TR}^{(m,m')} \right]_{mm'} \left[\frac{u_x(z,\omega)}{\sqrt{v_{gR}I_{1R}}} \right]_{m'} \tag{117} $$

$$ {}^{m,m'}U_z(r,z,\omega) = {}^{m,m'}U_x(r,z,\omega)\exp(-i\pi/2)\left(\varepsilon_0|_{m'}\right)^{-1} \tag{118} $$

where subscript R refers to Rayleigh modes. Using expressions (115-118) it is very easy to extend the existing, highly efficient mode summation computer codes (Panza, 1985; Florsch et al., 1991), to laterally heterogeneous media.

In the following figures we show some examples of synthetic seismograms calculated for a laterally heterogeneous structural model that is assembled starting from models C and P, used in Sect. 4.2 (see Fig. 9). The source-receiver distance is 100 km and the vertical interface between the two media is placed right at the middle of the path. An instantaneous point-source is placed at the depth of 10 km, with a scalar seismic moment of 10^{13} Nm. The orientation of the double-couple of forces is defined as follows: strike-receiver angle = 60°, dip = 90°, rake = 180°. The cut-off frequency for the computations is 1 Hz.

In Fig. 21 the seismograms are shown for the three components of displacement, grouped for the four structural models: models C and P and 2-D models CP PC. For each group there are four rows, according to the number of incoming modes: the first row is for the fundamental mode, the second row is for the first 5 incoming modes, the third row is for the first 10 modes, and the fourth row is for 110 incoming modes. For each component of motion the seismograms are normalized to the maximum amplitude associated with the signal computed for 2-D model CP summing 110 modes.

Arrival times of the wavetrains propagating in the laterally heterogeneous structure are a kind of average of the arrival times characteristic of the two 1-D models. Peak amplitude of the signals computed for model CP is always larger

than the peak value obtained in the laterally homogeneous media. Looking at the waveforms obtained for the laterally heterogeneous anelastic models, CP and PC, it appears that the transverse component is controlled more by the model where the source is placed. For radial and vertical components, the model where the receiver is placed seems to have greater importance. A possible interpretation is that the ellipticity factor, ε_0, could be more relevant than the radiation pattern, χ_R, for P-SV motion (see expressions (116-118)). In the general case the relative position of the source and of the receiver with respect to the vertical interface can play a more fundamental role.

In Fig. 21 the difference between the signal shown in the last row of the CP-radial component of motion (and, to a minor extent, of the CP-vertical component) and the corresponding signals, obtained summing modes with lower order numbers, is bigger than in the other cases. This can be explained by the fact that, in the P-SV motion problem for the CP case, the intercoupling energy for the higher modes becomes significant, making the amplitude of the early phases, with higher frequency content, comparable to that of the later dominant arrivals associated with lower order modes (see Fig. 22).

The described methodology can be applied to improvement of the existing laterally variable models at a regional scale (Du et al., 1998), as well as to study of the site response of local heterogeneous models (see Sect. 5.2.2).

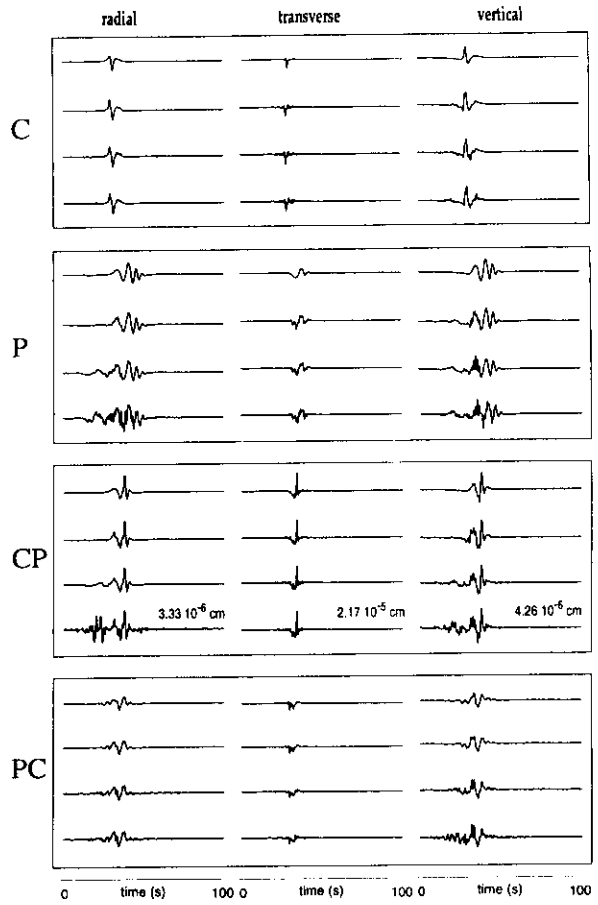

Fig. 21. Synthetic seismograms for the three components of displacement, grouped for the four structural models: models C and P and 2-D models CP and PC. For each group four rows are shown, according to the number of incoming modes: the first row is for the fundamental mode, the second row is for the first 5 incoming modes, the third row is for the first 10 modes and the fourth row is for 110 incoming modes. For each component of motion the seismograms are normalized to the maximum amplitude associated with the signal computed for 2-D model CP summing 110 modes.

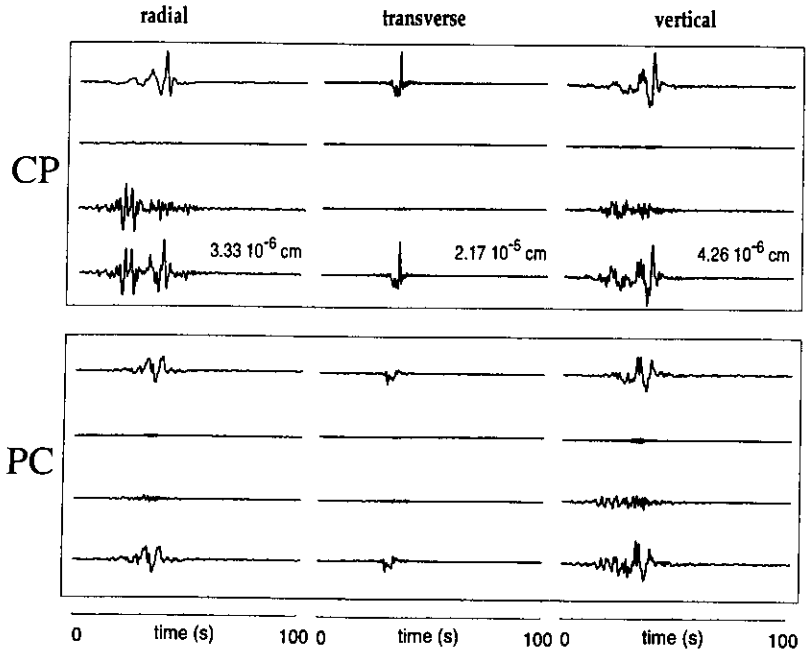

Fig. 22. Synthetic seismograms for the three components of displacement, grouped for the 2-D structural models CP and PC. For each group four rows are shown, according to the number of incoming modes and the considered couplings: first and last rows are for the first 10 incoming modes and 110 incoming modes, respectively (same as Fig. 21); second and third rows are for 10-110 incoming modes, excluding and including cross-couplings, respectively. For each component of motion the seismograms are normalized to the maximum amplitude associated with the signal computed for the 2-D model CP summing 110 modes.

5. Deterministic seismic hazard assessment: from seismic zonation to site response estimation

Strong earthquakes such as the 1985 Michoacan earthquake and the 1995 Kobe have acted as catalysts for the use of zoning in seismic risk management. Politicians and administrators are more and more interested in the rapid reconstruction according to criteria which reduce the probability of a repetition of disasters. In an anthropc area it is now technically possible to identify zones in which the heaviest damage can be predicted. A first-order zoning can be carried out at regional scale, based on the knowledge of the average properties of seismic sources and on structural models. Microzonations are possible as well, provided that detailed information about the source, path, and local site conditions are available.

A drastic change is required in the orientation of zoning that must be a predisaster activity performed to mitigate the effects of the next earthquake, using all available technologies. The events in Los Angeles (1994) and Kobe (1995) clearly show that we must be able to take preventive steps, extending, in a scientifically acceptable way, the obtained results to areas in which no direct experience has yet been gained. Seismic zoning can use scientific data banks, integrated in an expert system, by means of which it is possible not only to identify the safest and most suitable areas for urban development, but also to define the seismic input that is going to affect a given building. Examples of this capability, closely linked to the ability to calculate realistic synthetic seismograms, are given in Sects. 5.1 and 5.2.

5.1 Deterministic seismic zoning: regional scale

The procedure for deterministic seismic zoning developed by Costa et al. (1992, 1993) and subsequently widely applied (Orozova-Stanishkova et al., 1996; Alvarez et al., 1999; Aoudia et al., 2000; Bus et al., 2000; Markusic et al., 2000; Radulian et al., 2000; Zivcic et al., 2000) represents one of the new and most advanced approaches. It can be used also as a starting point for the development of an integrated approach that will combine the advantages of the probabilistic and deterministic methods, thus minimizing their respective drawbacks. This approach addresses some issues largely neglected in probabilistic hazard analysis, namely how crustal properties affect attenuation: ground motion parameters are not derived from overly simplified attenuation functions, but rather from synthetic time histories.

Starting from the available information on the Earth's structure, seismic sources, and the level of seismicity of the investigated area, it is possible to estimate maximum ground acceleration, velocity, and displacement (AMAX, VMAX, and DMAX, respectively) or any other parameter relevant to seismic engineering, which can be extracted from the computed theoretical signals. This procedure allows us to obtain a realistic estimate of the seismic hazard in those areas for which scarce (or no) historical or instrumental information is available and to perform the relevant parametric analyses.

Synthetic seismograms can be constructed to model ground motion at sites of interest, using knowledge of the physical process of earthquake generation and wave propagation in realistic media. The signals are efficiently generated by the modal summation technique (see Sect. 2), so it becomes possible to perform

detailed parametric analyses at reasonable costs. For instance, different source and structural models can be taken into account to create a wide range of possible scenarios from which to extract essential information for decision making.

In first-order zoning, average structural models are defined, representing the lithospheric properties at a regional scale. Synthetic seismograms are computed, taking into account the effects of lateral heterogeneities in a rough way: if the source-receiver path crosses one or more boundaries between adjacent structural models, the signal is computed assuming the model of the receiver as representative of the whole path. This is justified by the results shown in Fig. 21, where the signals obtained for the laterally heterogeneous medium look more similar to the signals computed in the receiver structural model than to those computed using the structural model containing the source.

The flowchart of the procedure is shown in Fig. 23. The first problem to tackle in the definition of seismic sources is the handling of seismicity data. Basically, what is needed is an evenly spaced distribution of the maximum magnitude over the territory, but the data available from earthquake catalogues are widely scattered. Furthermore, earthquake catalogues are both incomplete and affected by errors, so a smoothed distribution is preferable (Panza et al., 1990).

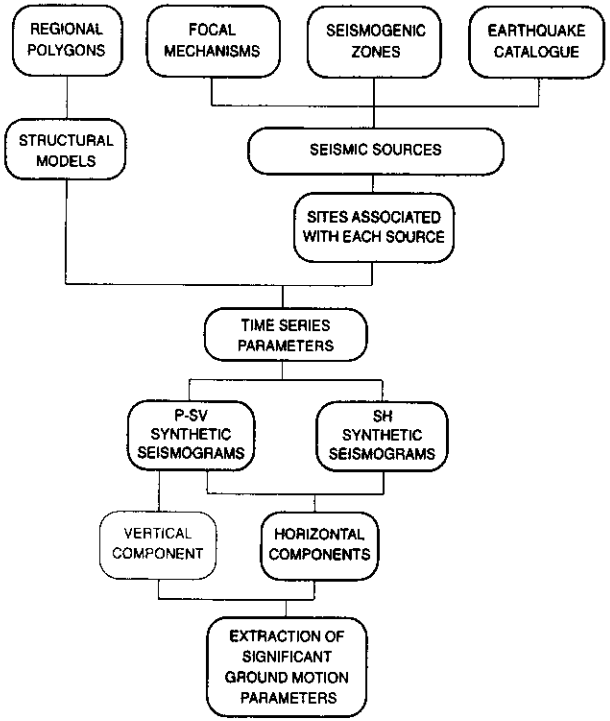

Fig. 23. Flow-chart of the deterministic procedure for seismic hazard assessment at regional scale. The vertical component is routinely not used.

The smoothing procedure is shown in Fig. 24. The punctual distribution of epicenters given in Fig. 24a is discretized into cells (Fig. 24b) and the maximum magnitude of the events pertinent to each cell is retained. In the case where the earthquake catalogue contains different estimates of magnitude (e.g., magnitude computed from body waves, from surface waves, or from macroseismic intensity), the maximum between them is considered. It is then convenient to represent the data graphically, and symbols are associated with magnitude

ranges (Fig. 24c). In most cases, the smoothing obtained by considering just the discretized cells is not enough. A centered smoothing window is then considered, so that earthquake magnitudes are analyzed not only in the central cell but also in the neighboring ones. The idea of a constant magnitude within each seismogenic area (choosing the maximum available value) has been shown to be a poor choice, since for the larger seismogenic areas it leads to an overestimation of the seismicity. Three possible smoothing windows are shown in Fig. 24d.

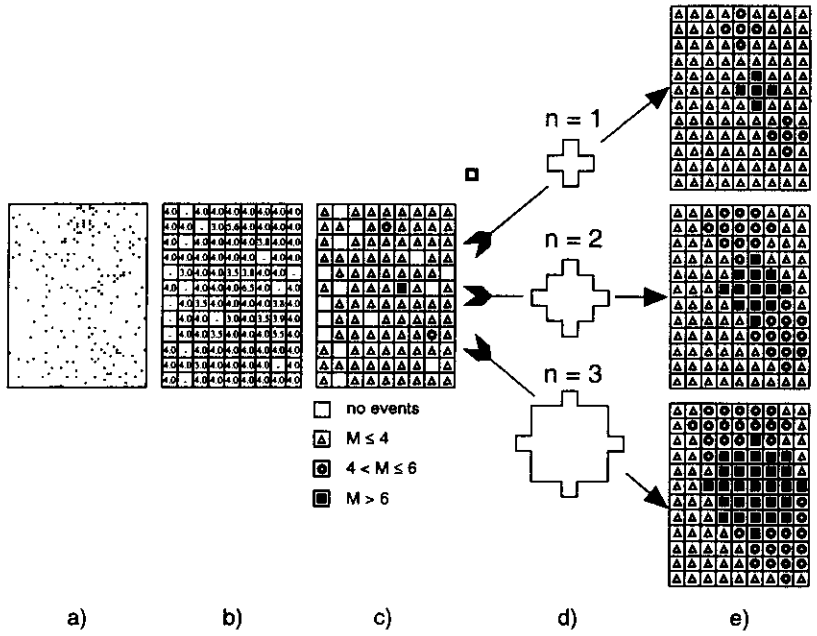

Fig. 24. Discretization and smoothing of seismicity. (a) Distribution of epicenters; (b) definition of cells and choice of the maximum magnitude; (c) graphic representation; (d) smoothing windows of radius n=1, n=2, n=3; (e) smoothed distribution of magnitude.

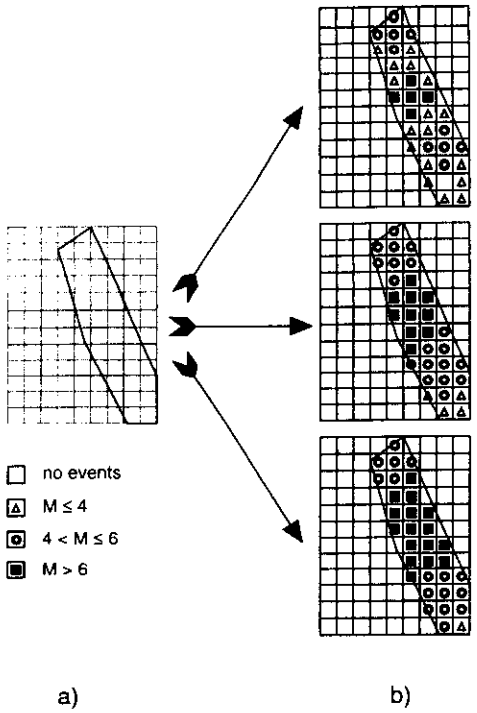

Fig. 25. (a) Seismogenic zone and (b) its intersection with the smoothed data shown in Fig. 24(e).

Their radius is expressed in terms of number of cells n. In the example, the values n=1, n=2 and n=3 are considered. By applying those windows to the distribution in Fig. 24c, the results of Fig. 24e are obtained. At first glance, it appears that distribution of the maximum magnitude given by the window with n=3 is quite exaggerated with respect to the starting data of Fig. 24c. Its intersection with a hypothetic seismogenic area (shown in Fig. 25a), gives quite a reasonable distribution (Fig. 25b), which allows us to account for errors in the location of the source and for its extension in space. The smoothing

corresponding to radius n=3 (smoothing 1) is chosen to produce deterministic maps of hazard, while the smoothing n=1, applied only to the strongest shocks (smoothing 2), is employed to derive empirical relations between ground motion parameters and observed intensities. In Figs. 24 and 25, symbols are used only to improve readability. In the actual smoothing procedure magnitudes are not divided into classes.

For definition of the seismic sources that generate the synthetic seismograms, only the cells located within a seismogenic area are retained. The map shown in Fig. 26 is the result of the application of smoothing 1 to the NT4.1 earthquake catalogue (Camassi and Stucchi, 1996).

The focal mechanisms of the seismic source placed at the center of each cell are defined as the *best* double-couple, corresponding to the arithmetic average of the tensor elements of the available mechanisms in the relevant seismogenic zone. This simple procedure appears to be reasonable when the mechanisms on average are similar, and this condition should always be checked for each seismogenic area.

Once the structures and the sources have been defined, sites are considered on a grid (0.2° X 0.2°) that covers the whole territory. The synthetic signals are computed for an upper frequency content of 1 Hz, and the scaled point-source approximation (Gusev, 1983) is still acceptable. This is fully justified by practical considerations, as several-story buildings have a peak response in the frequency range below 1 Hz (Manos and Demosthenous, 1992), and by the fact that modern seismic design approaches and technologies, such as seismic isolation, tend to lower the free oscillation frequencies of buildings. As a rule of thumb (in Italian legislation) the resonance period (in seconds) of a building can be expressed as

$0.1H/B^{0.5}$, where H is the height and B is the maximum lateral extension, in meters. When shorter periods are considered, it is no longer possible to neglect the finite dimensions of the faults and the rupturing process at the source.

To reduce the number of computed seismograms, the source-receiver distance is kept below an upper threshold, which is taken to be a function of the magnitude associated with the source. The maximum source-receiver distance has been set equal to 25, 50, and 90 km, respectively, for $M < 6$, $6 \leq M < 7$ and $M \geq 7$. All seismograms are computed for a hypocentral depth which is a function of magnitude (10 km for $M < 7$, 15 km for $M \geq 7$), but it is also possible to assign to each source an average depth determined from analysis of the available catalogues. Keeping the hypocentral depth fixed (for classes of magnitude) and shallow is important due to the large errors generally affecting hypocentral depth reported in the earthquake catalogues and due to the fact that strong ground motion is mainly controlled by shallow sources (Vaccari et al., 1990), with the spectacular exception of the Vrancea region (Radulian et al., 2000) seen in Figs. 32-34.

Synthetic seismograms for P-SV-waves (radial and vertical components) and SH-waves (transverse component) are originally computed for a seismic moment of 10^{-7} Nm. The amplitudes are then properly scaled according to the smoothed magnitude associated with the cell of the source. For the moment-magnitude relation, we have chosen that given by Kanamori (1977). The finiteness of the source is accounted for by scaling the spectrum using the spectral scaling law proposed by Gusev (1983) as reported in Aki (1987). At each site, the horizontal components are first rotated to a reference system common to

the whole territory (North-South and East-West directions) and then the vector sum is computed.

Among the parameters representative of strong ground motion we have focused our attention on maximum ground acceleration, velocity, and displacement (AMAX, VMAX, and DMAX). In computing the complete time series we are not limited to this choice, and it is possible to consider integral quantities that can be of interest in earthquake engineering or engineering seismology (Uang and Bertero, 1990; Decanini and Mollaioli, 1998).

The Fourier spectra of displacements and velocities show that an upper frequency limit of 1 Hz is sufficient to take into account the dominant part of seismic waves, while this is definitely not true for accelerations (Panza et al., 1999a). On the other hand, the required knowledge about seismic sources and lateral heterogeneities, which might justify the choice of a higher frequency limit in the computations, is not usually available at the scale of the areas generally considered in the zoning.

For accelerations, deterministic results may be extended to frequencies higher than 1 Hz by using design response spectra, for instance, Eurocode 8 (EC8, 1993), which define the normalized elastic acceleration response spectrum of the ground motion, for 5% critical damping. In general, this operation should be made taking into account the soil type. If the regional structural models used are all of type A, as defined in EC8, we can immediately determine the Design Ground Acceleration (DGA) (Panza et al., 1996).

5.1.1 Seismic zoning of Italy

The NT 4.1 file prepared by Gruppo Nazionale per la Difesa dai Terremoti (GNDT) (Camassi and Stucchi, 1996) is used for the definition of seismicity. The smoothed magnitude distribution for cells belonging to the seismogenic zones defined by GNDT (Corsanego et al., 1997) is given in Fig. 26. The focal mechanisms associated with each seismogenic zone are obtained from a collection of data gathered by Suhadolc (1990) and Suhadolc et al. (1992). DGA, VMAX, and DMAX maps are shown in Figs. 27, 28 and 29, respectively. In Figs. 30 and Figure 31 the periods associated with VMAX and DMAX are shown. In some regions such as Central Italy around latitude 42°N, long periods in the range between 20 and 30 s dominate.

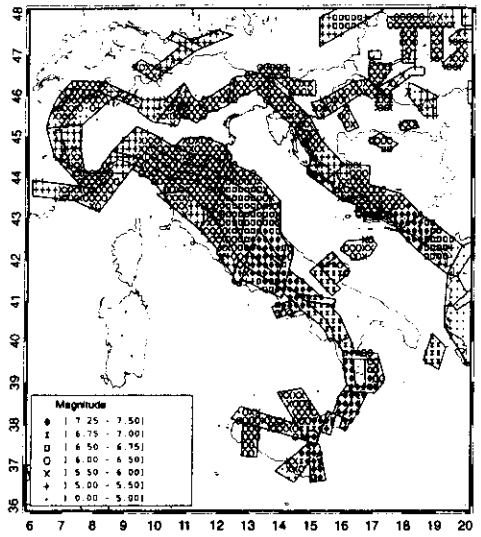

Fig. 26. Smoothed magnitude distribution for the cells belonging to the seismogenic zones defined by GNDT (Corsanego et al., 1997) and updated by A.A.V.V. (2000).

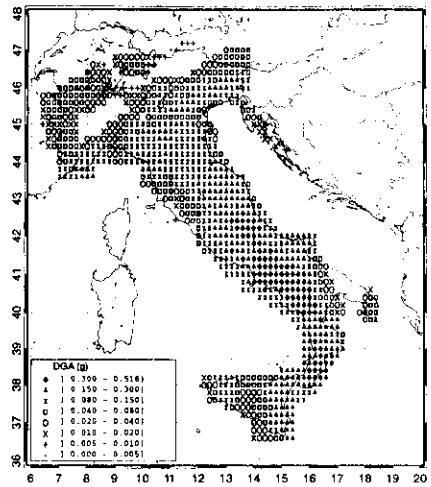

Fig. 27. Distribution of DGA, obtained as a result of deterministic zonation extended to high frequencies using the design spectra of EC8 for soil A. Similar maps can be readily constructed using other design spectra. Units: 1g = 980 cm/s^2.

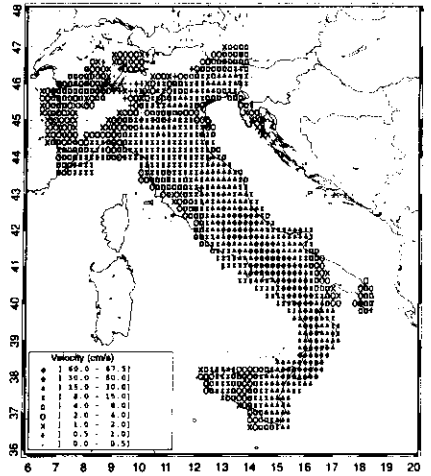

Fig. 28. Horizontal VMAX distribution, obtained as a result of deterministic zonation.

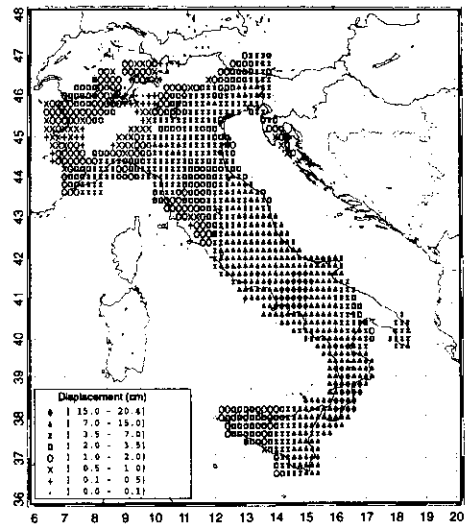

Fig. 29. Horizontal DMAX distribution, obtained as a result of deterministic zonation.

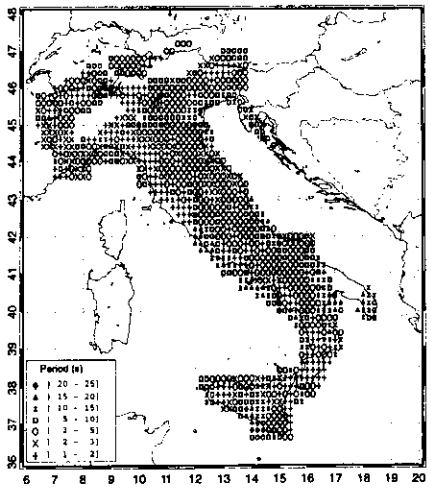

Fig. 30. Period in seconds of the maximum of VMAX at each site.

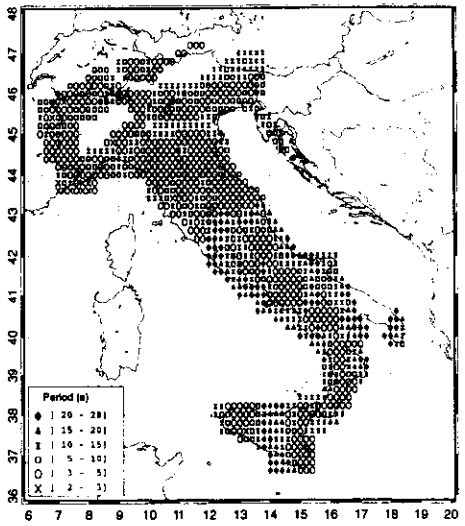

Fig. 31. Period in seconds of the maximum of DMAX at each site.

They are related to signals generated by strong earthquakes occurring at large distances from the site (about 90 km), while the magnitude of the closer events, which are responsible for the higher frequencies (between 2 and 5 s in our computations), is not big enough to let these frequencies dominate the ground motion scenario.

Results of the deterministic procedure are particularly suitable for civil engineers as seismic input for the design of special buildings. In fact, the relevance of the displacements at periods on the order of 10 s or so is a key issue for seismic isolation and in general for lifelines with large linear dimensions, such as bridges and pipelines, where differential motion plays a relevant role in their stability (Monti et al., 1996).

Deterministic modelling can be used to derive correlatios between the maximum-felt macroseismic intensity, I, and DMAX, VMAX, and DGA. This possibility is particularly relevant for countries with a long seismological history since it facilitates the engineering use of historical events that are quantified only in terms of macroseismic intensity. Smoothing 2 is applied to the procedure described in Figs. 24 and 25, assuming n=1 for events with magnitude larger than 6.75 (Panza et al., 1997, 1999a). In this way only the source dimension is accounted for, and the mislocation errors that possibly affect the historical catalogues are neglected, since the same error is present in the observations as well. Using (1) the map of maximum macroseismic intensity felt in Italy, made by Istituto Nazionale di Geofisica (ING) (Boschi et al., 1995), and (2) the set of maximum intensity felt in every municipal land, compiled jointly by ING, SSN and GNDT (ISG) (Molin et al.,1996), Panza et al. (1997, 1999a) obtained two sets of regressions from which the intervals shown in Tables 1 and 2 can be defined.

Table 1. Conversion table between macroseismic intensity and ground motion parameters, DMAX, VMAX, DGA, using ING intensity data.

Intensity	DMAX (cm)	VMAX (cm/s)	DGA (g)
V	0.1 – 0.5	0.5 – 1.0	0.005 – 0.01
VI	0.5 - 1.0	1.0 –2.0	0.01 – 0.02
VII	1.0 – 2.0	2.0 – 4.0	0.02 – 0.04
VIII	2.0 – 3.5	4.0 – 8.0	0.04 – 0.08
IX	3.5 – 7.0	8.0 – 15.0	0.08 – 0.15
X	7.0 – 15.0	15.0 – 30.0	0.15 – 0.30
XI	15.0 – 30.0	30.0 – 60.0	0.30 – 0.60

Table 2. Conversion table between macroseismic intensity and ground motion parameters, DMAX, VMAX, DGA, using ISG intensity data.

Intensity	DMAX (cm)	VMAX (cm/s)	DGA (g)
VI	1.0 – 1.5	1.0 –2.0	0.01 – 0.025
VII	1.5 – 3.0	2.0 – 5.0	0.025 – 0.05
VIII	3.0 – 6.0	5.0 – 11.0	0.05 – 0.1
IX	6.0-13.0	11.0 – 25.0	0.1 – 0.2
X	13.0 – 26.0	25.0 – 56.0	0.2 – 0.4

5.1.2 Zoning of the Circum Pannonian region

The results summarized in this section have been obtained using the framework of the international project EC-COPERNICUS "Quantitative seismic zoning of the Circum Pannonian region (QSEZ-CIPAR)" and the NATO Linkage Grant "Earthquake hazard associated to the Vrancea region seismicity" and are described in the special issue of Pure and Applied Geophysics: Seismic Hazard of the Circum Pannonian Region (A.A.V.V., 2000). Details about the definition of the structural models and source characteristics are given in Orozova-Stanishkova et al. (1996), Radulian et al. (2000), Bus et al. (2000), Markusic et al. (2000), Zivcic et al. (2000).

The main effort has been to harmonize Eastern and Western Europe in terms of seismic safety compliance. Standard deterministic procedure described in Sect. 5.1 has been applied, with the exception of the strong events occurring at intermediate-depth in the Vrancea (Romania) region. To handle this case, response spectra especially determined for Romanian intermediate-depth earthquakes (Lungu et al., 1996) have been considered instead of EC8, and the

computations have been performed over Romanian, North-Eastern Croatian, and Hungarian territory, and elsewhere within a circle of 350 km radius, centered on the Vrancea epicenter cell. The hypocentral depth of the intermediate-depth events is 90 km for magnitudes less than 7.4, and 150 km for the larger ones. In Figs. 32, 33, and 34 we show maps of peak values of horizontal motion (DMAX, VMAX, and DGA) for the European countries that have been involved in this major effort for mitigating seismic hazard.

Peak values for DGA, VMAX, and DMAX, and pertinent periods associated with displacements, T(D), and velocities, T(V), obtained with the deterministic approach at the sites where nuclear power plants are located (Fig. 35) are summarized in Table 3. The values obtained at Cernavoda, Kozloduy, and Paks are due to the intermediate-depth Vrancea events.

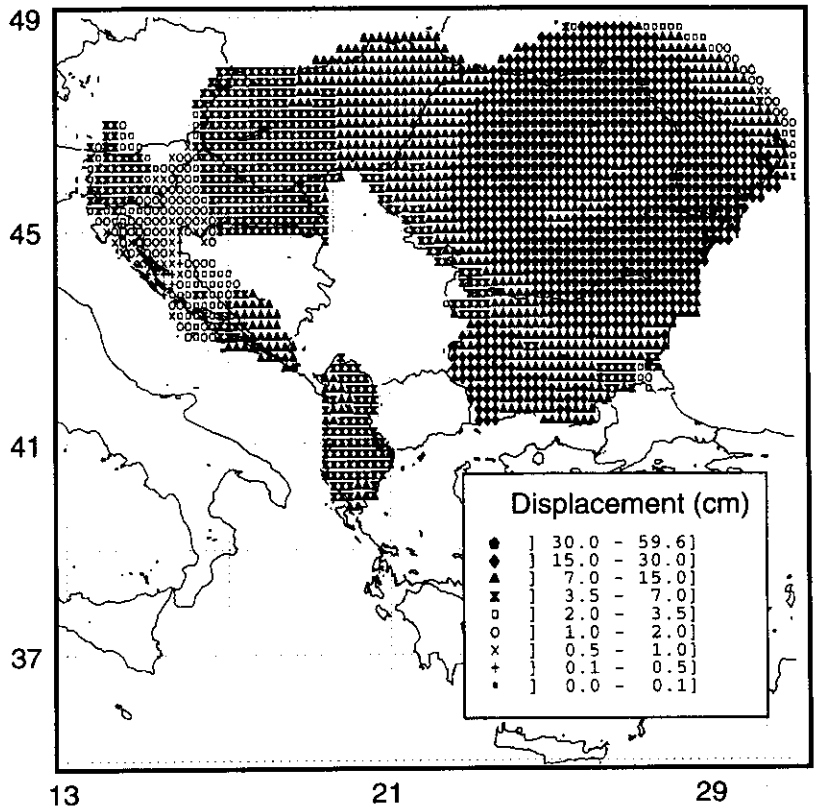

Fig. 32. Maximum displacements. Shallow seismicity has been considered, limiting computations to epicentral distances shorter than 90 km. In the case of Vrancea intermediate-depth events, computations have been performed over the Romanian, North-Eastern Croatian, and Hungarian territory and elsewhere within a circle of 350 km radius, centered on Vrancea epicenter cell. The hypocentral depth is 90 km for magnitude less than 7.4, and 150 km for larger events. The thick gray outline defines the polygons where computations have been performed.

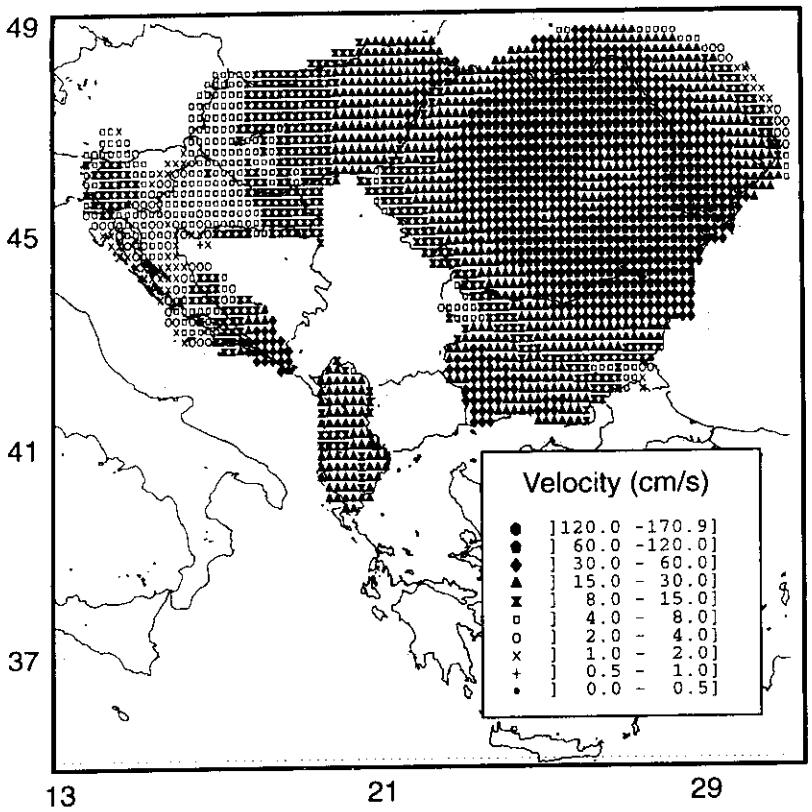

Fig. 33. Same as in Fig. 32 but for maximum velocities.

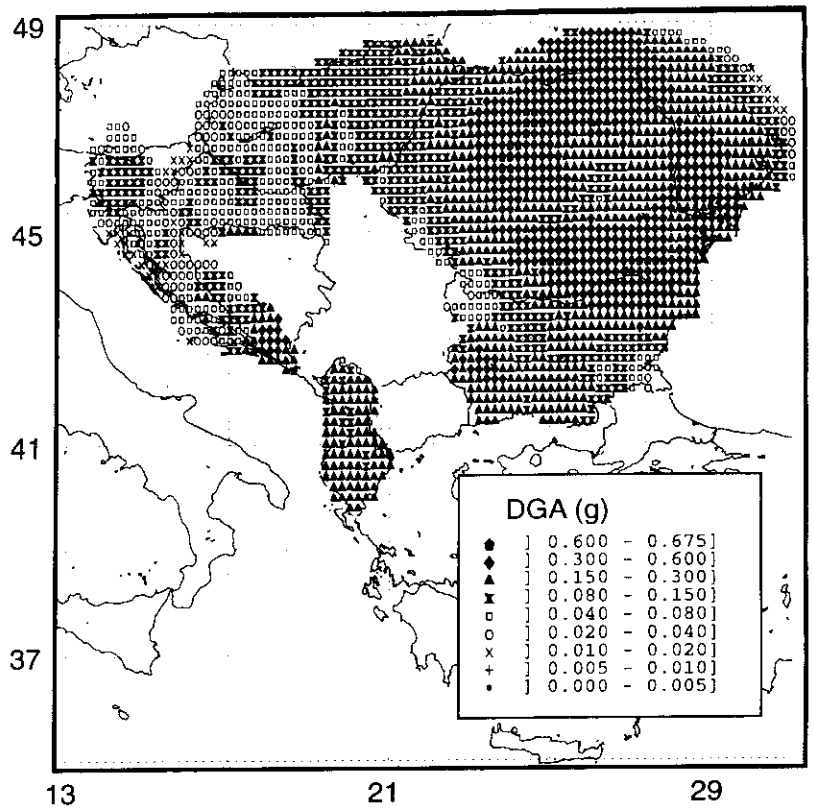

Fig. 34. DGA based on the European Building Code EC8 for shallow events and on response spectra especially determined for the Romanian intermediate-depth earthquakes in the case of Vrancea intermediate-depth events.

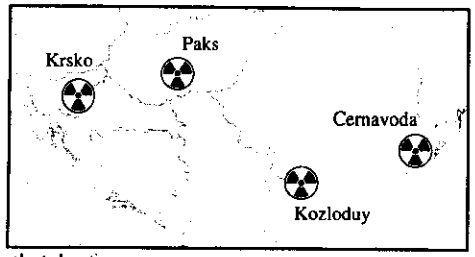

Fig. 35. Nuclear power plants location.

Table 3. Modelled ground shaking for the nuclear power plants of Fig. 35.

Site Name	DMAX cm	T(DMAX) s	VMAX cm/s	T(VMAX) s	DGA g
Cernavoda	35	11.0	91	1.5	0.32
Kozloduy	9	18.0	15	4.0	0.10
Krsko	1	4.5	3	4.5	0.04
Paks	6	3.5	8	3.5	0.07

5.1.3 Validation of the synthetic models against independent observations

Quantitative validation of the deterministic results has been made using the observed accelerograms recorded during the Irpinia earthquake on 23 November 1980 (M=6.9, Camassi and Stucchi, 1996) and the Friuli earthquake on 6 May 1976 (M=6.5, Camassi and Stucchi, 1996). The source rupturing process of the Irpinia event is very complex (Bernard and Zollo, 1989) and the dimension of the source has been estimated to be on the order of several tens of kilometers. Nevertheless, it seems that the signal recorded at the station of Sturno is mostly due to a single subevent that occurred rather close to the station itself, while the energy contributions coming from other parts of the source seem less important (Vaccari et al., 1990). With the cut-off frequency at 1 Hz, the horizontal accelerations recorded at Sturno have been lowpass filtered to be compared with

the computed signals for the Irpinia region. The example shown in Fig. 36a refers to the NS component, but the same considerations can be applied to the EW component of motion. The early phases and the AMAX of the recorded signal (upper trace) and the synthetic one computed in the point-source approximation (middle trace) are in good agreement. The later part of the observed recording is more complicated and this is mostly related to the complexity of the source, which is deliberately neglected in the computation of the synthetic signal, to be used in the zoning. The lower trace is shown as an example of modelling of the source complexity. It is the result of a superposition of four subevents, each one modelled with the middle trace properly weighted and shifted in time according to the model by Vaccari et al. (1990).

The same approach has been used for comparison of the NS component recorded at Tolmezzo during the Friuli (1976) earthquake (Fig. 36b, upper trace) and two synthetic signals obtained for that area (middle and lower traces). In the case of the Tolmezzo record of the Friuli event, the point-source approximation seems to be satisfactory even for an event with Ms=6.1. Quite good agreement has been obtained using a similar procedure by Moldoveanu and Panza (1999) for Vrancea events. The zonation map of Italy proved the prediction capabilities of peak values in the Umbria-Marche region (Central Italy), where a long sequence of events occurred, starting in September 26, 1997, with the largest shock being of magnitude 6.1 (NEIC). The peak of horizontal acceleration, lowpass-filtered at 1Hz, predicted with the modelling, is 70 cm/s^2 and the observed one is 44 cm/s^2. The agreement is improved for peak velocities: about 20 cm/s both for synthetic and for observed time series (obtained by integration of the recorded acceleration).

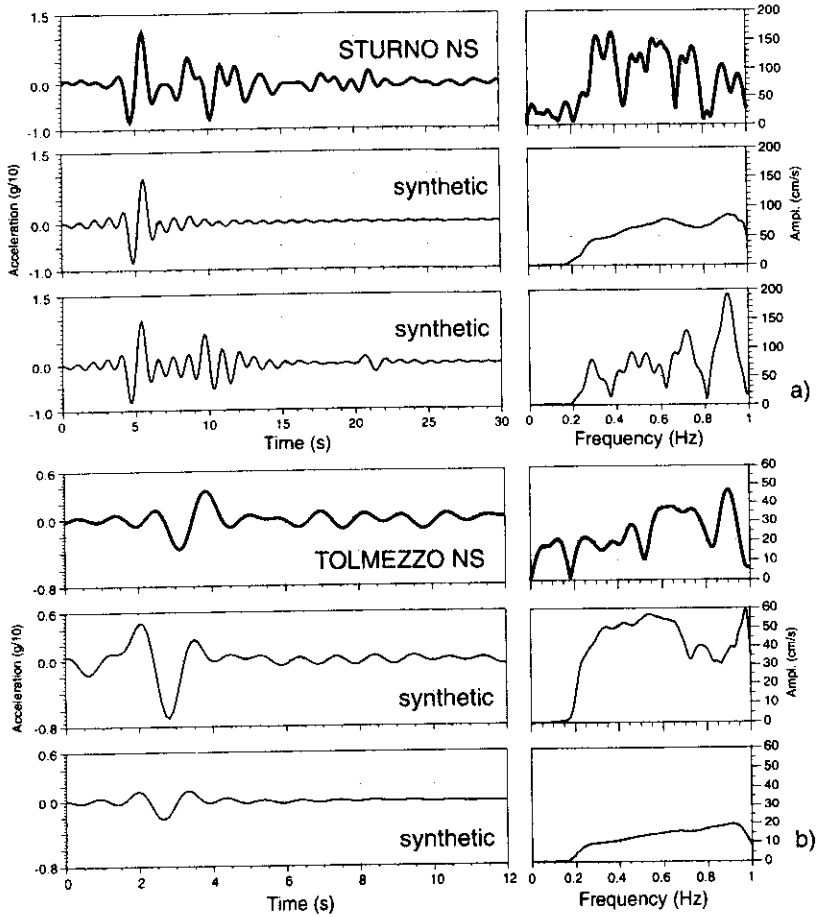

Fig. 36. (a) Comparison of NS component of acceleration recorded at Sturno, filtered with a cut-off frequency of 1Hz (top trace), and two synthetic seismograms computed at the closest grid point, in the point-source approximation (middle trace), and for a complex source (bottom trace), with spectral amplitude. (b) Comparison of NS component of acceleration recorded at Tolmezzo, filtered with a cut-off frequency of 1Hz (top trace) and two synthetic signals computed at the grid point closest to the station (middle and bottom trace), with spectral amplitude.

5.2 *Deterministic seismic zoning: sub-regional and urban scale*

One of the basic problems associated with the study of seismic hazard is determining the seismic ground motion, at a given site, from an earthquake with a given magnitude or moment and epicentral distance from the site. The ideal solution for such a problem could be to use a database of recorded strong motions and to group those accelerograms that have similar source, path and site effects. In practice however, such a database is not available. Actually, the number of recorded signals is relatively low and the installation of local arrays in each zone with a high level of seismicity is too expensive an operation, requiring a long time interval to gather statistically significant data sets. An alternative method is based on computer codes, developed from knowledge of the seismic source process and the propagation of seismic waves, that can simulate the ground motion associated with given earthquake scenario. Synthetic signals can then be produced immediately at a very low cost/benefit ratio, to be used as seismic input in subsequent engineering analysis.

Once the gross features of the seismic hazard are defined, and the parametric analyses have been performed, a more detailed modelling of the ground motion can be carried out for sites of specific interest. Such a detailed analysis should take into account the source characteristics, the path and the local geological and geotechnical conditions. This deterministic modelling goes well beyond the conventional deterministic approach taken in hazard analyses - in which only a simple wave attenuation relation is invoked - in that it includes full waveform modelling.

It is not possible to refine the results obtained with first-order zoning by simply assuming a higher cutoff frequency (> 1 Hz) in the computation of synthetic seismograms. A more detailed zoning requires better knowledge of the seismogenic process in the region. Furthermore, to model wave propagation in greater detail the structural model used in the computation of synthetic seismograms must take into account lateral heterogeneities. Detailed numerical simulations play an important role in the estimation of ground motion in regions of complex geology. They can provide synthetic signals for areas where recordings are absent. Numerical simulations are, therefore, useful for the design of earthquake-resistant structures, in particular when seismic isolation techniques are applied. In fact the number of available strong motion recordings containing reliable information at periods of a few seconds is very small and will not increase very rapidly, since strong earthquakes in densely instrumented areas are rare events.

5.2.1 Local site response

One of the most important factors influencing spatial variability of ground motion is the site response. The local amplification, or deamplification, effects can dominate the ground shaking response whenever lateral heterogeneities, such as surface topographical features or soft-sedimentary basins, are present in the vicinity of a site.

Topographical site effects have not been studied extensively, but their importance is confirmed both by instrumental evidence (Géli et al., 1988; Bard, 1997) and by numerical simulations (Pedersen et al., 1988; Chávez-García et al., 1996). Although there is no general quantitative agreement between theory and

observation, a valid qualitative conclusion is that the seismic ground motion is amplified on mountain tops, i.e., over *convex* topographies, with respect to the valley bottoms (Bard, 1997). Numerical simulations have shown (Géli et al., 1988) that the amplification patterns are strongly dependent on the incidence angle, the nature of the incoming wavefield, and the sharpness of the topography. Focusing the diffracted seismic energy may explain the fact that the greater amplifications occur at those wavelengths that are comparable with the horizontal dimension of the topographical feature (Bard, 1997).

A simpler physical explanation for local amplification of ground motion, due to soft surface layering, is the trapping of seismic energy, due to impedance contrast between the soft surface soils and the underlying bedrock. Moreover, the relatively simple onset of vertical resonances can be transformed into a complex pattern of resonances, strongly dependent on the characteristics of the subsurface topography of the sedimentary deposits.

Macroseismic observations made of the destructive events of the twentieth century have clearly shown the strong influence of near-surface geological and topographical conditions on damage distribution. Most anthropic areas (e.g., megacities) are settled in relation to sedimentary basins (e.g., river valleys); therefore a realistic definition of the seismic input that takes into account site response has become one of the most relevant tasks in seismic engineering analysis. In the last decade, a huge amount of literature has been dedicated to estimation of the site effects, and a practical definition of the site effect, that combines the purposes of the engineering and seismological communities, is proposed by Field (1996): "the unique behavior of a site, relative to other sites, that persists given all (or most) of the potential sources of earthquake ground

motion in the region". Such a definition implicitly reveals the difficulties connected with the correct site response estimation, i.e., identification of the different ingredients involved in the resulting ground motion signal: source, path (including the presence of lateral heterogeneities), and local soil effect including its possible nonlinear behavior. The nonlinear effects will not be treated in the following; we just mention that the assumption of linearity between stress and strain can be no longer valid for accelerations larger than 0.1-0.3 g, quite important values from the seismic engineering point of view (Beresnev and Wen, 1996). In fact, due to nonlinearity the actual shear wave velocity decreases with increasing stress, and hysteresis leads to energy loss at any deformation cycle. As a consequence, the resonance of surficial layers can be shifted to lower frequencies, and this can lead to a lower amplification of ground motion at higher frequencies.

The experimental approach to estimation of the site response is based on the measure of ground motion at different sites. This implies the recording, with a network of instruments, of multiple seismic sources. If a network of I sites has recorded J events, the amplitude spectrum, O, of the j-th event recorded at the i-th site is usually represented as (Field and Jacob, 1995):

$$O_{ij}(\omega) = E_j(\omega) \cdot P_{ij}(\omega) \cdot S_i(\omega) \qquad (119)$$

where E is the source term, P is the path term, and S is the site-effect term. The most traditional techniques for estimation of the S term are based on computation of the ratio between the spectrum of the signal (or a portion of it) at

the sedimentary site and the spectrum of a reference signal, preferably recorded at a nearby bedrock site (Borcherdt, 1970). Andrews (1986) recasted the traditional method into a generalized-inverse problem by solving for all the site-effect and source terms simultaneously. However, quite often a signal recorded on bedrock is not available close to the investigated sites, so that directional effects due to the source could become relevant. Some techniques have been proposed that are non-reference-site dependent: for example, Boatwright et al. (1991) proposed a parametrized source and path inversion scheme based on some assumptions regarding the source-spectra, frequency and distance attenuation laws, etc.

An alternative approach is based on the spectral ratio between the horizontal and vertical components of motion. This method was originally applied by Langston (1979) for crustal and upper mantle studies and it is based on the assumption that propagation of the vertical component of motion (in general only S-waves are considered) is minimally perturbed by the surficial layers, and therefore, it can be used to remove source and path effects from the horizontal components. Lermo and Chávez-García (1993) applied the same technique at higher frequencies for the site response estimation in Mexico city. Similarly, Nakamura's (1989) method is based on computation of the spectral ratio between horizontal (usually the square root of the product between the spectra of the NS and EW components is used) and vertical components obtained from seismic noise (microtremors). Theoretical investigations (e.g., Lachet and Bard, 1994; Dravinski et al., 1996) and experimental studies (e.g., Field and Jacob, 1995; Field, 1996) have shown that Nakamura's method can reveal the fundamental resonant frequency of a site but that it is usually not able to give the correct amplification

level. Furthermore, Nakamura's (1989) assumptions seem questionable since several studies (e.g., Lachet and Bard, 1994; Konno and Ohmachi, 1998) have demonstrated that the horizontal to vertical ratio is strictly correlated with the polarization of Rayleigh waves.

Table 4 summarizes schematically the most frequently used techniques for the empirical estimation of site effects. These techniques supply reliable information about the site response to noninterfering seismic phases; they are not always adequate in most real cases when the seismic sequel is formed by several interfering waves. For each technique the signal type used (i.e., earthquakes or ambient noise signals), its characteristic (i.e., if it is a reference site dependent technique or not), and a bibliographic reference are given. For a more comprehensive comparison of the various empirical techniques the reader is referred to Bard (1997).

An alternative to the experimental approach to site response estimation is based on computer codes, developed from detailed knowledge of the seismic source process and the propagation of seismic waves. This approach can simulate the ground motion associated with a given earthquake scenario. In such a way, using available geological and geotechnical information, a low-cost parametric analysis can be performed, since the installation of site arrays in each zone with a high level of seismicity is too expensive an operation.

Table 4. Summary of the most frequently used techniques for the empirical estimation of the site response.

Technique	Earthquake (E) or microtremors (M)	Reference site (R) or not (NR)	Example reference
Sediment/bedrock (S/B)	E	R	Borcherdt (1970)
Generalized inversion scheme	E	R	Andrews (1986)
Parametrized source and path inversion	E	NR	Boatwright et al. (1991)
Coda waves analysis	E	NR	Philips and Aki (1986)
Horizontal/vertical (H/V) (receiver function)	E	NR	Lermo and Chávez-Garcia (1993)
Sediment/bedrock (S/B)	M	R	Yamanaka et al. (1993)
Horizontal/vertical (H/V)	M	NR	Nakamura (1989)
Array analysis	M	NR	Malagnini et al. (1993)

In principle all techniques presented in Sect. 3 could be used for the theoretical estimation of the site response, each one being more or less suited according to the problem to be solved. For example, it has been shown that boundary techniques (Dravinski et al., 1996), and domain techniques (Coutel and Mora, 1998) can be used to test the reliability of empirical techniques, as well as to study the dependence of the site response on source and path parameters. Progress in computational techniques has allowed extension of numerical analysis to 3-D structural models by using domain methods such as finite difference methods (e.g., Olsen and Archuleta, 1996; Graves, 1998). These techniques could be useful in areas characterised by severe subsurface topography and by embedded extended faults (e.g., the Los Angeles basin), in order to study the 3-D diffraction effects and the 3-D ground motion

amplifications. However, computational demands limit the application of 3-D techniques to periods greater than 1 s and to seismic velocities larger than 1 km/s; the corresponding minimum wavelength is on the order of 1 km, which represents the limit of the spatial resolution of such modelling.

5.2.2 *Examples of ground motion scenarios*

In the following we consider two examples of the application of deterministic techniques for seismic hazard assessment at a subregional and urban scale, showing results for the Catania (Sicily) area, where the mode coupling analytical technique (see Sect. 4) is used, and for the city of Rome, where the modal summation–finite difference hybrid method (see Sect. 3.1.3) is used. These results are produced in the framework of the IUGS-UNESCO-IGCP Project 414 (e.g., Panza et al., 1999b).

5.2.2.1 Site response estimation in the Catania (Sicily) area

A realistic definition of the seismic input for the Catania area is obtained using the modelling techniques, described in Sect. 4, that allow us to create a database of synthetic signals which can be used for the study of the local response in a set of selected sites located within the Catania area.

The main task is to define a scenario corresponding to an earthquake of the same size as the destructive event that occurred on January 11, 1693. From analysis of the felt intensities (up to XI) it has been possible to estimate a magnitude ranging from 7.0 to 7.8 (e.g., Boschi et al., 1995; Decanini et al., 1993).

It is very difficult to determine the source characteristics for such a historical event, as the macroseismic data are the only available information. The poor

control over hypocentral coordinates does not permit use of the macroseismic data for inversion of the source mechanism, but with these data it is possible to perform an analysis to test the validity of the source mechanism models that can be formulated on the basis of seismotectonics. The observed intensities can be converted into accelerations, velocities, or displacements (e.g., Decanini et al., 1995; Panza et al., 1997; 1999a) and they can be compared with the synthetic data. Applying such a procedure to the 1693 event (Romanelli et al., 1998a,b), good agreement with the macroseismic data is obtained for a seismic source located on the Northern Segment of the off-shore Hyblean fault, which is considered the most important seismogenic structure of the zone.

Because our attention focuses on the lateral variations of the model, to minimize the number of free parameters we account for source finiteness by properly weighting the point source spectrum using the scaling laws of Gusev (1983), as reported in Aki (1987). We have chosen these curves for several reasons: compared to ω^{-2} spectra (e.g., Joyner, 1984; Houston and Kanamori, 1986), Gusev curves, that are based on solid statistical analysis of experimental data, are more conservative in the range from 2 to 0.1 s; they often provide a corner frequency that allows us to fit the observed amplitudes with the synthetic seismograms (e.g., Vaccari, 1995; Moldoveanu and Panza, 1999).

The focal mechanism parameters of the source, located approximately in the center (latitude: 37.44°; longitude: 15.23°) of the Northern Segment of the Hyblean fault, are strike = 352°, dip = 80°, rake = 270°, focal depth = 10 km, and seismic moment = $3.5 \cdot 10^{19}$ Nm.

For definition of the model, we use the geotechnical information collected within GNDT (GNDT, 1997): a simplified geotechnical zonation map and a set of five detailed geotechnical cross sections. Because our method can be applied to both rough and detailed laterally heterogeneous models, we first employ the simplified map, to analyze effects of the gross features of geotechnical zonation on ground motion. As a second step, in order to test the usefulness of the simplified models, we consider a detailed version of one of the simplified cross sections.

In Fig. 37 the simplified geotechnical zonation map for the Catania area, together with the 13 cross sections considered in the analysis, are shown. Along each section, a set of sites is considered and the site locations are chosen both in the proximity of the boreholes and at the edges of the section. The laterally varying models associated with each cross section are built up by putting in welded contact (from 2 to 4) different 1-D local models: the regional model, assigned to Eastern Sicily (Costa et al., 1993), is chosen as the bedrock model and the geotechnical information related with the selected boreholes are used for definition of the local models. Synthetic signals are calculated with the modal summation technique for laterally heterogeneous models (see Sect. 4), with a cut-off frequency of 10 Hz. The map shown in Fig. 37 defines the borders between the local models, i.e., the distances between the vertical interfaces separating the different 1-D models. In Fig. 37 the velocity time series calculated, for the transverse component of motion, corresponding to all sites, are shown. Their spectra show that most of the energy is present for frequencies below 4 Hz. Each record is 20 s long and is normalized to the peak velocity value, VMAX, for the entire region. The largest computed values of VMAX are consistent with the

reported macroseismic intensity value, XI (Tables 1 and 2). Fig. 37 shows how the source and propagation effects can combine a big variety of signals; if laterally heterogeneous models and azimuthal dependencies are included in the analysis, the parameters describing the ground motion are strongly site dependent.

For section S10 (dot-dashed line in Fig. 37) detailed geotechnical information is available (GNDT, 1997), and we examine it with the purpose of comparing the results obtained using a simplified laterally heterogeneous model with those obtained for a realistic model of a geological cross section.

The detailed laterally heterogeneous model used for calculation of the synthetic seismograms along S10 is built up using 48 local models in welded contact, for a total extension of approximately 13 km. The geological cross section and its detailed model are shown in Fig. 38, together with the elastic parameters of each geotechnical unit; the Q values vary in the range from 40 to 300, depending upon the unit considered. The source is buried in the regional bedrock model.

The results shown by Somerville (1996), who supplies the ground motions for a magnitude 7.0 earthquake on the northern Hayward fault, and the spectral analysis of the signals shown in Fig. 37 indicate that a reasonable upper frequency limit in the calculations can be 4 Hz.

The signals are calculated for a set of sites, one for each local model, along the section; in Fig. 38 a set of selected signals is shown for the transverse component of motion. We give an estimation of the local response at a given site, evaluating the response spectra ratio (RSR) corresponding to the laterally varying model and to the bedrock model.

Figure 39 shows the variation of the RSR (SH motion) along the profile: (a) shows the RSR at four selected frequencies (0.2, 0.5, 1.0, and 2.5 Hz) obtained using the signals calculated with a strike-section angle equal to 80°; (b) is obtained for a value of the strike-section angle equal to 180°, that corresponds to a maximum of the SH radiation pattern in the direction of the cross-section. As expected, at low frequencies (0.2 - 0.5 Hz) the ratios are approximately 1 along all the section, but at higher frequencies the wavelengths are comparable to the dimensions of the lateral heterogeneities, and the local effects become important. The shape of the curves corresponding to 2.5 Hz seems to resemble the subsurface topography of the Alf and Aa layers, respectively. In Fig. 39c and d the RSR versus the epicentral distance and frequency are shown for strike-section angles equal to 80 and 180°, respectively. For the first part of the section (up to an epicentral distance of approximately 20 km) the amplification patterns are practically the same, but in the remaining part the amplification levels change significantly. This example shows that the interference between the seismic waves and the lateral heterogeneities is azimuthally dependent and may therefore be responsible for different responses in the same site (e.g., Field, 1996; Riepl et al., 1998). Such a result sends a warning against the general use of the schematic representation used in Eq. (119) and of determinations of the validity of local soil effects made with very popular methods that do not consider the realistic propagation and interference of seismic waves.

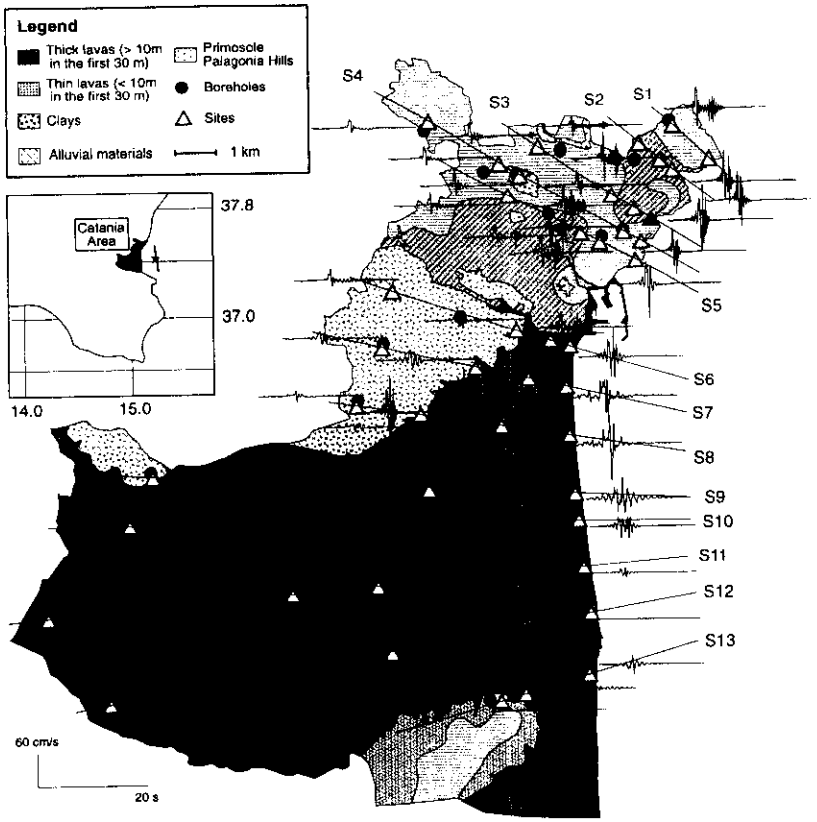

Fig. 37. Simplified geotechnical zonation map for the Catania area and the first 20 s of the velocities time series, calculated at the sites. Each signal is scaled to the maximum value of VMAX (63 cm/s) over the entire area (black triangle) (modified from Romanelli and Vaccari, 1999).

Results obtained using the detailed model for section S10 can easily be compared with those from the simplified model. A set of 48 synthetic signals is calculated along S10, using the simplified laterally heterogeneous model shown in Fig. 40a, at the same epicentral distances used for computation of the signals

for the detailed model. These signals have been lowpass-filtered with a cut-off frequency of 4 Hz. In Fig. 40b-c the RSR are shown, versus epicentral distance and versus frequency, for the strike-section angle equal to 80°: (b) shows the results corresponding to the detailed section (same as Fig. 39c), while (c) shows the results obtained using the simplified model. The RSR corresponding to the simplified model has a very sharp discontinuity close to the beginning of the local model at an epicentral distance of 13 km. This discontinuity is responsible for the excitation of high-frequency diffracted waves that are rapidly decaying with increasing distance from the boundary. Away from the boundary, the pattern assumes a relatively simple shape: the greater amplifications are obtained at a frequency of approximately 1.5 Hz, that is the value of the fundamental resonant frequency for the stack of local layers shown in the left part of Fig. 40a. The results summarized in Fig. 40 show that the extension of punctual information to extended sections, i.e., the adoption of simplified models, could lead to misleading conclusions concerning the seismic response of sedimentary basins.

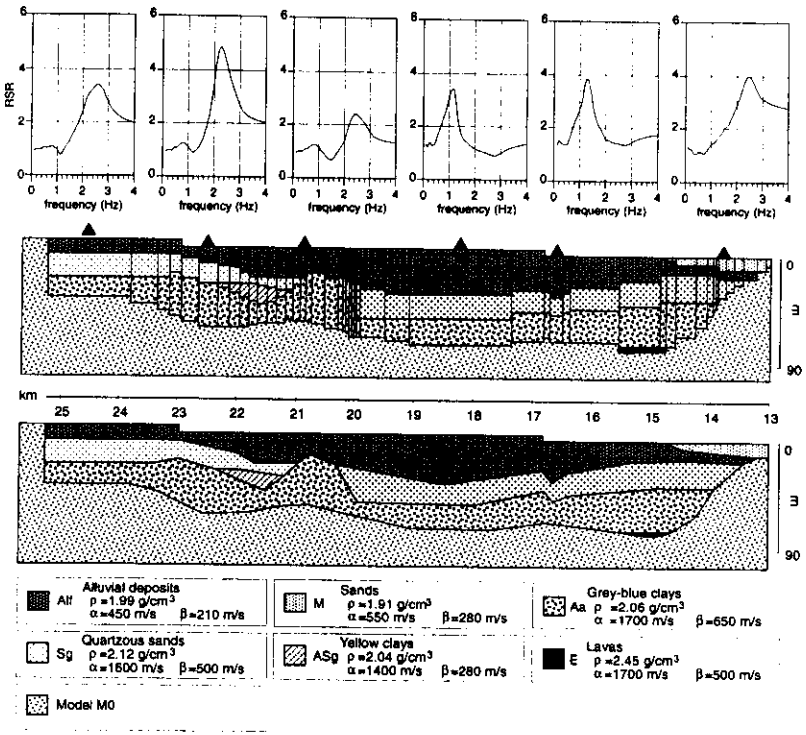

Fig. 38. Cross-section (bottom) and corresponding model for section S10. The distance along the section is measured in km from the source, while the vertical scale is in m. Six selected RSR, are shown (modified from Romanelli and Vaccari, 1999).

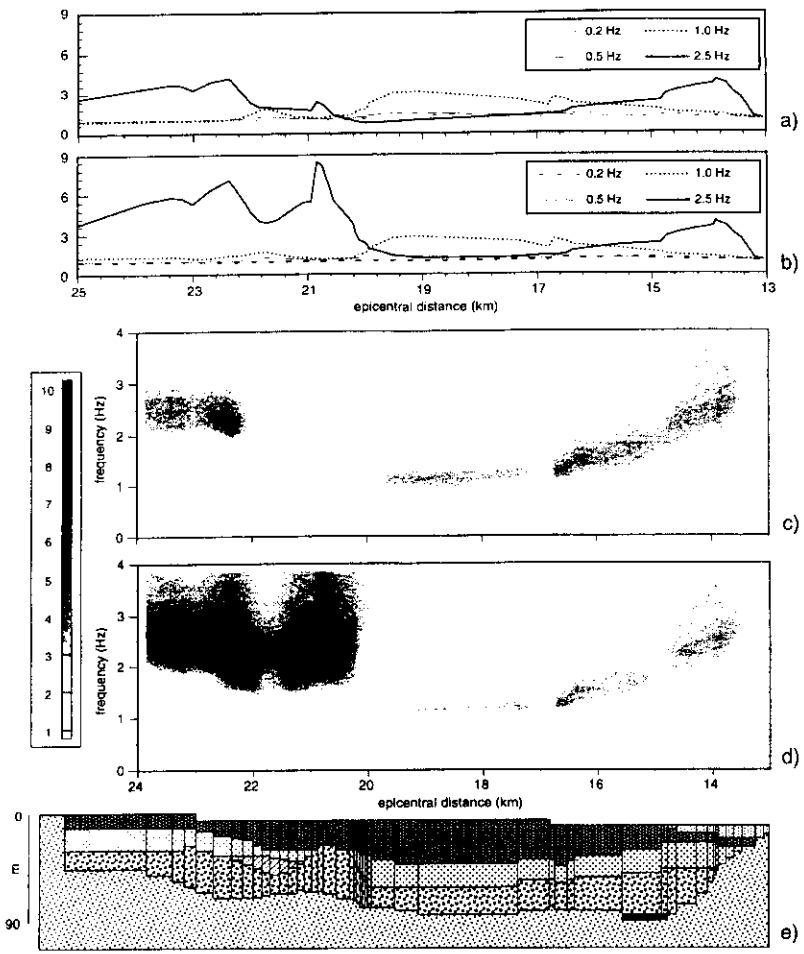

Fig. 39. (a) RSR at four selected frequencies (0.2, 0.5, 1.0, and 2.5 Hz) versus epicentral distance, for the transverse component of motion; strike-section angle is equal to 80°. (b) Same as (a) but the strike-section angle is equal to 180°. (c) RSR versus epicentral distance and versus frequency; strike-section angle is equal to 80°. (d) Same as (c) but the strike-section angle is equal to 180° (modified from Romanelli and Vaccari, 1999). (e) Model for S10.

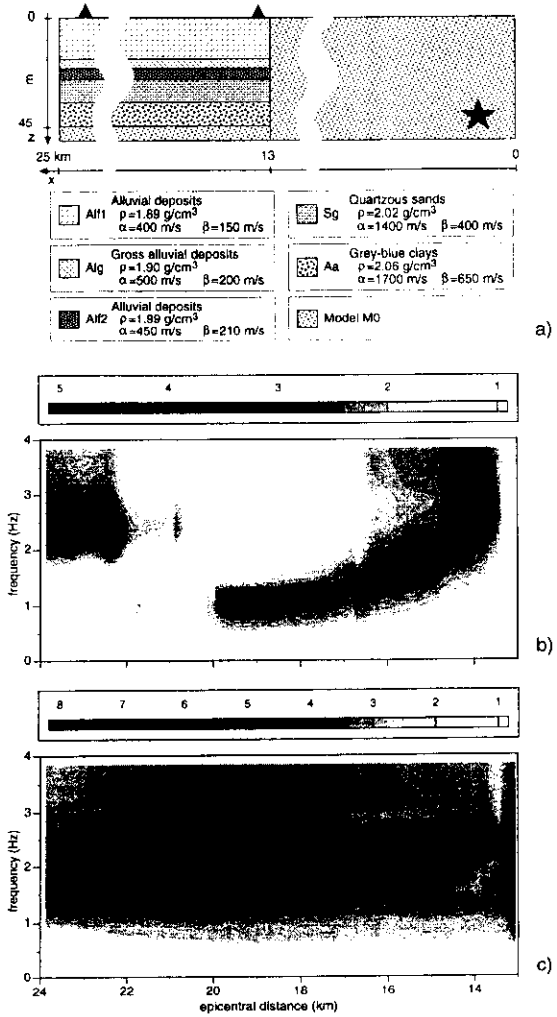

Fig. 40. (a) Simplified model of S10 constructed from the geotechnical map shown in Fig. 37. Comparison of the RSR obtained for the detailed (b) and for the simplified (c) laterally heterogeneous models of section S10. The RSR are plotted versus the epicentral distance and versus frequency for the strike-section angle equal to 80°. The gray scales are different in the two cases.

Therefore, an accurate estimation of the site effects in complicated geometries requires a parametric study that takes into account the complex combination of the source and propagation parameters.

The RSR, obtained using the synthetic signals calculated for the P-SV motion along the detailed section S10, are shown versus epicentral distance and frequency in Fig. 41. The strike-section angle is 80°, a value that, for the given focal mechanism, corresponds approximately to a maximum in the radiation pattern for the P-SV waves. For epicentral distances less than about 20 km the pattern of the resonance frequencies, shown in Fig. 41a (radial component), is in good agreement with the pattern visible in Fig. 41c and d. Fig. 41b shows that, in this case, the vertical component of motion is not affected significantly by the local geological conditions.

The fact that the vertical component of motion is free from near surface influences is one of the original assumptions (Nakamura, 1989) of the horizontal-to-vertical spectral ratio technique (H/V RSR) for the estimation of the site response. The main advantage of this technique is its independence from the reference-site. If earthquake recordings are used, the H/V technique is usually called the receiver function technique (Lermo and Chávez-García, 1993) while if ambient noise recordings are considered it is known as Nakamura's technique (Nakamura, 1989). In Fig. 41c the H/V RSR are shown versus epicentral distance and frequency. The calculations confirm the empirical conclusions that the resonance patterns are very well correlated with surface geology, but the absolute level of amplification cannot be straightforwardly determined (Theodulidis et al., 1996; Lachet and Bard, 1994). The H/V RSR obtained for the bedrock model (not shown) has a simple pattern, with a practically constant

value of the resonance frequency along the path. This is in agreement with the theoretical explanation concerning the physical meaning of the H/V RSR: the vertical component of Rayleigh wave motion has a minimum or vanishes, according to the vertical velocity contrast, around the S-wave resonance frequency, and the H/V RSR is a sort of mapping of the ellipticity curve of Rayleigh wave modes (e.g., Panza, 1985; Panza and Suhadolc, 1987; Lachet and Bard, 1994; Konno and Ohmachi, 1998).

The synthetic signals database assembled for the Catania area, which can easily be expanded to other earthquake scenarios, can be used as seismic input in subsequent engineering analyses, at a very low cost/benefit ratio. For estimation of the destructive potential of some of the signals calculated for the simplified models (e.g., Fig. 37), some parameters, obtained from their (a) direct analysis, (b) integration in the time or frequency domain, and (c) the structural (elastic and anelastic) response, have been investigated by Decanini et al. (1999). On the basis of the parameters characterizing earthquake destructive power, derived from available strong motion records, the results show that the synthetic signals provide an energy response which is typical of accelerograms recorded on intermediate-firm soil, at a distance from the causative fault between 12 and 30 km, and with a magnitude between 6.5 and 7.1.

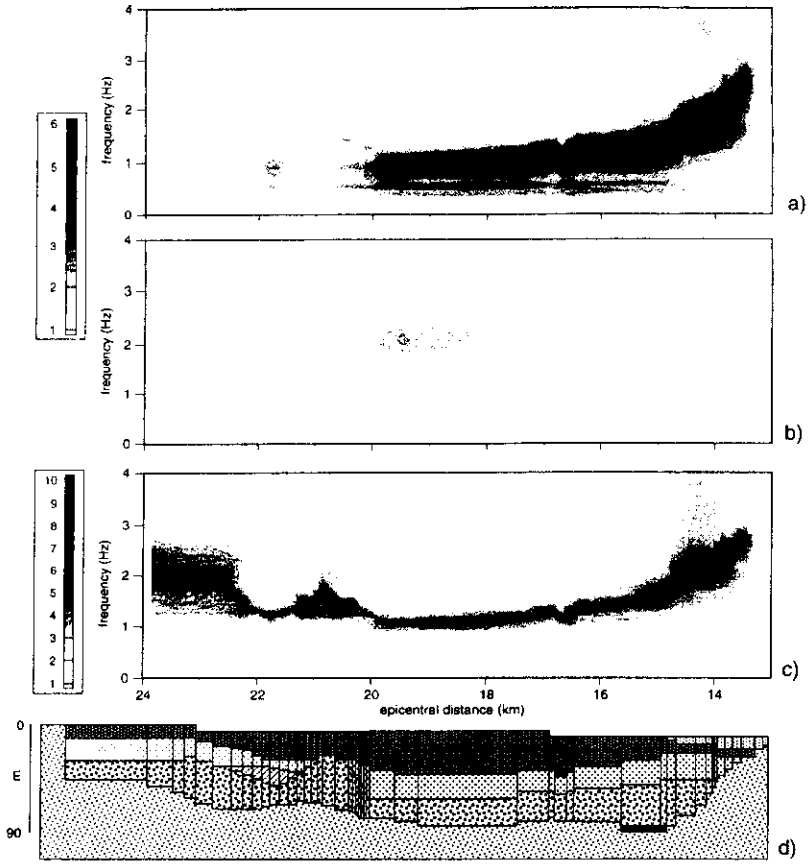

Fig. 41. (a) RSR for the radial component of motion versus epicentral distance and frequency; (b) RSRs for the vertical component of motion versus epicentral distance and frequency; (c) H/V RSR versus epicentral distance and frequency. Strike-section angle equal to 80° (modified from Romanelli and Vaccari, 1999). (d) Model of S10. The gray scale in (c) is different from the ones in (a) and (b).

5.2.2.2 *Microzoning of Rome*

A large quantity of descriptions of earthquakes that have been felt in Rome is available (Ambrosini et al., 1986; Molin et al., 1986; Basili et al., 1987). Use of the hybrid method described in Sect. 3.2.2 allows us to give a simple and natural explanation of the damage distribution observed as a consequence of the the January 13, 1915, Fucino earthquake - one of the strongest events to have occurred in Italy during this century (Intensity XI on the Mercalli-Cancani-Sieberg, MCS, scale). The well-documented distribution of damage in Rome, caused by the Fucino earthquake, is successfully compared by Fäh et al. (1993b; 1995) with the results of a series of different numerical simulations, using AMAX and the so-called total energy of acceleration, W (Jennings, 1983), which is proportional to the Arias Intensity (Arias, 1970).

High relative AMAXs are obtained where the impedance of surficial sediments is small, whereas relative AMAXs are low where volcanic rocks are thick, and this is in good agreement with the observed damage distribution. An even better correlation with the observed damage is obtained considering the relative W. An additional important result of Fäh et al. (1993b) is the demonstration that sharp variations in the spatial distribution of spectral ratios can be due to polarization of P-SV waves into the radial component, a resonance effect similar to the one described in Sect. 5.2.2.1 for the H/V RSR, even when the geometry of the different sedimentary layers is relatively regular. This is quite a logical explanation of the often observed concentration of damage in very small, scattered zones, and it is easier to accept than the often invoked presence of unlikely abrupt variations in the geotechnical properties of the subsoil. Similar

results have been obtained by Marrara and Suhadolc (1998) in a case study at Thessaloniki.

The good correlation between AMAX, W, and the damage statistics makes it possible to extend zoning to the entire city of Rome, thus providing a basis for the prediction of expected damage from future strong events.

In addition to the Central Apennines, whose earthquakes caused maximum intensity VII-VIII (MCS) in Rome and may generate significant perturbations at long periods (Figs. 30 and 31), the most important seismogenic zone (Fig. 42) the earthquakes of which can cause structural damage in Rome are the Alban Hills (observed maximum MCS in Rome VI-VII) (Molin et al., 1986). Therefore, Fäh et al. (1995) used the sources shown in Fig. 42: (1) the epicenter of the January 13, 1915, Fucino earthquake, (2) the Carseolani Mountains where, from the study of pattern recognition (Caputo et al., 1980), a strong earthquake is expected to occur, and (3) the Alban Hills. The source mechanisms assigned to these earthquakes are the mechanism of the Fucino earthquake (Gasparini et al., 1985) for event 1 and 2, and the mechanism of an earthquake in the Alban Hills (Amato et al., 1984) for event 3.

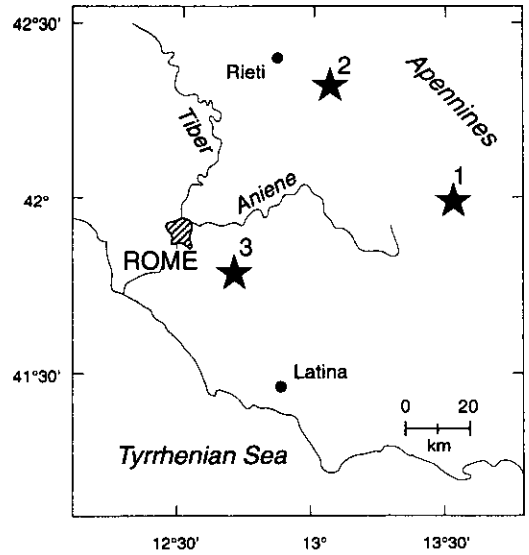

Fig. 42. Epicenter locations of the events considered in the numerical simulations used for microzoning. The source positions are (1) the epicenter of the January 13, 1915 Fucino earthquake, (2) the Carseolani Mountains, and (3) the Alban Hills (after Fäh et al., 1995).

Fäh et al. (1995) consider the RSR computed along the profiles of Fig. 43, and using the results obtained from the modelling of the Fucino event, they define the six zones shown in Fig. 44: zone 1 includes the edges of the Tiber river, zone 2 extends over the central part of the alluvial basin of the Tiber, zone 3 includes the edges of the Paleotiber basin, and zone 4 extends over the central part of the Paleotiber basin. Zones 5 and 6 include areas located outside the large basins of the Tiber and Paleotiber where we distinguish between areas without (zone 5) and without (zone 6) a layer of volcanic rocks close to the surface. Some of these zones can also be recognized in the sections considered in relation to the events located in the Carseolani Mountains and the Alban Hills (Fig. 44). The RSR have

been computed for all the sites located in each of the six zones, for all two-dimensional models, shown in Fig. 42, and for all three events, located in Figure 5.20. From these values the average and the maximum RSR (shown in Fig. 45) for zero and 5% damping of the oscillator, are determined for each given zone.

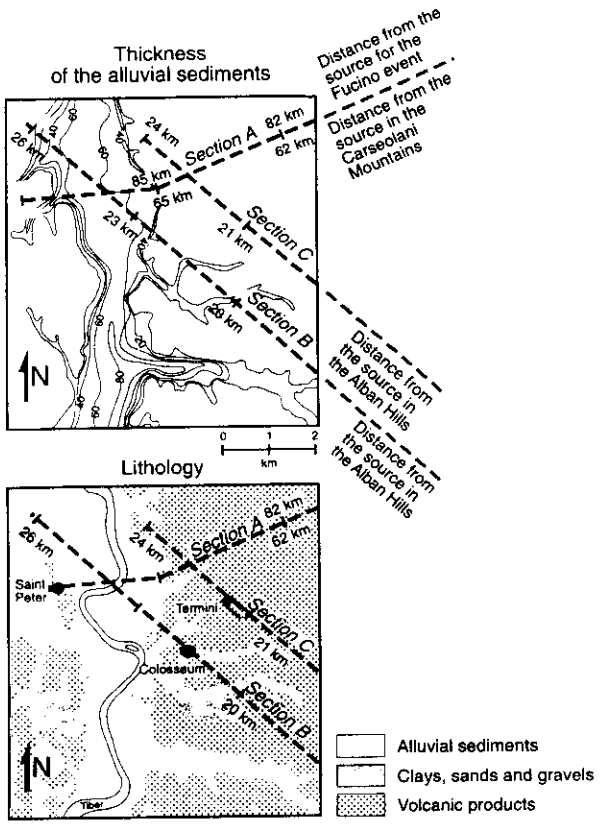

Fig. 43. Lithology and thickness of the alluvial sediments in Rome (Ventriglia, 1971; Funiciello et al., 1987; Feroci et al., 1990). The dashed lines indicate positions of the cross sections, for which numerical modelling is performed (after Fäh et al., 1995).

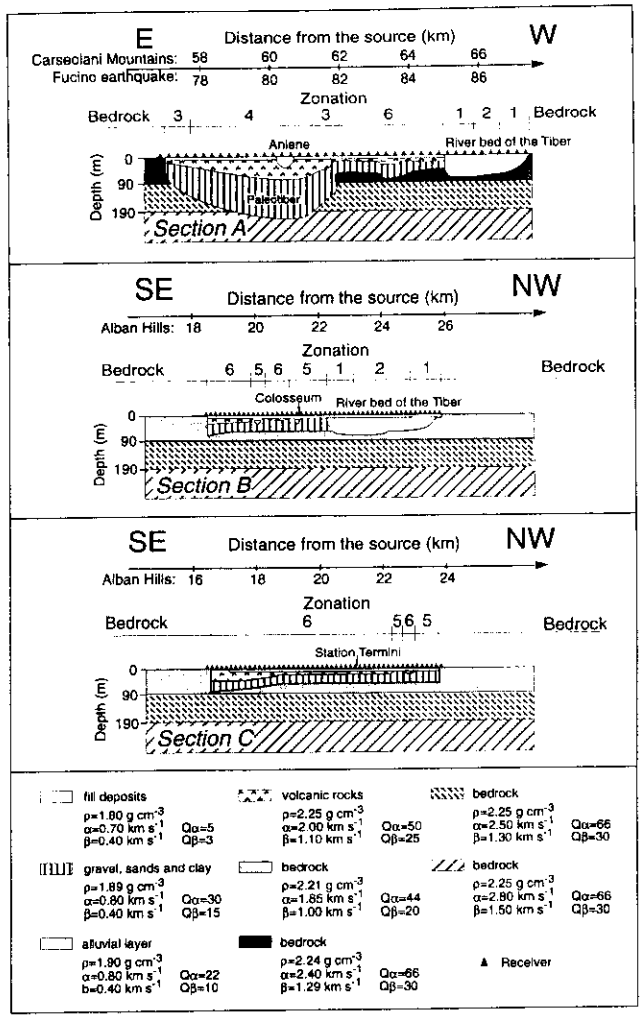

Fig. 44. Two-dimensional models corresponding to the dashed lines shown in Fig. 43. Only the part near to the surface is shown, where the laterally varying model deviates from the horizontally layered bedrock reference models. The microzonation, identified by numbers from 1 to 6, is described in the text (after Fäh et al., 1995).

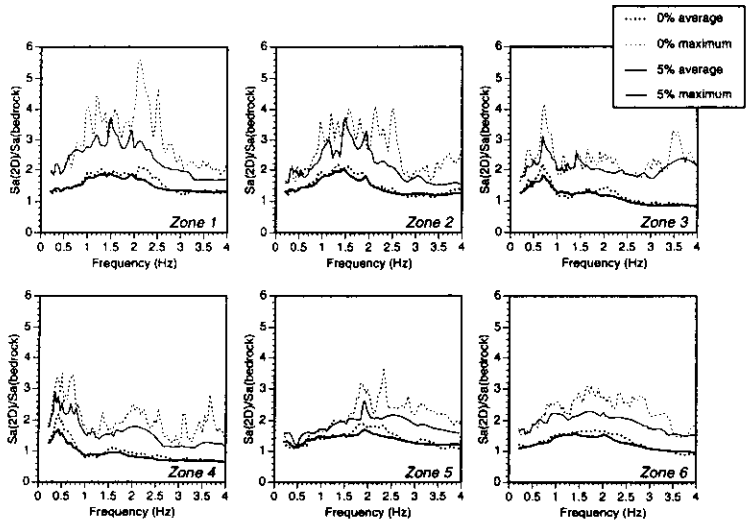

Fig. 45. Maximum and average RSR for the zones defined in Fig. 44, for zero damping and 5% damping (after Fäh et al., 1995).

Whenever possible, the spectral characteristics defined in Fig. 45 have been assigned to areas located outside the profiles, but characterized by a lithological setting close to one of the six zones identified (see Fig. 44). In such a way, the zoning performed along the three sections has been extended to larger areas using the information available on geological and geotechnical conditions. The result of such tentative extrapolation is shown in Fig. 46.

Given that in Rome the DGA calculated for a bedrock model is about 0.1 g (see Fig. 27), the absolute response spectra that one should expect in the six zones of Fig. 46 is shown in Fig. 47. We may assume that the DGA expected in each zone can be obtained by dividing the largest spectral value by 2.5 (as is the case for EC8 design spectrum). Therefore in Rome the largest estimated DGA is about

0.2g. Using the correlation between DGA and intensity given in Tables 1 and 2 the intensity is either X or IX, respectively. The intensity due to the 1915 Fucino earthquake (90 km from Rome, M=7.3 in catalogue NT4.1) is VIII. The conservative values we obtain are due to the smoothing of magnitude (smoothing 1, described in Sect. 5.1) and to the geometry of the seismogenic zones, which permits us to account for possible stronger events that might occur closer to the city. Actually, after the smoothing procedure, a magnitude as large as the one of the Fucino event is associated with a source 45 km from Rome. On the other hand if we want to compare our modelling with the observations, applying smoothing 2 (Sect. 5.1.1), the DGA reduces to 0.10 g. From Tables 1 and 2, the corresponding intensity is either IX or VIII, respectively, well compatible with observations (Molin et al., 1986).

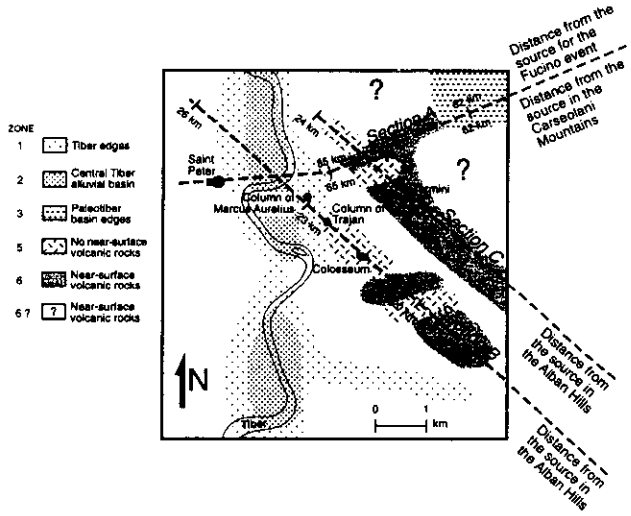

Fig. 46 Microzoning for the city of Rome.

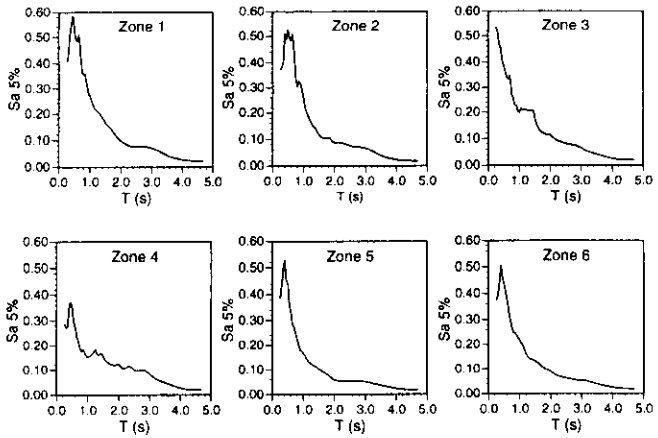

Fig. 47. Spectral accelerations (5% damping) in units of g for the 6 zones shown in Fig. 44.

Thus, in the absence of instrumental data, and without having to wait for a strong earthquake to occur, a realistic numerical simulation of the ground motion has been used for microzonation of Rome. The highest values of the spectral amplification are observed at the edges of the sedimentary basin of the Tiber, and strong amplifications are observed in the Tiber river bed. This is caused by the large amplitudes and long duration of the ground motion due to (1) low impedance of the alluvial sediments, (2) resonance effects, and (3) excitation of local surface waves. The presence of near-surface rigid volcanic rocks is therefore not sufficient to classify a location as a *hard-rock* site, since the existence of an underlying sedimentary complex can cause amplifications due to resonance effects. Reliable zonation requires knowledge of both the thickness of the surficial layer and of the deeper parts the structure, down to the real bedrock. This is especially important in volcanic areas, where volcanic flows often cover alluvial basins.

6. Summary and conclusions

Traditional deterministic methods for seismic zoning can lead to only a kind of *postevent* zoning whose validity cannot easily be extrapolated in time and to different regions and which, therefore, must be considered obsolete.

The ability to estimate accurately seismic hazard at very low probability of exceedance may be important in protecting of special objects in the built environment against rare earthquakes. The deterministic approach, based upon the assumption that several earthquakes can occur within a predefined seismic zone, represents a conservative definition of seismic hazard for *preevent* localized planning for disaster mitigation, over a broad range of periods.

Computation of realistic synthetic seismograms, using methods that take into account source, propagation, and site effects, and utilising the huge amount of available geological, geophysical, and geotechnical data, goes well beyond the conventional deterministic approach and gives a powerful and economically valid scientific tool for seismic zonation and microzonation.

The definition of realistic seismic input can be obtained from computation of a wide set of time histories and spectral information, corresponding to possible seismotectonic scenarios for different source and structural models. Such a data set can be fruitfully used by civil engineers in the design of new seismo-resistant constructions and in the reinforcement of the existing built environment, and can therefore provide a particularly powerful tool for the prevention aspects of Civil Defence. The possibility of modelling broad-band seismic input is a useful tool for engineering design and for the retrofitting of special objects, with relatively long free periods, and is acquiring continuously increasing importance, due to the widespread existence, in the built environment, of special objects.

The procedure is scientifically and economically valid for immediate action, since there is no need to wait for a strong earthquake to occur. First order zonations can be made at regional scale, considering average structural models and a set of sources with damaging potential distributed within the identified seismogenic areas. Seismic microzonations of urban areas can be performed even more accurately when the required geotechnical data are available, so that local site effects can be soundly modelled.

A practical definition of site effect, that accounts for both the seismological and engineering point of view, is the one given by Field (1996): "the unique behaviour of a site, relative to other sites, that persists given all (or most) of the potential sources of earthquake ground motion in the region." This definition implicitly indicates the difficulties connected with a correct estimate (or prediction) of the site effect. These are the determination and separation of the other factors contributing to the seismic signal: source effect, path effect (including lateral heterogeneity), and possible (but not considered here) nonlinear soil response. The theoretical site response estimations that we performed using different types of seismic motion and different techniques, confirm that the identification of the behavior of a site with a set of resonant frequencies could be a very difficult task, especially when the amplification is azimuthally dependent. Furthermore, our results show that the extension of discrete information for limited areas to extended sections, i.e., the adoption of simplified models, could lead to misleading conclusions concerning the seismic response of sedimentary basins. The results suggest that, in order to perform an accurate estimate of the site effects in complicated geometries, it is necessary to make a parametric study that takes into account the complex combination of the source and propagation parameters.

Acknowledgements

We would like to express our gratitude to Mrs. Dilys Grilli, Publications Section, for editing the English language of the entire manuscript, to Prof. Betim Muço for his permission to show the seismic zonation results for Albania, yet unpublished, and to an anonymous referee for the careful and fruitful review work. We acknowledge support by CNR Grants 96.02986.PF54, 97.00540.PF54, and 98.03238.PF54; European Union Grants CIPA-CT94-0238, EV5V-CT94-0513, and ENV4-CT96-0491, NATO Grant ENVIR. LG 960916 677(96); and Italian MURST 40 and 60% funds (1996-1998). Part of this research is a contribution to the IUGSUNESCO-IGCP Project 414 "Realistic Modelling of Seismic Input for Megacities and Large Urban Areas".

UVO
Seismic safety of urban areas: ground motion modelling and intermediate-term earthquake prediction

Realistic Modelling of Seismic Input for Megacities and Large Urban Areas (project 414)

References

A.A.V.V., 2000. *Seismic hazard of the Circum-Pannonian region*, (G. F. Panza, M. Radulian and C.-Y. Trifu editors), PAGEOPH Topical Volumes,**157**, Birkhouser, Basel.

Aki, K, 1987, Strong motion seismology, in M. Erdik and M. Toksöz (eds) *Strong ground motion seismology*, NATO ASI Series, Series C: Mathematical and Physical Sciences, D. Reidel Publishing Company, Dordrecht, Vol. 204, pp. 3-39.

Aki, K. and Richards, P. G., 1980. *Quantitative Seismology*, Freeman and Co., San Francisco.

Alsop, L. E., 1966. Transmission and reflection of Love waves at a vertical discontinuity, *J. Geophys. Res.*, **71**, 3969-3984.

Alsop, L. E., Goodman, A. S. and Gregersen, S., 1974. Reflection and transmission of inhomogeneous waves with particular application to Rayleigh waves, *Bull. Seism. Soc. Am.*, **64**, 1635-1652.

Alterman, Z. S. and Karal, F.C., 1968. Propagation of elastic waves in layered media by finite difference methods, *Bull. Seism. Soc. Am.*, **58**, 367-398.

Alvarez, L., Vaccari, F. and Panza, G. F., 1999. Deterministic seismic zoning of eastern Cuba, *PAGEOPH* , **156**, 469-486.

Amato, A., De Simoni, B. and Gasparini, C., 1984. Considerazioni sulla sismicità dei Colli Albani. Atti del 3° Convegno del Gruppo Nazionale di Geofisica della Terra Solida, CNR, Roma, **2**, 965-976.

Ambrosini, S., Castenetto, S., Cevolani, F., Di Loreto, E., Funiciello, R., Liperi, L. and Molin, D., 1986. Risposta sismica dell'area urbana di Roma in occasione del terremoto del Fucino del 13 gennaio 1915. Risultati preliminari, *Mem. Soc. Geol. It.*, **35**, 445-452.

Andrews, D. J., 1986. Objective determination of source parameters and similarity of earthquakes of different size, in *Earthquake Source Mechanics* (Das, S., Boatwright, J. and Scholz C. H. editors), American Geophysical Union, Washington D.C., 259-268.

Aoudia, A., Vaccari, F., Suhadolc, P. and Meghraoui, M., 2000. Seismogenic potential and earthquake hazard assessment in the Tell Atlas of Algeria, *J. of Seismology.*, **4**, 79-98.

Arias, A., 1970. A measure of earthquake intensity. In: Seismic design for nuclear power plants (Ed. R. Hansen), Cambridge, Massachussets.

Babich, V. M., 1956. Ray method for the computation of the intensity of wavefronts, *Nauka*, in russian.

Bard, P.-Y., 1997. Local effects on strong ground motion: basic physical phenomena and estimation methods for microzoning studies, *in SERINA- Seismic Risk: An Integrated Seismological, Geotechnical and Structural Approach* (ITSAK Ed.), Thessaloniki.

Basili, A., Favali, P., Scalera, G. and Smriglio, G., 1987. Valutazione della pericolosità sismica in Italia centrale con particolare riguardo alla città di Roma. Atti del 6° Convegno del Gruppo Nazionale di Geofisica della Terra Solida, CNR, Roma, 379-393.

Ben-Menhaem, A. and Harkrider, D. G., 1964. Radiation patterns of seismic surface waves from buried dipolar point sources in flat stratified media, *Bull. Seism. Soc. of Am.*, Vol. **69**, 2605-2620.

Beresnev, I. A. and Wen, K. L., 1996. Nonlinear soil response-a reality?, *Bull. Seism. Soc. of Am.*, Vol. **86**, No. 6, 1964-1978.

Bernard, P. and Zollo, A., 1989. The Irpinia (Italy) 1980 earthquake: detailed analysis of a complex normal faulting, *J. Geophys. Res.*, **94**, 1631-1647.

Boatwright, J., Fletcher, J. B. and Fumal, T., 1991. A general inversion scheme for source, site and propagation characteristics using multiply recorded sets of moderate size earthquakes, *Bull. Seism. Soc. Am.* , **81**, 1754-1782.

Borcherdt, R. D., 1970. Effects of local geology on ground motion near San Francisco Bay, *Bull. Seism. Soc. Am.* , **60**, 29-61.

Boschi, E., Ferrari, G., Gasperini, P., Guidoboni, E., Smriglio, G. and Valensise, G., 1995. *Catalogo dei forti terremoti in Italia dal 461 a.C. al 1980*, ING-SGA, Roma, CD-ROM.

Bostock, M. G., 1992. Reflection and transmission of surface waves in laterally varying media, *Geophys. J. Int.*, **109**, 411-436.

Bouchon, M. and Aki, K, 1977. Discrete wavenumber representation of seismic-source wavefield, *Bull. Seism. Soc. Am.*, **67**, 2, 259-277.

Bouchon, M., and Coutant, O., 1994. Calculation of synthetic seismograms in a laterally varying medium by Boundary element-discrete wavenumber method, *Bull. Seism. Soc. Am.*, **84**, 6, 1869-1881.

Burridge, R. and Knopoff, L., 1964. Body force equivalents for seismic dislocations, *Bull. Seism. Soc. Am.* , **54**, 1875-1888.

Bus, Z., Szeidovitz, G. and Vaccari, F., 2000. Synthetic seismogram based deterministic seismic zoning for the Hungarian part of the Pannonian Basin, *PAGEOPH*, **157**, 205-220.

Camassi, R. and Stucchi, M., 1996. NT4.1: un catalogo parametrico di terremoti di area italiana al di sopra della soglia del danno. Internet, http://emidius.itim.mi.cnr.it/NT/home.html.

Caputo, M., Keilis-Borok, V., Oficerova, E., Ranzman, E., Rotwain, I. and Solovjeff, A., 1980. Pattern recognition of earthquake-prone areas in Italy. *Phys. Earth. Planet. Int.*, **21**, 305-320.

Cerveny, V., 1987. Ray tracing algorithms in three-dimensional laterally varying layered structures, in *Seismic Tomography* ed Nolet, G.,Reidel, Dordrecht, 99-133.

Chapman, C. H., 1978. A new method for computing synthetic seismograms, *Geophys. J. R. Astron. Soc.*, **54**, 481-513.

Chávez-García, F. J., Sánchez, L. R. and Hatzfeld, D., 1996. Topographic site effects and HVSR. A comparison between observations and theory, *Bull. Seism. Soc. Am.* , **86**, 1559-1573.

Corsanego, A., Faccioli, E., Gavarini, C., Scandone, P., Slejko, D. and Stucchi, M., 1997. *Gruppo Nazionale per la difesa dai terremoti. L'attività del triennio 1993-1995*, CNR, GNDT, Roma, 1997.

Costa, G., Panza, G.F., Suhadolc, P. and Vaccari, F., 1992. Zoning of the Italian region with synthetic seismograms computed with known structural and source information. *Proc. 10th WCEE*, July 1992, Madrid, Balkema, 435-438.

Costa, G., Panza, G.F., Suhadolc, P. and Vaccari, F., 1993. Zoning of the Italian territory in terms of expected peak ground acceleration derived from complete synthetic seismograms. *J. Appl. Geophys.*, **30**, 149-160.

Coutel, F. and Mora, P., 1998. Simulation based comparison of four site-response estimation techniques, *Bull. Seism. Soc. Am.*, **88**, 30-42.

Decanini, L., Gavarini, C., and Oliveto, G., 1993. Rivalutazione dei terremoti storici della Sicilia Sud-Orientale. In:*Atti del 6° Convegno Anidis* **3**, Perugia, Italy 13-15 October 1993: 1101-1110.

Decanini, L., Gavarini, C. and Mollaioli, F., 1995. "Proposta di definizione delle relazioni tra intensita' macrosismica e parametri del moto del suolo." *Atti del 7° Convegno L'ingegneria sismica in Italia*, Vol. **1**, 63-72.

Decanini, L. and Mollaioli, F., 1998. Formulation of Elastic Earthquake Input Energy Spectra, *Earthquake Engineering and Structural Dynamics*, **27**, 1503-1522.

Decanini, L., Mollaioli, F., Panza, G. F. and Romanelli, F., 1999. The realistic definition of the seismic input: an application to the Catania area, in Earthquake Resistant Engineering Structures II (G. Oliveto and C.A. Brebbia eds.), WIT press, Boston, 425-434.

Dravinski, M., G. Ding and Wen, K-L, 1996. Analysis of spectral ratios for estimating ground motion in deep basins, *Bull. Seism. Soc. of Am.*, **86**, 646-654.

Du, Z., Michelini, A. and Panza, G. F., 1998. EurID: a regionalized 3-D seismological model of Europe, *Phys. Earth. Planet. Inter.*, **105**, 31-62.

Du, Z. and Panza, G. F., 1999. Amplitude and phase differentiation of synthetic seismograms: a must for waveform inversion at a regional scale, *Geophys. J. Int.*, **136**, 83-98.

EC 8, 1993. Eurocode 8 structures in seismic regions - design - part 1 general and building, Doc TC250/SC8/N57A.

Fäh, D., Suhadolc, P. and Panza, G.F, 1993a. Variability of seismic ground motion in complex media: the Friuli area (Italy). In *Geophysical Exploration in Areas of Complex Geology, II* (eds Cassinis, R., Helbig, K. and Panza, G.F.), *J. Appl. Geophys.*, **30**, 131-148.

Fäh, D., Iodice, C., Suhadolc, P. and Panza, G.F, 1993b. A new method for the realistic estimation of seismic ground motion in megacities: the case of Rome. *Earthquake Spectra*, **9**, 643-668.

Fäh, D., and Panza, G.F, 1994. Realistic modelling of observed seismic motion in complex sedimentary basins, *Annali di Geofisica*, **37**, 6, 1771-1797.

Fäh, D., and Suhadolc, P., 1995. Application of numerical wave-propagation techniques to study local soil effects: the case of Benevento (Italy), *Pure and Appl. Geophys*, **143**, 513-536.

Fäh, D., Iodice, C., Suhadolc, P. and Panza, G.F., 1995. Application of numerical simulations for a tentative seismic microzonation of the city of Rome, *Ann. Geofis.* **38**, 607-616.

Farra, V. and Madariaga, R., 1987. Seismic waveform modeling in heterogeneous media by ray perturbation theory, *Journal of Geophys. Res*, **92** (3), 2697-2712.

Feroci, M., Funiciello, R., Marra, F. and Salvi, S., 1990. Evoluzione tettonica e paleogeografica plio-pleistocenica dell'area di Roma. *Il Quaternario*, **3**, 141-158.

Field, E. H., 1996. Spectral amplification in a sediment-filled valley exhibiting clear basin-edge-induced waves, *Bull. Seism. Soc. of Am.*, **86**, No. 4, 991-1005.

Field, E. H. and Jacob, K. H., 1995. A comparison and test of various site-response estimation techniques, including three that are not reference-site dependent, *Bull. Seism. Soc. of Am.*, Vol. **85**, No. 4, 1127-1143.

Florsch, N., Fäh, D., Suhadolc, P. and Panza, G. F., 1991. Complete synthetic seismograms for high-frequency multimode SH-waves, *PAGEOPH*, **136**, 529-560.

Fornberg, B., 1987. The pseudospectral method: Comparison with finite differences for the elastic wave equation, *Geophys.*, **52**, 483-501.

Funiciello, R., Lori, G. and Salvi, S., 1987. Ricostruzione delle superfici strutturali del sottosuolo della città di Roma. Atti del 6° Convegno del Gruppo Nazionale Geofisica della Terra Solida, CNR, Roma, 395-415.

Furumura, T. and Takenaka, H., 1996. 2.5-D modelling of elastic waves using the pseudospectral method, *Geophys. J. Int.*, **124**, 820-832.

Gasparini, C., Iannaccone, G. and Scarpa, R., 1985. Fault-plane solutions and seismicity of the Italian peninsula. *Tectonophysics*, **117**, 59-78.

Géli, L., Bard, P.-Y. and Jullien, B., 1988. The effect of topography on earthquake ground motion: a review and new results, *Bull. Seism. Soc. Am.*, **78**, 42-63.

GNDT, 1997. Progetto Catania - *Caratterizzazione geotecnica del territorio comunale di Catania a fini sismici*, GNDT, Milano.

Graves, R., 1998. Three-dimensional finite difference modeling of the San Andreas fault: source parametrization and ground motions level, *Bull. Seism. Soc. Am.*, **88**, 881-897.

Gregersen, S. and Alsop, L. E., 1974. Amplitudes of horizontally refracted Love waves. *Bull. Seism. Soc. Am.*, **64**, 535-553.

Gregersen S. and Vaccari, F., 1993. Lg-wave modelling for the North Sea, *Geophys. J. Int.*, **114**, 76-80.

Gusev, A. A., 1983, Descriptive statistical model of earthquake source radiation and its application to an estimation of short period strong motion, *Geophys. J. R. Astron. Soc.* **74**, 787-800.

Haskell N.A., 1962. Crustal reflection of plane SH waves, *J. Geophys. Res.*, **65**, 4751-4767.

Hays, W., Mohammadioun, B. and Mohammadioun, J., 1998. Seismic zonation: a framework for linking earthquake risk assessment and earthquake risk management. Ouest Éditions – Presse Académiques, Nantes, France.

Herrera, I., 1964. On a method to obtain a Green's function for a multi-layered half-space, *Bull. Seism. Soc. Am.*, **54**, 1087-1096.

Houston, H., and Kanamori, H., 1986, Source spectra of great earthquakes: teleseismic constraints on rupture process and strong motion, *Bull. Seism. Soc. Am.*, **76**, 19-42.

Joyner, W., 1984, A scaling law for the spectra of large earthquakes, *Bull. Seism. Soc. Am.*, **74**, 1167-1188.

Jeffreys, H. and Jeffreys, B. S., 1950. *Methods of mathematical physics*, Cambridege University Press, Cambridge.

Jennings, P.C., 1983. Engineering seismology. Terremoti: osservazione, teoria ed interpretazione. Rendiconti della Scuola Internazionale di Fisica 'Enrico Fermi', LXXXV Corso. Società Italiana di Fisica (ed.), 138-173.

Kanamori, H., 1977. The energy release in great earthquakes, *J. Geophys. Res.* **82**, 2981-2987.

Kausel, E. and Schwab, F., 1973. Contributions to Love wave transformation theory: earth flattening transformation for Love waves from a point source in a sphere, *Bull. Seism. Soc. Am.*, **63**, 983-993.

Kennett, B.L.N., 1984. Guided wave propagation in laterally varying media-I. Theoretical development., *Geophys. J. R. astr. Soc.*, **79**, 235-255.

Knopoff, L., Schwab, F. and Kausel, E., 1973. Interpretation of Lg, *Geophys. J. R. astr. Soc.*, **39**, 41-70.

Konno, K. and Ohmachi, T., 1998. Ground-motion characteristics estimated from spectral ratio between horizontal and vertical components of microtremor, *Bull. Seism. Soc. Am.*, **88**, N. 1, 228-241.

Kosloff, D., Reshef, M. and Loewenthal, D., 1984. Elastic wave calculations by the Fourier method, *Bull. Seism. Soc. Am.*, **74**, 875-891.

Lachet, C. and Bard, P.-Y., 1994. Numerical and theoretical investigations on the possibilities and limitations of Nakamura's technique, *J. Phys. Earth*, **42**, 377-397.

Langston, C. A., 1979. Structure under Mount Rainier, Washington, inferred from teleseismic body waves, *J. Geophys. Res.*, **84**, 4749-4762.

Lermo, J. and Chávez-Garcia, F. J., 1993. Site effect evaluation using spectral ratios with only one station, *Bull. Seism. Soc. Am.* , **83**, 574-1594.

Levander, A. R., 1988. Fourth-order finite difference P-SV seismograms, *Geophys.*, **53**, 1425-1436.

Levshin, A. L., 1973. Surface and Channel Seismic Waves. Moscow, *Nauka* (in Russian).

Levshin., A. L., 1985. Effects of lateral inhomogeneities on surface waves amplitudes measurements, *Ann. Geophys.*, **3**, 511-518.

Lungu, D., Cornea, T., Craifaleanu, I. and Aldea, A., 1996. Seismic zonation of Romania based on uniform hazard response. Proc. Fifth Int. Conference on Seismic Zonation, Oct. 17-19, 1995, Nice, France.

Lysmer, J. and Drake, L. A., 1972. A finite element method for seismology, in *Methods in computational Physics* (B. A. Bolt editor), Academic Press, New York, 181-215.

Madariaga, R., 1976. Dynamics of an expanding circular fault, *Bull. Seism. Soc. Am.*, **66**, 639-666.

Madariaga, R., 1989. Waveform synthesis by ray theoretical methods, in *Digital seismology and fine modeling of the lithosphere* (R. Cassinis, G. Nolet, G. F. Panza eds.), Ettore Majorana International Science Series, Physical Sciences, Plenum Press, New York, 49-78.

Maier, G., Diligenti, M. and Carini, A, 1991. A variational approach to boundary element elastodynamic analysis and extension to multidomain problems, *Computer methods in applied mechanics and engineering*, **92**, 192-213.

Malagnini, L. , Rovelli, A., Hough, S. E. and Seeber, L., 1993. Site amplification estimates in the Garigliano Valley, central Italy, based on dense array measurements of ambient noise, *Bull. Seism. Soc. Am.*, **83**, 1744-1754.

Manos, G.C. and Demosthenous, M., 1992. Design of R.C. structures according to the Greek Seismic Code Provisions. *Bull. of IISEE*, **26**, 559-578.

Markusic, S., Suhadolc, P., Herak, M. and Vaccari, F., 2000. A contribution to seismic hazard assessment in Croatia from deterministic modelling, *PAGEOPH.*, **157**, 185-204.

Marquering, H. and Snieder, R., 1995. Surface-wave mode coupling for efficient forward modelling and inversion of body-wave phases, *Geophys. J. Int.*, **120**, 186-208.

Marquering, H., 1996. *Surface-wave mode coupling: modelling and inverting waveforms including body-wave phases*, Geologica Ultraiectina, Utrecht.

Marrara, F. and Suhadolc, P., 1998. Observation and modeling of site effects in the Volvi basin, Greece. In: K. Irikura, K. Kudo, H. Okada and T. Sasatani, Eds., *The effects of surface geology on Seismic Motion*, Balkema, Rotterdam, The Netherlands, pp. 973-980.

Maruyama, T., 1963. On the force equivalents of dynamical elastic dislocations with reference to the earthquake mechanism, *Bull. Earthquake Res. Inst.*, Tokyo Univ., **41**, 467-486.

Maupin, V., 1988. Surface waves across 2-D structures: a method based on coupled local modes, *Geophys. J. Int.*, **93**, 173-185.

McGarr, A. and Alsop, L. E., 1967. Transmission and reflection of Rayleigh waves at vertical boundaries, *J. Geophys. Res.*, **72**, 2169-2180.

Moldoveanu, C.L. and Panza, G.F., 1999. Modelling for micronization purposes, of the seismic ground motion in Bucharest, due to the Vrancea earthquake of May 30, 1990. In: F. Wenzel et al. (Editors), Vrancea earthquakes: Tectonics, Hazard and Risk Mitigation, 85-97.

Molin, D., Ambrosini, S., Castenetto, S., Di Loreto, E., Liperi, L. and Paciello, A., 1986. Aspetti della sismicità storica di Roma. *Mem. Soc. Geol. It.*, **35**, 439-444.

Molin, D., Stucchi, M. and Valensise, G., 1996. *Massime intensità macrosismiche osservate nei comuni italiani*, elaborato per il Dipartimento della Protezione Civile. GNDT, ING, SSN, Roma.

Monti, G., Nuti, C. and Pinto, P. E., 1996. Non-linear response of bridges under multi-support excitation, *J. of Structural Engineering*, ASCE, **122**, 10.

Nafe, J. E., 1957. Reflection and transmission coefficients at a solid-solid interface of high-velocity contrast. *Bull. Seism. Soc. Am.*, **47**, 205-219.

Nakamura, Y., 1989. A method for dynamic characteristics estimation of subsurface using microtremor on the ground surface, *Q. Rept. Railway Tech. Res. Inst.*, **30**, 1, 25-33.

Nielsen, P., Flemming, I., Berg, P. and Skovgaard, O., 1995. Using the pseudospectral method on curved grids for 2D elastic forward modelling, *Geophysical Prospecting*, **43**, 369-395.

Nolet, G., 1990. Partitioned waveform inversion and two-dimensional structure under the network of autonomously recording seismographs, *J. Geophys. Res.*, **95**, 8499-8512.

Nolet, G., Trier, J. V. and Huisman, R., 1986. A formalism for nonlinear inversion of surface waves, *Geophys. Res. Lett..*, **13**, 26-29.

Nunziata, C., Fäh, D., and Panza, G. F., 1995. Mitigation of seismic hazard of a megacity: the case of Naples, *Annali di Geofisica*, **38**, 649-661.

Odom R.I., 1986. A couple mode examination of irregular waveguides including the continuum spectrum, *Geophys. J. R. astr. Soc.*, **86**, 425-453.

Olsen, K.B. and Archuleta, R., 1996. Three-dimensional simulation of earthquakes on the Los Angeles fault system, *Bull. Seism. Soc. Am.*, **85**, 575-596.

Orozova-Stanishkova, I.M., Costa, G., Vaccari, F. and Suhadolc, P., 1996. Estimates of 1 Hz maximum acceleration in Bulgaria for seismic risk reduction purposes, *Tectonophysics*, **258**, 263-274.

Panza, G.F., 1985. Synthetic seismograms: the Rayleigh waves modal summation, *J. Geophys.*, **58**, 125-145.

Panza, G.F., Schwab F.A., and Knopoff, L., 1973. Multimode surface waves for selected focal mechanisms. I. Dip-slip sources on a vertical fault plane, *Geophys. J. R. Astr. Soc.*, **34**, 265-278.

Panza, G.F. and Calcagnile, G., 1975. Lg, Li and Rg from Rayleigh modes, *Geophys. J. R. Astr. Soc.*, **40**, 475-487.

Panza, G.F., and Suhadolc, P., 1987. Complete strong motion synthetics. In *Seismic strong motion synthetics* (B. A. Bolt editor), Academic Press, Orlando, 153-204.

Panza, G.F., Prozorov, A. and Suhadolc, P., 1990. Is there a correlation between lithosphere structure and statistical properties of seismicity? In: R. Cassinis and G. F. Panza (Editors), The structure of the Alpine - Mediterranean area: contribution of geophysical methods. *Terra nova*, **2**, 585-595.

Panza, G.F., Vaccari, F., Costa, G., Suhadolc, P. and Fäh, D., 1996a. Seismic input modelling for zoning and microzoning, *Earthquake Spectra* **12**, 529-566.

Panza, G.F, Vaccari, F., and Cazzaro, R., 1997. Correlation between macroseismic intensities and seismic ground motion parameters, *Annali di Geofisica* **15**, 1371-1382.

Panza, G.F., Vaccari, F. and Cazzaro, R., 1999a. Deterministic seismic hazard assessment. In F. Wenzel et al. (Eds), Vrancea Earthquakes: Tectonics, Hazard and Risk Mitigation, 269-286. Kluwer Academic Publishers, The Netherlands.

Panza, G.F., Vaccari, F. and Romanelli, F., 1999b. The IUGS-UNESCO IGCP Project 414 : Realistic modeling of Seismic Input for Megacities and Large Urban Areas, *Episodes*, Vol. 22, 1, 26-32.

Pedersen, H., LeBrun, B., Hatzfeld, D., Campillo, M. and Bard, P.-Y., 1988. Ground motion amplitude across ridges, *Bull. Seism. Soc. Am.*, **84**, 1786-1800.

Philips, S. W. and Aki, K., 1986. Site amplification of coda waves from local earthquakes in Central California, *Bull. Seism. Soc. Am.*, **76**, 627-648.

Radulian, M., Vaccari, F., Mandrescu, N., Panza, G.F. and Moldoveanu, C.L., 2000. Seismic hazard of Romania: deterministic approach, *PAGEOPH*, **157**, 221-248.

Reiter, L., 1990. *Earthquake hazard analysis*, Columbia University Press, New York.

Riepl, J., Bard, P.-Y., Hatzfeld, D., Papaioannou, C., and Nechtshein, S., 1998, Detailed evaluation of site-response estimation methods across and along the sedimentary valley of Volvi (EURO-SEISTEST), *Bull. Seism. Soc. Am.*, **88**, 488-502.

Romanelli, F. Bing, Z., Vaccari, F. and Panza, G.F., 1996. Analytical computation of reflection and transmission coupling coefficients for Love waves, *Geophys. J. Int.*, **125**, 132-138.

Romanelli F., Bekkevold J. and Panza, G.F., 1997. Analytical computation of coupling coefficients in non-poissonian media, *Geophys. J. Int.*, **129**, 205-208.

Romanelli, F., Vaccari, F. and Panza, G. F., 1998a, Realistic Modelling of ground motion: techniques for site response estimation. In: *Proceedings of 6th U.S. National Conference on Earthquake Engineering*, Seattle, U.S.A. 31 May - 4 June 1998, CD-ROM: paper 433.

Romanelli, F., Nunziata, C., Natale, M. and Panza, G. F., 1998b. Site response estimation in the Catania area. In: K. Irikura, K. Kudo, H. Okada and T. Sasatani, Eds., *The effects of surface geology on Seismic Motion*, Balkema, Rotterdam, The Netherlands, pp. 1093-1100.

Romanelli, F. and Vaccari, F., 1999. Site response estimation and ground motion spectral scenario in the Catania Area, *J. of Seism.*, **3**, 311-326.

Saraò, A., Das, S. and Suhadolc, P., 1998. A comprehensive study of the effect of non-uniform station distribution on the inversion for earthquake rupture history for a Haskell-type source model, *J. of Seism.*, **2**, 1-25.

Schwab, F. A., and Knopoff, L., 1972. Fast surface wave and free mode computations, in *Methods in Computational Physics* (B. A. Bolt editor), Academic Press, New York, 86-180.

Schwab, F. A., Nakanishi K., Cuscito M., Panza G. F. and Liang, G., 1984. Surface-wave computations and the synthesis of theoretical seismograms at high frequencies, *Bull. Seism. Soc. Am.*, **74**, 1555-1578.

Snieder, R., 1986. 3D Linearized scattering of surface waves and a formalism for surface wave holography, *Geophys. J. R. astr. Soc.*, **84**, 581-605.

Somerville, P., 1996. Ground Motions, in *Scenario for a magnitude 7.0 earthquake on the Hayward fault*, EERI, Oakland, pp. 35-42.

Stümpel, H., Khaler, S., Meissner, R. and Milkereit, B. 1984. The use of shear waves and compressional waves for lithological problems of shallow sediments. *Geophys. Prosp.*, **32**, 622-675.

Suhadolc, P., 1990. Fault-plane solutions and seismicity around the EGT southern segment. In: R. Freeman and St. Müller (Editors), Sixth EGT Workshop: Data Compilations and Synoptic Interpretation, European Science Foundation, Strasbourg, pp. 371-382.

Suhadolc, P., Panza, G.F., Marson, I., Costa, G. and Vaccari, F., 1992. Analisi della sismicità e meccanismi focali nell'area italiana. Atti del Convegno del Gruppo Nazionale per la Difesa dai Terremoti, Pisa 1990, **1**, 157-168.

Takeuchi, H. and Saito, M., 1972. Seismic surface waves, in *Methods in Computational Physics*, Volume 11, B.A. Bolt, Editor, Academic Press, New York, 217-295.

Theodulidis, N., Bard, P. Y., Archuleta, R. and Bouchon, M., 1996. Horizontal-to-vertical spectral ratio and geological conditions: the case of Garner Valley downhole array in Southern California, *Bull. Seism. Soc. of Am.*, **86**, No. 2, 306-319.

Uang, C. M. and Bertero, V. V., 1990. Evaluation of seismic energy in structures. *Earthquake Engineering and Structural Dynamics*, **19**, 77-90.

Vaccari, F., 1995, LP-displacement hazard evaluation in Italy. In: Proc. 24th General Assembly of the European Seismological Commission, Athens, 3: 1489-1498.

Vaccari, F., Gregersen S., Furlan M. and Panza G. F., 1989. Synthetic seismograms in laterally heterogeneous, anelastic media by modal summation of P-SV waves, *Geophys. J. Int.*, **99**, 285-295.

Vaccari, F., Suhadolc, P. and Panza, G.F., 1990. Irpinia, Italy, 1980 earthquake: waveform modelling of strong motion data, *Geophys. J. Int.* **101**, 631-647.

Vaccari, F. and Panza, G.F., 1993. V_P/V_S estimation in southwestern Europe from P-wave and surface-wave tomography analysis. *Physics of the Earth and Planetary Interiors*, **78**, 229-237.

Vaccari, F. and Gregersen S., 1998. Physical description of Lg waves in inhomogeneous continental crust, *Geophys. J. Int.*, **135**, 711-720.

Ventriglia, U., 1971. La geologia della città di Roma. Amm. Prov. di Roma, Roma.

Wolf, J. P. and Song, C., 1996. *Finite-element modelling of unbounded media*, Wyley and Sons.

Woodhouse, J. H., 1974. Surface waves in a laterally varying layered structure, *Geophys. J. R. astr. Soc.*, **89**, 5953-5986.

Yamanaka, H., Drawinski M. and Kagami, H., 1993. Continuous measurements of microtremors on sediments and basements in Los Angeles, California, *Bull. Seism. Soc. Am.*, **83**, 1595-1569.

Zivcic, M., Suhadolc, P. and Vaccari, F., 2000. Seismic zoning of Slovenia based on deterministic hazard computations, *PAGEOPH*, **157**, 171-184